

ABSTRACT

Dissertation Title: **ELECTROCHEMICAL ANALYSIS ON
THE CHARGE TRANSPORT
PROPERTIES OF HETEROGENEOUS
SUPERCAPACITOR ELECTRODE
MATERIALS**

Zhe Gui, Doctor of Philosophy, 2014

Dissertation Directed By: **Professor Sang Bok Lee, Department of
Chemistry and Biochemistry**

The design and exploration of heterogeneous materials for energy storage system are investigated here. The charge transport property of the electrode materials is tuned through different architectures and chemical compositions. This dissertation describes the motivation, design, and fabrication of heterogeneous materials grown on cellulose fibers or as free standing ordered nanoarrays with AAO technology. Their advanced electrochemical properties were enabled by the more feasible charge transfer processes enhanced by structural or compositional regulations. In the first approach, cellulose fibers with porous structure and electrolyte absorption properties are explored as prospective substrate for the deposition of energy material. These substrates are lighter, more flexible and better performing than the traditional substrates (e.g. gold, stainless steel), and are able to also function as an interior

electrolyte reservoir. We demonstrated the value of this internal electrolyte reservoir by comparing a series of hierarchical hybrid supercapacitor electrodes based on home-made cellulose paper or polyester textile integrated with carbon nanotubes (CNTs) by simple solution dip, and electrodeposited with MnO_2 . Besides substrate, direct modification on the active materials itself was also conducted to advance the charge transfer process. In this approach, heterogeneous materials were synthesized either through single step or two step fabrications processes assisted with AAO technology, revealing well-ordered 1D nanoarrays. Solely MnO_2 nanowires were compared with a series of RuO_2 - MnO_2 composite nanowires with different loading amounts manipulated through the co-electrochemical deposition. The RuO_2 has direct beneficial influences on the charge transfer process as evidenced by the impedance behavior, and shows capability to enhance both the power and energy densities of MnO_2 materials. Additionally, a general route to grow metal oxides into/onto polymer nanowires matrixes through the redox-exchange reaction between high oxidation state metal ions and different polymers were explored here. These heterogeneous materials embed the metal oxide materials (MnO_2 , RuO_2) into/onto polymer arrays (PEDOT, PPY) where good electrical conductivity and ion diffusion path are well maintained, realizing the maximum utilization of synergistic materials. These heterogeneous supercapacitor electrode materials engineered in aspects of substrate, structure, and compositions show promising capability in directing the future energy material toward high performance and easy packing to meet the requirements dictated by different fields.

ELECTROCHEMICAL ANALYSIS ON THE CHARGE TRANSPORT
PROPERTIES OF HETEROGENEOUS SUPERCAPACITOR ELECTRODE
MATERIALS

By

Zhe Gui

Dissertation submitted to the Faculty of the Graduate School of the
University of Maryland, College Park, in partial fulfillment
of the requirements for the degree of
Doctor of Philosophy
2013

Advisory Committee:
Professor Sang Bok Lee, Chair
Professor Neil Blough
Professor Bryan Eichhorn
Professor Gary W. Rubloff
Professor YuHuang Wang

© Copyright by

Zhe Gui

2013

Dedication

I would like to dedicate this dissertation to my parents and sister for their endless support.

Acknowledgements

Most of all, I would like to thank my advisor, Professor Sang Bok Lee, for his guidance and support throughout my graduate career. Many thanks go to his courage during my candidacy, his innovative ideas on research and his directing in thinking and solving problems scientifically.

I would like to thank Stefanie Sherrill for great organization on the group meetings and conference events, and being always nice. I thank Liz Nguyen for bring group members together, and make it feel home. I thank Dr. Kim for showing my how to grow the nice metal nanotube. I would like to thank Jonathon Duay for the stimulating and productive discussion on research and the nice introduction of American culture with patience. I thank Junkai Hu for the interesting comments on research and useful information for living. I thank Eleanor Gillette for giving valuable writing advice and sharing interesting stories at happy hour. I thank Jaehee Song for sharing interesting papers and seminars. I thank Lauren Graham for keeping us updated what is going on downstairs. I thank Nikki Schneck for introducing the bio-side science research with passion. I would like to acknowledge the hard work of Dr. Ran Liu, which contributes to the solid foundation of Lee group's research. I would like to thank Dr. Liangbing Hu for initiating the project corporation opportunity and thank Dr. Hongli Zhu from his group for her expertise in paper science and corporation work. I would like to thank Professor Rubloff and his group for their engineering perspective as well as technical supports. I would like to thank the Maryland Nanocenter staff (especially Li Chung Lai) for their training and assistance.

I would like to thank Professor Neil Blough, Professor Bryan Eichhorn, Professor Gary W. Rubloff and Professor YuHuang Wang for kindly accepting to serve on my committee and for their suggestions and support along the way.

I would like to thank my family and friends for their continued support for my study and life.

Table of Contents

Dedication	ii
Acknowledgements	iii
Table of Contents	v
List of Schemes	vii
List of Tables	viii
List of Figures	ix
List of Abbreviations	xi
Chapter 1: Introduction to Supercapacitor Technology	1
1.1 Background and Current Challenge	1
1.2 Supercapacitors Category and Materials	3
1.2.1 Electrical Double-Layer Capacitors	7
1.2.2 Pseudocapacitors	9
1.3 Factors and Strategies for Supercapacitors	14
1.3.1 Factors Affecting the Ragone Plots	14
1.3.2 Nanostructure for Ion Diffusion	17
1.3.3 Heterogeneous Materials with Synergistic Properties	23
1.4 Approach Overview	24
Chapter 2: Fabrication and Characterization of 1D Nanostructured Supercapacitor materials	26
2.1 1D Well-ordered Nanoarrays Materials Synthesis	26
2.1.1 AAO Template	26
2.1.2 Electrochemical Deposition	31
2.2 Characterization of Nanostructure Materials	33
2.2.1 Structural Characterization	34
2.2.1.1 SEM and TEM	34
2.2.2 Chemical Compositions Characterization	36
2.2.2.1 EDS	36
2.2.2.2 XPS	38
2.2.2.3 Raman	39
2.2.2.4 ICP-AES	41
2.2.3 Electrochemical Characterization	42
2.2.3.1 GV and CV	43
2.2.3.2 Electrochemical Impedance Spectroscopy	46
Chapter 3: Natural Cellulose Fibers as Substrate for Supercapacitors	48
3.1 Introduction	48
3.2 Experimental Section	51
3.2.1 Electrode Fabrication	51
3.2.3 Characterizations	52
3.3 Results and Discussion	54
3.3.1 Structural Characterization	54
3.3.2 Electrochemical Characterizations	63

3.3.3 Electrochemical Impedance Spectroscopy	68
3.3.4 Cycling Performance	70
3.4 Conclusion	72
Chapter 4: RuO ₂ -MnO ₂ Composite Material for Supercapacitors with High Energy and Power Densities.....	74
4.1 Introduction.....	74
4.2 Experimental Section.....	76
4.2.1 Nanowires Synthesis.....	76
4.2.2 Characterizations.....	77
4.3 Results and Discussion	79
4.3.1 Structural Characterization	79
4.3.2 Electrochemical Characterizations.....	85
4.3.3 Effect of RuO ₂ Loading Amount	88
4.3.4 Deconvolutions of the Capacitance	90
4.4 Conclusion	94
Chapter 5: Redox-Exchange Induced Heterogeneous RuO ₂ -Conductive Polymer Nanowires	95
5.1 Introduction.....	95
5.2 Experimental Section.....	98
5.2.1 Chemicals and Materials.....	98
5.2.2 Synthesis	98
5.2.3 Characterizations.....	100
5.3 Results and Discussion	101
5.3.1 Growth Scheme and Structural Characterizations	101
5.3.2 Charge Storage Mechanism and Electrochemical Characterizations	113
5.4 Conclusion	119
Chapter 6: Summary and Outlook	121
6.1 Summary	121
6.2 Outlook	123
Publication	125
Reference	127
Appendices.....	126

List of Schemes

Scheme 3.1 Schematic illustration of the synthesis process.....	56
Scheme 4.1 Schematic illustration of the electrochemical co-deposition process.....	80
Scheme 5.1 Synthesis of heterogeneous RuO ₂ -Polymer nanowires.....	100

List of Tables

Table 1.1 Electrochemical capacitor vs. battery.....	5
Table 3.1 Summary of the samples with different configurations.....	55
Table A.1 Literature survey of MnO ₂ -based supercapacitors electrode	149

List of Figures

Figure 1.1 Ragone Plot	3
Figure 1.2 Representation of energy storage devices	4
Figure 1.3 Electrical double layer capacitor graphic	8
Figure 1.4 Specific capacitance values of different materials.	11
Figure 1.5 Pseudocapacitor charge storage mechanism	12
Figure 1.6 Charge storage mechanism for conductive polymers.....	13
Figure 1.7 Contributions of polarizations on power and energy.	16
Figure 1.8 Comparing bulk and nanostructured materials for energy storage.....	18
Figure 1.9 Stress buffering ability of bulk and nanostructured materials.....	20
Figure 1.10 Illustration of different nanostructure defined by dimensionalities.	22
Figure 2.1 Schematic illustration of the two-step anodizing process for AAO.	28
Figure 2.2 SEM images of homemade AAO	29
Figure 2.3 Graphic and SEM images of novel porous alumina structures	30
Figure 2.4 AAO assisted electrodeposition set-up.....	33
Figure 2.5 SEM and TEM image for 1D nanoarrays.....	36
Figure 2.6 EDS line scan across a single nanowire or nanotube	37
Figure 2.7 Deconvoluted XPS spectra.....	39
Figure 2.8 Raman spectra of electrodeposited MnO ₂ with birnessite phase.....	40
Figure 2.9 Calibration curve for Ru element	42
Figure 2.10 Typical GV and CV curves	44
Figure 2.11 Illustration of the energy stored in supercapacitor and battery	45
Figure 2.12 Simple equivalent circuits and their Nyquist plots.....	47
Figure 3.1 SEM characterizations on the different fibers.	59
Figure 3.2 SEM and TEM images on different CNT-paper based electrodes.	61
Figure 3.3 Raman spectra of MnO ₂ electrodeposited on cellulose paper	62
Figure 3.4 SEM images of P-CMC at higher magnifications.....	62
Figure 3.5 HRTEM on the MnO ₂ nanosheets structure.....	63
Figure 3.6 Schematic illustration of the fabrication process.....	65
Figure 3.7 SEM-EDS characterization on ALD alumina coated fiber	66
Figure 3.8 Electrochemical performance of MnO ₂ on different substrates.	66
Figure 3.9 Electrochemical performance.....	68
Figure 3.10 Impedance spectra and cycling test	70
Figure 4.1 SEM, TEM, and EDS images of RuO ₂ -MnO ₂ composite material.....	81
Figure 4.2 d-space measurements on TEM image and FFT resolved image.....	82
Figure 4.3 Raman and XPS characterization	84
Figure 4.4 XPS spectra for Ru 3p in the RuO ₂ -MnO ₂ composite material.....	84
Figure 4.5 Electrochemical performance for bare MnO ₂ and RuO ₂ -MnO ₂ composite	87
Figure 4.6 Capacitance and impedance behavior of RuO ₂ - MnO ₂ composite nanowires	89
Figure 4.7 Deconvoluted capacitances for MnO ₂ with different RuO ₂ loading amount	93
Figure 4.8 Voltammetric responses at 20 mV/s for the pristine MnO ₂ nanowires	93

Figure 5.1 Potentiostatic transients for the Polymer electrodeposition	103
Figure 5.2 Barrett-Joyner-Halenda pore-size distribution curves from N ₂ adsorption branches of PEDOT and PPY films.....	104
Figure 5.3 SEM and TEM images for different polymer nanowires	105
Figure 5.4 EDS element mapping and line scan results.....	106
Figure 5.5 TEM images and EDS line scan result on MnO ₂ -PPY nanowires	108
Figure 5.6 XPS and FTIR on the hybrid RuO ₂ -polymer nanowires	109
Figure 5.7 XPS Ru 3p spectra of composite PEDOT-RuO ₂	110
Figure 5.8 XPS spectra of N 1s of PPY-RuO ₂	112
Figure 5.9 Effect of soaking time on the RuO ₂ mass loading.....	113
Figure 5.10 Electrochemical characterizations of the RuO ₂ -polymer nanowires.....	114
Figure 5.11 Specific capacitance of RuO ₂ -polymer nanowires.	116
Figure 5.12 Cycling ability of the two polymer-RuO ₂ nanowires	118

List of Abbreviations

AAO- Anodic aluminum oxide

ECD- Electrodeposition

EDLC- Double-layer electrostatic charging

PEDOT- Poly (3,4-ethylenedioxythiophene)

EDOT- 3,4-ethylenedioxythiophene

PPY- Polypyrrole

CV- Cyclic voltammetry

GV- Galvanostatic voltammetry

CNTs- Carbon nanotubes

Chapter 1: Introduction to Supercapacitor Technology

1.1 Background and Current Challenge

Due to the fast consumption of fuel sources and growing global green-house effect, more sustainable, renewable and environmental-friendly energy sources such as wind and solar power are taking increasingly important role in the energy development. In order to efficiently use the renewable energy, we need controllable and reliable devices to store and deliver the power on demand. An electrochemical energy storage system with easy-portability, high conversion efficiency, and zero gaseous exhaust is an important field that bridges the gap between the sustainable power source and energy market.¹ Among these devices, batteries are well-commercialized and dominate the landscape in electrochemical energy storage in terms of all different aspects of our life, such as portable electronics (e.g. cellphone, laptop, PDAs) and transportation. However, substantial efforts are still needed to advance the battery to meet the requirements dictated by different fields, such as packing efficiency for the fast developing computer science applications and high energy/power density for heavy-duty electrical vehicles.^{2,3} Compared to batteries with their high energy density, supercapacitors stand out for their high power performance, which can meet the requirement when fast energy storage and release is needed, for example, in traction and space flight technologies.^{4,1,5} Due to the intrinsic properties of the energy materials and different charge storage mechanisms, batteries, capacitors, and supercapacitors locate in different regions in the Ragone plot as show in Figure 1.1.⁶ High energy density is desired for long working time, and can be

approached by batteries devices. However in term of power performance, batteries show relatively mild output. Conventional capacitor show good power density yet fairly low energy storage. In order to achieve short charging time and peak power release needed in some advanced applications, while maintaining good energy density, there is growing attention on supercapacitor research and development. The supercapacitor's capability, as illustrated in Figure 1.1, bridges the gap between capacitor and battery, showing moderate energy density and good power density.

Supercapacitor has realized its practical value in some portion of the energy storage market and has growing demand in not only traditional fields of electronics, but also in power generation and transportations sectors. Although wide spread usage of supercapacitors is still limited by the high cost, and some technical problems, growing interest and effort are continuing to be devoted to the research of this field, and genuine progress has been made.⁷⁻⁹

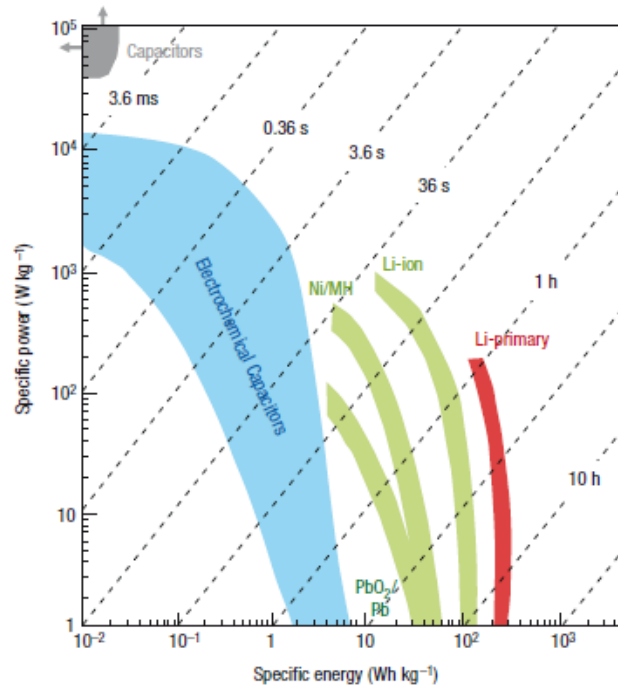


Figure 1.1 Ragone Plot

Ragone plot of power density (W/kg) *versus* energy density (Wh/kg) with various electrical energy storage technologies including capacitors, electrochemical capacitors, and batteries. (Graph reprinted from Simon *et al.* ⁶)

1.2 Supercapacitors Category and Materials

A conventional capacitor consists of two metal plates and dielectric media in between. Energy is stored electrostatically when a potential difference is applied between the two conductors. As the potential increases, the charge stored on the plates increases linearly. The capability of how much charge can be stored per voltage applied is known as capacitance, which is related to the dielectric constants ($\epsilon = \epsilon_r \epsilon_0$, ϵ_r is the relative permittivity of dielectric media, and ϵ_0 is the vacuum permittivity

constant with value of 8.854×10^{-12} F/g), plate area size (A) and distance between the two plates (d). In a simple parallel model, the capacitance can be expressed by the following equation.⁵

$$C = \frac{\epsilon_r \epsilon_0 A}{d} \quad 1$$

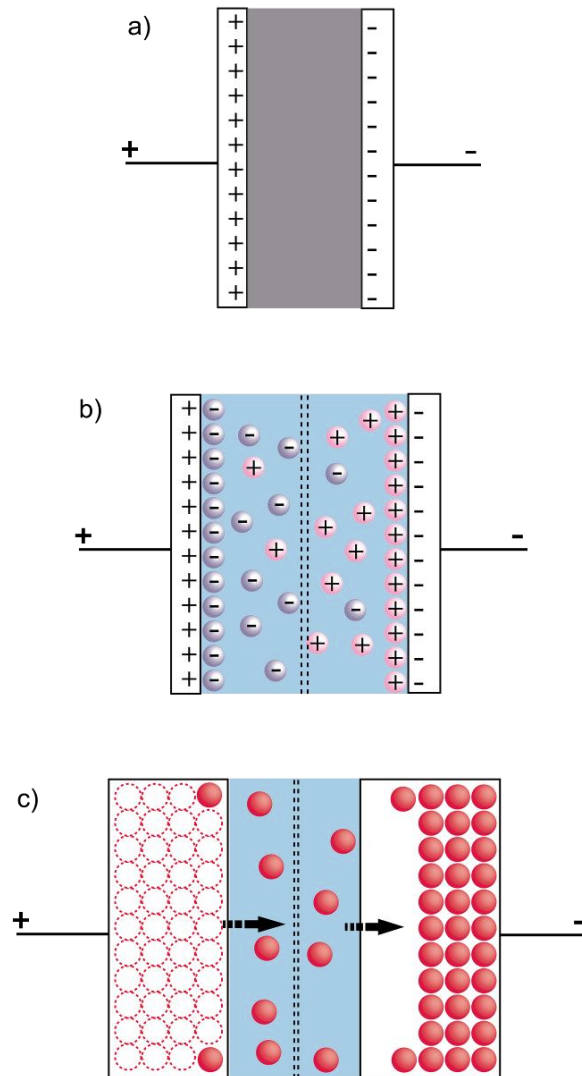


Figure 1.2 Representation of energy storage devices

(a) Conventional capacitors, (b) electrochemical capacitor, (c) lithium battery

For a traditional capacitor, the capacitance is very low, on the order of 10^{-3} Farad. We can achieve much higher capacitance, up to 10^6 Farad, in an electrochemical capacitor (EC). In electrochemical capacitors, electrolyte is used instead of dielectric layers. Therefore charge is stored at the interface between the electrode and electrolyte, resulting in two capacitors in series. The separation distance between the opposite charged layers in electrochemical capacitors is very small, typically around few Angstrom for aqueous electrolyte, compared to a few millimeters for conventional capacitor.¹⁰ With higher capacitance, higher energy density can be obtained according to the following equation, moving toward the top right region in the Ragone plot:

$$E = \frac{CV^2}{2} \quad 2$$

The charge/discharge process in battery occurs at more or less constant potential and is usually accompanied by a phase change process, while in an electrochemical capacitor, the potential is a continuous function of degree of charge that is passed into the electrode.¹¹ As shown in Figure 1.2, the bulk battery electrode materials will be accessible during the insertion/desertion processes, rather than the surface-only redox process in pseudocapacitor or the electrode/electrolyte interface ion/electron charge separation process in electrochemical double layer supercapacitor, which will be discussed in the following sections. The differences between electrochemical capacitors and battery are listed in table 1.1.

TABLE 1.1 Electrochemical capacitor vs. battery

	<i>Supercapacitor</i>	<i>Battery</i>
Potential	Continuous value with degree of charge build-up	Constant value during charge/discharge
Energy	<10 Wh/kg	×100 Wh/kg
Power	×10 ⁴ W/kg	<10 ³ W/kg
Cycle ability	Long cycle life with high degree of reversibility (up to 10 ⁶ for RuO ₂ ¹²)	Hundred cycles due to material irreversibility and kinetic irreversibility
Charge mechanism	Double-layer electrostatic charging (EDLC) & surface fast faradaic charging (pseudocapacitor)	Faradaic redox reaction with changing of the oxidation states accompanying by ion insertion/desertion

We want to note here that the battery does enable more efficient utilization of the electrode material than electrochemical capacitors. At the same time, better reversibility and stability are achieved by the EC. Design of hybrid energy storage devices integrating EC with battery is desired for both high energy and power performances. For example, a hybrid battery-ultracapacitors energy storage system has been used in hybrid electrical vehicles (HEVs).¹³⁻¹⁵ In HEVs, supercapacitors play the key role to capture the regenerative braking energy and quickly deliver burst power for acceleration and hill climbing, therefore increasing fuel efficiency.

Supercapacitors can be divided into two main categories, electrical double-layer capacitors (EDLC) and pseudocapacitors, based on the charge storage mechanisms. For electrical double layer capacitors, “super” charge storage is realized through the

high surface area of electrode material (A) and small charge separation distance (d). While for pseudocapacitors, “super” is achieved through the surface redox reactions of the active material, which is a faradaic process. For comparison, Conway has quantified the degree of electron transfer in different devices as: 0.18 e⁻/atom of accessible surface in a double-layer capacitor, 1–2.5 e⁻ /atom of accessible surface of electro-active material in a pseudocapacitor and 1–2 e⁻ /atom or molecule of bulk phase for a battery.⁵

1.2.1 Electrical Double-Layer Capacitors

Electrochemical capacitors were first reported in 1957 by Becker using porous carbon electrodes.¹⁶ In 1987, the first commercialized double layer capacitor was produced by NEC with name “Supercapacitor”, under license from SOHIO.⁵ In these electrical double layer capacitors, the capacitance is much larger than the electrostatic capacitance, and can be attributed to the ultra-small separation distance and high surface area. For example, for a conventional capacitor with $A=1\text{m}^2$, (much larger than real device) and $d=1\ \mu\text{m}$, $\epsilon_r=1000$, capacitance equals 8.9 mF based on equation 1; in carbon double layer capacitors with separation of 0.7 nm (Debye length of water), $\epsilon_r=80$ for aqueous electrolyte, and surface area of $10^3\ \text{m}^2/\text{g}$, $C= 1012\ \text{F}$ for 1 g commercial available active carbon.

A model to understand the double layer was first built by Helmholtz in 1853.¹⁷ In this early EDL model, the double layer was described as two opposite charge layers at the interface of electrode and electrolyte. Later on this model was modified by Gouy and Chapman to take account of a continuous ion distribution in the electrolyte

solution from the electrode surface, termed as a diffusion layer.^{18,19} Stern model was built based on these two theories, and states that there are two ion distribution regions. One is the compact layer (stern layer) near the electrode surface and another is the diffusion layer extends from the compact layer. Concepts of inner Helmholtz plane (IHP) and outer Helmholtz plane (OHP) were used to define the region of two differently absorbed ions. As shown in equation 1 for a planar electric capacitor, d represents the effective EDL thickness, also called Debye length. Another effect that contributes to the high capacitance performance is the large surface area of electrode materials. As shown in Figure 1.3, we can see the double layer is formed at the high surface area of the electrode materials. With higher effective area for charge separation to take place, more energy can be stored.

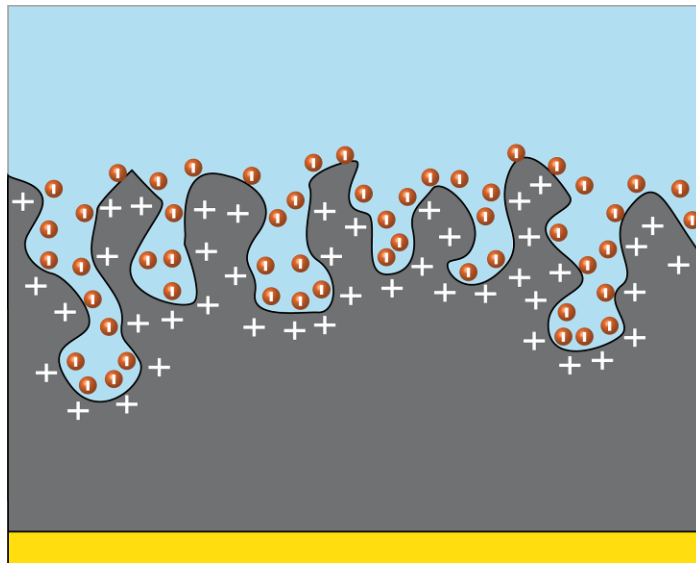


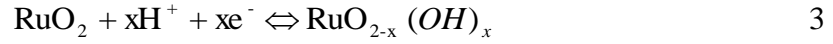
Figure 1.3 Electrical double layer capacitor graphic

All kinds of carbon based materials have been explored for application in EDLC.²⁰⁻²⁹ Carbon materials have many good qualities, such as good conductivity, high surface area, light weight, and moderate cost. For commercially available active carbon, surface areas of up to 3000 m²/g can be achieved.²⁵ Other alternative materials, such as graphene, carbon nanotubes, carbon fibers, and carbon based composite materials have also been reported. The pore size and shape of the carbon materials also play an important role in determining the EDLC performance.²⁵ So far, active carbon can achieve 100-300 F/g capacitance in aqueous electrolyte, and a high capacitance of 524 F/g was reported for CNT-aerogel composite material with a high surface area of 1059 m²/g.^{24,30} Since the energy is stored through nonfaradaic charge-separation process in EDLCs, the cyclability is very good with capacitance well retained after over 100k cycles.

1.2.2 Pseudocapacitors

In 1971, Trasatti and Buzanca reported the capacitive performance of RuO₂ observed during its charge/discharge in acidic electrolyte.³¹ Following that, fundamental research and commercialization development have been devoted to RuO₂ materials as supercapacitors.³²⁻⁴¹ The charge storage mechanism for RuO₂ is based on reversible redox reactions between multiple charge states of ruthenium. This is a faradaic process and is different from the EDLC electrostatic charge separation mechanism. A new term “Pseudo” was used to specify this type of electrochemical capacitors. In the study of RuO₂, the extent of charge accumulated shows a linear change with voltage profile during the charge storage process, which means the

derivative dQ/dV is constant, known as a capacitor characteristic. The redox reaction for RuO_2 can be expressed by the following equation:



Ruthenium has several charge states of +2, +3, +4, and successive redox processes will occur during the cyclic voltammetry (CV) characterization, possibly overlapping at the operating potential window, and showing rectangular, mirror-image CV curve.

After that, more materials have been reported as pseudocapacitor materials, which mainly contains two subcategories, one is transition metal oxides, and another one is conductive polymers.^{5,8,42,43} The capacitance values of different active materials reported in the literature were summarized and reported by K. Naoi *et al.* as shown in Figure 1.4.⁸ For transition metal oxides, the pseudocapacitance is gained through fast potential-dependent reactions that occur at the surface (absorption/desorption) or near surface (intercalation/deintercalation) of the active material. For conductive polymers the charge is stored through the counter ions absorption/ desorption process as the polymer is oxidized or reduced.

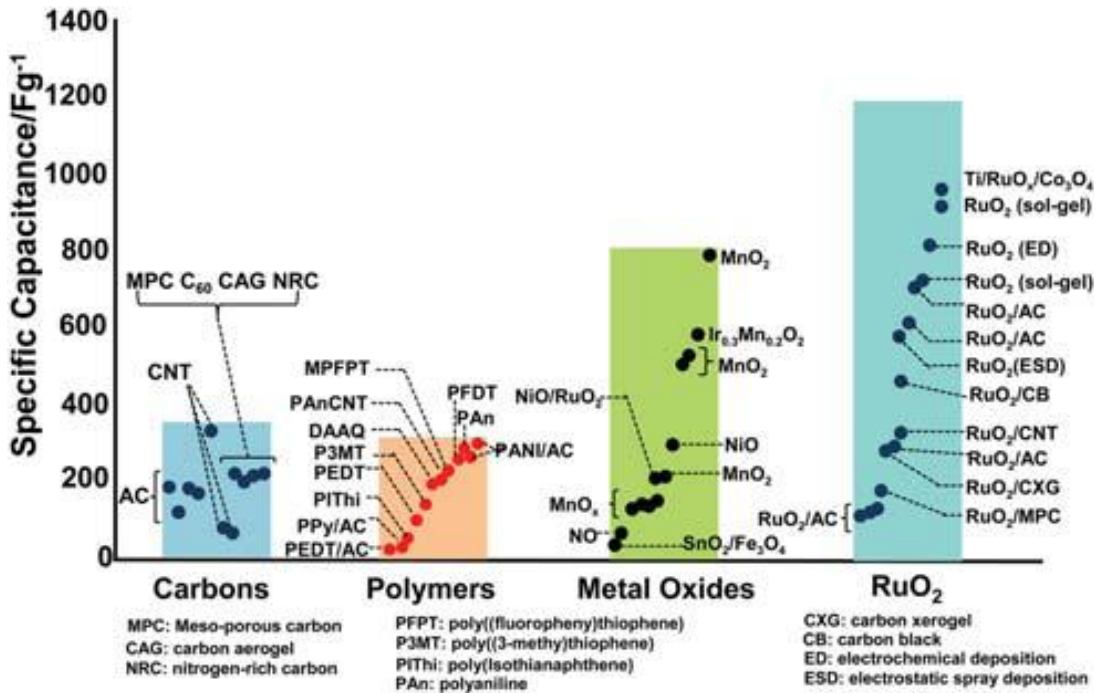


Figure 1.4 Specific capacitance values of different materials.

Based on literatures reported values (reprinted from reference ⁸).

Transition metal oxides including RuO_2 ,^{41,40,44,35,32} MnO_2 ,⁴⁵⁻⁵⁰ NiO/Ni(OH)_2 ,⁵¹⁻⁵⁴ V_2O_5 ^{55,56} have all been reported to show capacitive energy storage capability. The charge storage mechanism includes two main processes: surface absorption/desorption of ions, and fast faradaic reactions at near surface, as shown in Figure 1.5. Among all these metal oxides, MnO_2 has been most investigated due to its low cost, environmental benignity, and good energy density. MnO_2 has been used in alkaline battery industry for more than 150 years, and its potential in supercapacitors fields was reported in 1999 by Lee and Goodenough, using neutral aqueous electrolyte.⁴² This discovery has raised great interest for the exploring of MnO_2 materials for supercapacitor electrode at both basic and applied levels.⁵⁷ The

theoretical capacitance of MnO_2 is calculated to be 1100 F/g based on one electron redox process in aqueous electrolyte, which is much larger than EDLCs.⁴³

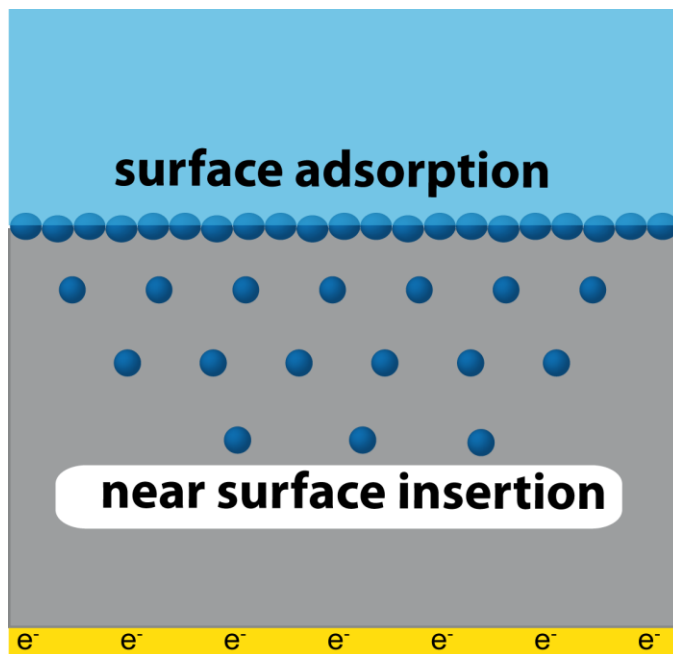


Figure 1.5 Pseudocapacitor charge storage mechanism

Both surface adsorption and near surface insertion take place. Cations are represented by the blue particles and electrons are transferring from the bottom towards the surface.

Since the discovery of conductive polymers in 1980s, their applications in the supercapacitor field have drawn much attention. Good electronic conductivity of magnitudes of $1\text{-}100 \text{ S cm}^{-1}$ can be achieved by the polymers through the π -conjugated electrons and pseudocapacitance can be stored through the redox reversible reaction between different doped states.⁵⁸⁻⁶¹ The potential for using conductive polymers for energy storage was first proposed and discussed by

Gottesfeld and Conway.^{58,5} Polyacetylenes,^{62–65} polyaniline,^{66,67} polypyrrole,^{68–73} and polythiophene^{74–78} are some of the earliest studied polymers in this field. The charge/discharge process of a p-type conductive polymer is shown in Figure 1.6. Polymer doping state is continually changing between undoped and p/n-doped types (p-type: positively charged; n-type: negatively charged) with charge balanced by the counter ions from the electrolyte. Compared to metal oxides, the charge storage mechanism of polymer is more like the double layer process than battery type behavior. Successive oxidization/reduction down the polymer chains gives rise to the capacitive features, showing an almost mirror-like rectangular CV curve. Since the charge is stored in the highly reversible doping/undoping process with electron withdrawal or electron donation, no significant structure changes are observed within certain potential window and electrolyte, and so good cyclability up to 100k cycles has been achieved.

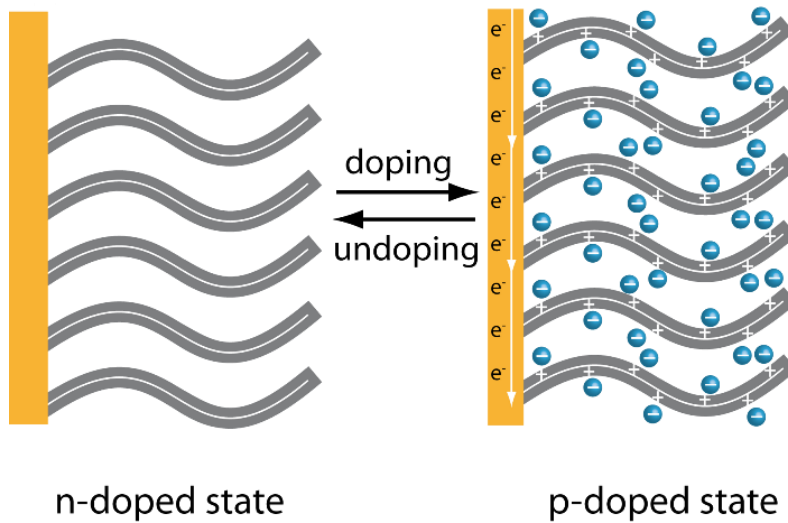


Figure 1.6 Charge storage mechanism for conductive polymers

1.3 Factors and Strategies for Supercapacitors

As we look at the charge storage mechanism of pseudocapacitors, it is not hard to realize that both the electron transfer and ion diffusion processes play a crucial role in determining the energy efficiency of the active materials. If both electrons and ions can access the active materials easily, especially at high current rate, we can fortify the supercapacitors power and energy performance.

1.3.1 Factors Affecting the Ragone Plots

From the equations below, we can simply conclude that the power density and energy density are closely related to the potential of the device (battery or electrochemical capacitors).

$$P = IV \quad 4$$

$$E = QV \quad 5$$

However, the potential will decrease due to the polarizations that occur as functions of the discharge current as shown in equation below:

$$V = \Delta V_{REV} - iR - \sum \eta_A - \sum \eta_C \quad 6$$

ΔV_{REV} represents the reversible potential (thermodynamic available potential)

iR represents the Ohmic polarization

η_A represents the activation polarization

η_C represents the concentration polarization

Three different kinds of polarizations are induced here.^{5,79} Ohmic polarization is caused by the internal resistances of the electrode materials and electrolyte solutions.

With increasing discharge current, the potential IR drop will increase linearly. If a

faradaic process is involved during the charge storage process, such as in battery and pseudocapacitor, activation overvoltage occur as a function of the current according to the Tafel equation:

$$\eta = b \ln i - b \ln i_0$$
$$b = \frac{RT}{\alpha F} \quad 7$$

i_0 is the exchange current density when activation overvoltage equals zero, and α is the transfer coefficient of the faradaic electrode process.

According to this equation, overvoltage increases with increasing current value, resulting in increasing loss of the energy device voltage.

The third polarization takes place associated with the depletion of the electrolyte ions near the electrode surface, especially at high charge current. When the local concentration of ions at electrode surface approaches zero, diffusion-limited maximum current is reached. The concentration overpotential η_C can be expressed as a function of the local ions concentration c_e in the equation below:

$$\eta_C = \frac{RT}{zF} \ln\left(\frac{c_b}{c_e}\right) \quad 8$$

When c_e is approaching zero, maximum current is reached, and concentration overpotential achieves a theoretically large value. Since current cannot increase anymore, power shutdown also comes along with the onset of the concentration polarization.

As a summary, all three polarizations will reduce the device voltage, and affect the energy and power performance. Figure 1.7 illustrates how power and energy are

influenced by the polarizations as a function increasing current as well as how the Ragone plot will be affected.^{5,79}

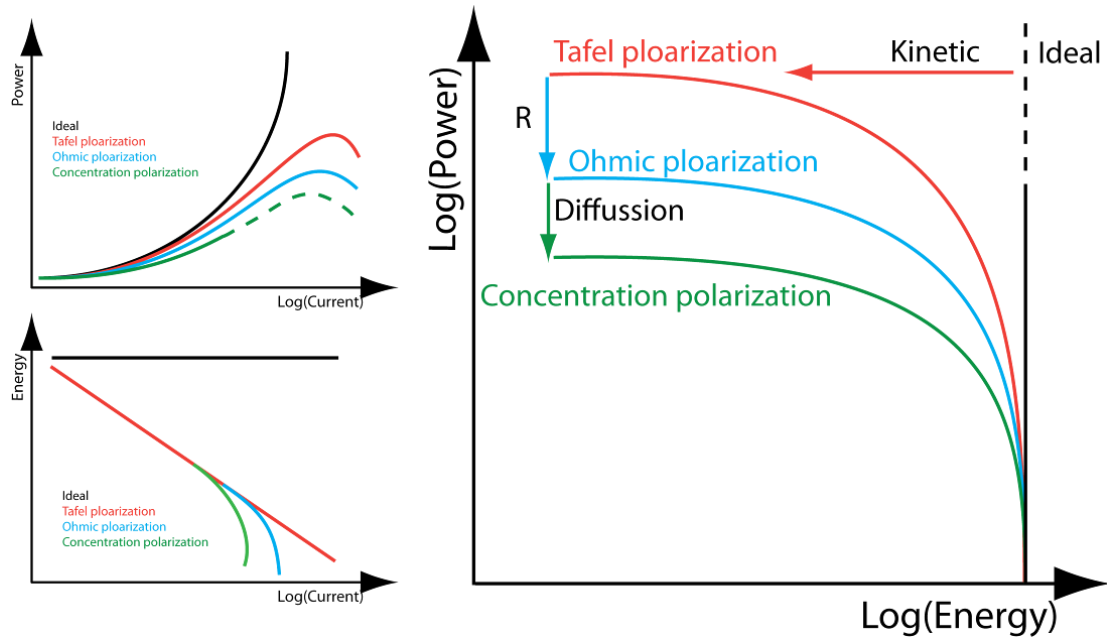


Figure 1.7 Contributions of polarizations on power and energy.

Left: Effect of ohmic, activation, and concentration polarizations on the power density and energy density as a function of current; right: effect of three polarizations on the Ragone plot (adapted from Conway et al.^{5,79})

Therefore, many efforts and research have been devoted to improve the electrical conductivity (reduce ohmic polarization) as well as the ion diffusion process (concentration polarization) of the energy storage systems. In the following sections, we will introduce the two main ongoing research directions in this field, including nanostructured materials fabrication and heterogeneous materials design.

1.3.2 Nanostructure for Ion Diffusion

With attempts to overcome the limitation of energy storage systems, including battery and supercapacitors, along with the fast development in solid state chemistry, nanomaterials have come into scientists' research interest. Many new results are reported using scale-down nanostructured electrode materials. It is believed that nanoscale size can bring the materials unique mechanical, electrical, and chemical properties, which give rise to profound influence on the EES performance.^{80,81,45,82,26,83,84} The main aspects affected by nanostructures are discussed below.

First, the high surface area of nanomaterials leads to a high contact area between the active materials and the electrolyte. As we discussed before, most charge is stored through the near surface fast redox process for pseudocapacitors. Therefore a high contact area is very desirable for higher specific energy storage. For example, given same amount of active materials, we can either fabricate a bulk structure or nanostructures like nanoparticles or nanowires as shown in Figure 1.8. The deep brown areas at the surface in all different structures present the most accessible active materials where faradaic redox reactions take place and contribute to the energy storage capability. We can see that a much larger portion of the total material will be active (presented by area in deep brown color) in the nanostructured ones, which means higher usage efficiency of the materials.

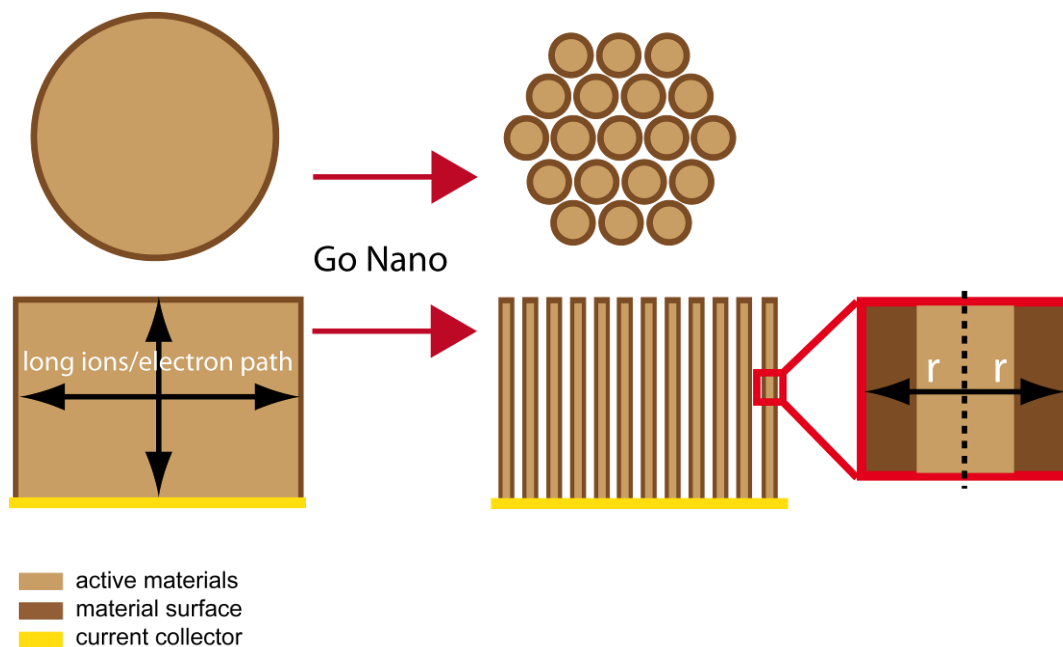


Figure 1.8 Comparing bulk and nanostructured materials for energy storage

For film and nanowires structure, the charge transfer path lengths are compared as indicated by the black arrows.

Another important merit of nanostructured materials is that both electron and ions will have shorter path lengths leading to the active site where redox reactions take place compared to bulk materials. As shown in Figure 1.8, for the film structure, ions have to diffuse a long distance to reach the inner material, and it is the same for the electrons. Therefore the usage of the inner materials, especially at high charge/discharge rate, is very limited. However, if we scale down the structure into nanowires shapes, ions do not have to travel a long distance before reaching the inner materials. As illustrated in the nanowire structures in Figure 1.8, ions can access the inner part through path that is vertical to the nanowire axial direction. The longest ion

diffusion path in this case equals to the radius of the nanowires, which can be fabricated down to tens of nanometer easily by multiple methods. The importance of electron and ion transfer associated to the device performance in term of power and energy density are discussed in section 1.3.1. Improvement on the electron/ions transfer will decrease the ohmic polarization and concentration polarization terms in a complex way. Therefore higher power and energy density are expected when nano technology are brought into energy storage devices.

Nanostructured materials can buffer the mechanical stress in a more efficient way, resulting in better cyclability. As discussed in the mechanism part in section 1.2, the pseudocapacitance involves the ion insertion/desertion process, which usually comes along with a volume change at different extent. This issue becomes more serious in batteries where the bulk materials are involved during charge/discharge processes. Nevertheless, even for supercapacitors, better strain buffering is always desired for good cycling stability. As shown in Figure 1.9, for bulk structure, cracks occur after a long time cycling due to the strain produced by the volume change. While for nanowires structure, volume change stress can be effectively buffered by the nanostructures even after long time cycles.

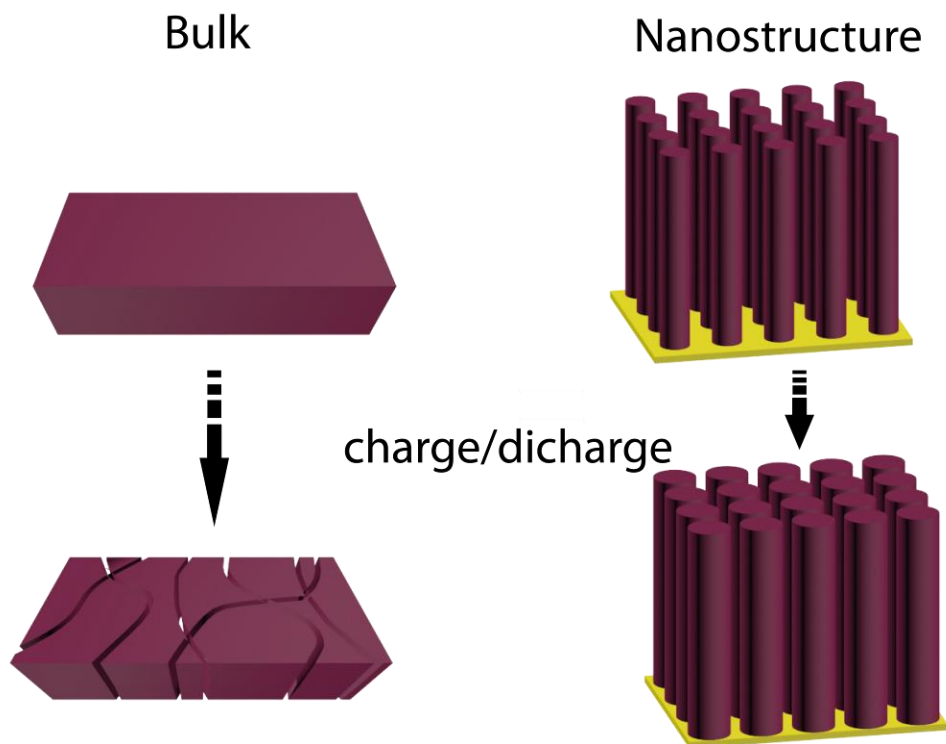


Figure 1.9 Stress buffering ability of bulk and nanostructured materials

Left: cracks occur in thick film due to strain induced after charge/discharge cycles; right: nanowires with good strain buffering maintain the structure well after cycles.

Various different nanostructures have been explored for application as battery and supercapacitor materials, including 0D, 1D, 2D,3D types as discussed by Liu.⁸⁵ In Figure 1.10 we show the nanostructure types with different dimensionalities. Nanoparticles usually require conductive additive (i.e. carbon black) to ensure good electron pathways as well as a binder material to maintain mechanical stability, especially for materials with poor conductivity. For thin film structures, this is not very practical, due to the poor mass loading per area. However, increasing film

thickness is also problematic; it is reported that for MnO₂ film supercapacitor electrode, the specific capacitance by mass decreases with increasing film thickness,^{86,87} and if the thickness goes up to micrometers, there is no redox reaction in the inner layer.⁴⁶ The maximum area capacitance reported for film MnO₂ electrode is only around 50 mF cm⁻¹. Well arrayed 1D nanowires/ nanotubes architectures are gaining more and more interest with the fast development of deposition techniques. Compared to nanoparticles, nanowires can sustain good connection to the current collector without adding any additive that contributes to the total mass. At the same time, ion diffusion process is facilitated with the large surface area and short inner diffusion length within the 1D arrays, overcoming the thickness limitation for the 2D film structure and approaching high mass loading requirement. 3D porous structures have also been applied to supercapacitors. Chen et al. reported the fabrication of MnO₂ grown into nanoporous gold substrate and show a high specific capacitance up to 1145 F/g, which approximates the maximum theoretical value for MnO₂ material.⁸⁸

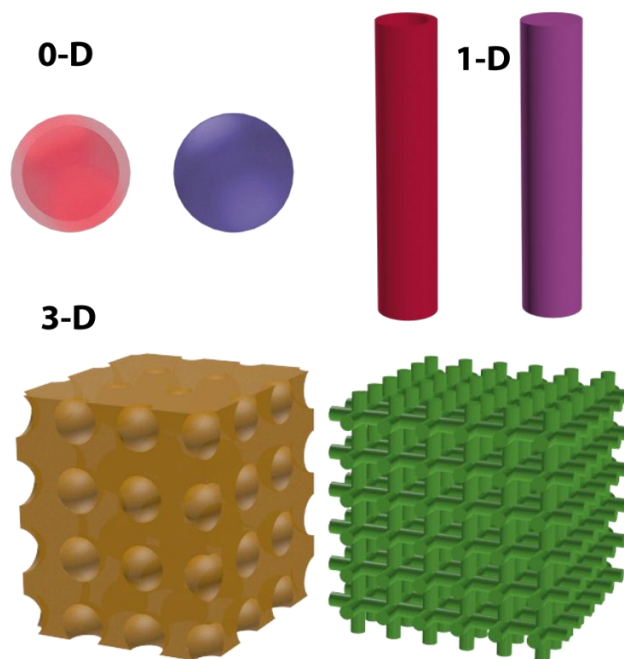


Figure 1.10 Illustration of different nanostructure defined by dimensionalities.

Many synthesis methods have been reported to fabricate nanostructures. Solution based-methods like sol-gel and electrochemical deposition with the assistance of soft/hard templates or with presence of surfactant are widely used. Some of the typical used templates include anodic alumina oxide (AAO) (see chapter 2.11) and polycarbonate templates.

With the fast development of technology, advanced techniques like CVD, ALD start to attract interest for the scientific study of energy storage process and scale-up capability. In 2009, Banerjee reported the fabrication of full metal-insulator-metal electrostatic nanocapacitors by CVD and ALD techniques within AAO template.⁸⁹ Additionally, a CVD technique for 3D batteries and supercapacitors was patented in 2011.⁹⁰ The precise control of the conformal deposition at nanoscale of these

techniques is very important for the development of micro energy storage devices as well as for studying the reaction mechanisms and structural evolution during the charge/discharge process. For example, Huang et al. have reported a lot of in-situ lithiation/delithiation research on a single nanowire.⁹¹⁻⁹⁴ In these works, CVD was utilized to grow individual well defined nanowires, which were later used to for studying the *in situ* charge/discharge process with tracking of the phase propagation and volume changes.

1.3.3 Heterogeneous Materials with Synergistic Properties

Beside the limitation caused by the structure, the intrinsic chemical and physical properties of the active materials also affect and most time dominate the performance of the materials. Through the design of heterogeneous materials, we can target synergistic properties that can be brought by the composite materials. The research in heterogeneous material has been widely explored in both battery and supercapacitors fields. In order to achieve most of the desirable properties of the composite materials, small scale integrated architecture is tailored and nanostructures are chosen and fabricated. Nanostructures of different dimensionalities (as shown in Figure 1.9) have been applied with each hybrid component material integrated in different ways, resulting in architectures like core-shell nanoparticles,⁹⁵⁻⁹⁷ coaxial nanowires/nanotubes,⁹⁸⁻¹⁰² and meso/microporous structures.¹⁰³⁻¹⁰⁷ Different combinations of energy materials are engineered for one or a few of the following demands: mechanical stability, cyclability, electrical conductivity, good ion diffusion, high surface area. Take PEDOT for example. The theoretical maximum capacitance

is around 200 F/g based on doping level of 0.3 electrons per unit, which limits the energy density. With PEDOT (doped with perchlorate ions) as an electrode material, 90 F/g was reported for bulk film¹⁰⁸ and performance improved to 110 F/g for nanowires arrays structure and 140 F/g for nanotubes.^{109,110} With design of heterogeneous materials of PEDOT integrated with high energy density materials, higher capacitances up to 250 F/g with MnO₂,¹¹¹ and 640 F/g with RuO₂ can be achieved.¹¹² For MnO₂, the power performance is limited due to the relatively poor electrical conductivity (i.e. 10⁻⁵ -10⁻⁶ for MnO₂).⁵⁷ Therefore heterogeneous materials hybridized with conductive materials like carbon based materials (including carbon nanotubes, mesoporous carbon, graphene),¹¹³⁻¹¹⁸ and conductive polymers^{119,120,111} are widely explored through all kinds of architectural structures. Again, the emphasis of this heterogeneous nanomaterials approach is to pick the proper materials with desired properties and integrate them into an effective architecture that can fully exploit the advantages. Both the materials' intrinsic properties and the structures play crucial roles in the materials optimization for success of future energy storage development.

1.4 Approach Overview

As discussed above, the ion diffusion and electron transfer processes are playing significant role in determining the energy material's performance. The following chapters of this thesis introduce mainly 2 approaches applied to facilitate the charge transfer process, including substrate approach and heterogeneous 1D nanoarrays approach.

The well-ordered, free-standing 1D nanoarrays synthesized within AAO template by different deposition technologies are intensely explored in our group. As documented in section 1.3.2, nanostructure is favorable for the charge transfer process through the nano-scale pathway; at the same time, 1D category shows some advantages over other dimensional nanostructure in terms of loading amount and packing efficiency. The AAO technology has been widely used in our group to pursue this goal. Ran has reported the synthesis of coaxial PEDOT/MnO₂ nanowires and RuO₂ loaded PEDOT nanotubes.^{121,112} In both of these heterogeneous materials, electron transfer pathway was enhanced through the conductive PEDOT shell. In most recent works, MnO₂/ TiN nanotubes was fabricated with TiN acted as a under layer which functioned to facilitate the electron transfer to the MnO₂.¹²² The strategy used in these previous works is adding additional conductive layer (PEDOT, TiN) for the electron transfer. In chapter 4, we induced an alternative way to improve the overall electrical conductivity of MnO₂ by a simple electro co-deposition process, resulting in RuO₂-MnO₂ composite nanowires, followed by its electrochemical properties studied in a comprehensive way. A general route for fabricating metal oxide-polymer nanowires was demonstrated and discussed in chapter 5. Besides applying fabrication on the active material itself, we also explore the approach of device substrate. The substrate approach was discussed in chapter 3 with cellulose fibers, which turn out to function well as an internal electrolyte reservoir, and manifest enhanced electrochemical properties.

Chapter 2: Fabrication and Characterization of 1D Nanostructured Supercapacitor materials

2.1 1D Well-ordered Nanoarrays Materials Synthesis

As discussed in chapter 1, fabricating well-ordered 1D nanostructure with lateral dimensions that fall within 1-100 nm is a very promising strategy for energy materials engineering in terms of good electrochemical properties, high mass loading and good integrity. Many different chemical methods have been applied to generate 1D nanostructures through “bottom-up” approaches.¹²³ Both soft templates and hard templates are widely used to direct the one-dimensional growth of a variety of materials. Anodic alumina oxide (AAO) templates combined with electrochemical deposition technology explored here provide a simple, straightforward growth method for well-ordered 1D nanoarrays, of which material amount, dimension size and areal density are tunable. Good connection with the current collector is also guaranteed through the direct electrochemical deposition on top of working electrode. The unique structure of AAO and its anodic fabrication process will be discussed below followed by its utilization in the electrochemical deposition of energy materials.

2.1.1 AAO Template

Anodic alumina oxide is at the forefront of the commonly used hard templates for the synthesis of 1D nanowires/nanotubes arrays. The porous alumina template has hexagonal closed-packed pores with pore density at magnitude between 10^9 to 10^{11} cm^{-2} .¹²⁴ The good uniformity and high pore density are very important for the template synthesis of high loading well-ordered 1D nanostructures. The template is

prepared by electrochemical anodization of aluminum film using acidic electrolyte under certain temperature and time. Pores are formed during the anodization process where local dissolution of alumina oxide occurs. The pore size can be tailored from tens of nanometer to hundreds of nanometer by adjusting the anodization conditions, such as electrolyte solution, anodization time, temperature and anodization potential.¹²⁴

The most widely used two-step anodizing procedure for preparing high-ordered arrangement of nanopores consists of a multistage process: pre-treatment, anodization, post-treatment, as illustrated in Figure 2.1. During the pre-treatment, the aluminum foil is annealed under non-oxidizing atmosphere, degased, and electropolished to remove any surface defect. Then a two-step anodizing procedure is carried out to grow well ordered porous structure. The first anodizing step is followed by chemical etching to produce a periodic concave pattern to direct the pore growth during the second anodizing step. The post-treatments include the aluminum base removal, pore-widening and barrier layer removal.

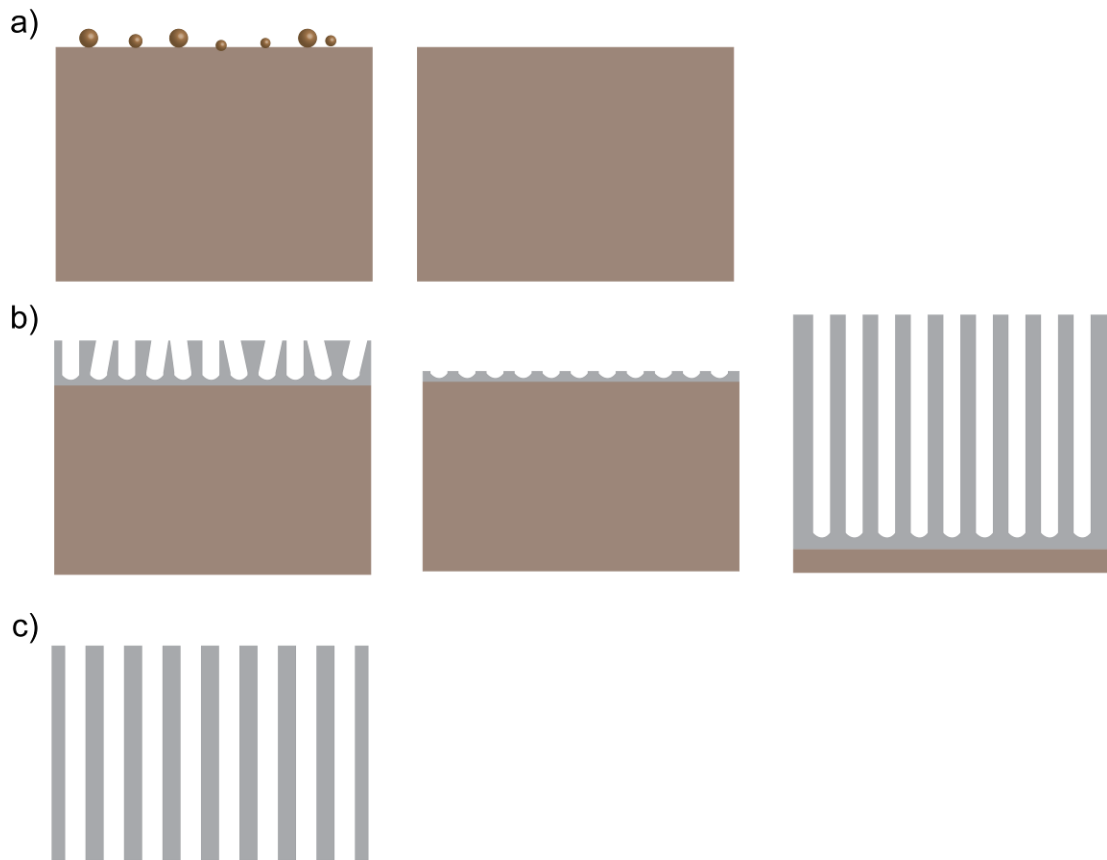


Figure 2.1 Schematic illustration of the two-step anodizing process for AAO.

(a) Pre-treatment, (b) two-step anodizing, (c) post-treatment.

The most commonly used electrolytes for two-step anodizing includes sulfuric acid, oxalic acid, and phosphoric acid. In Figure 2.2, we show the SEM images of AAO templates prepared in oxalic acid. Figure 2.2 a-c show the top view of the porous structure. The pore diameter is around 50 nm. In image d, e, we can see the cross-section of the parallel channel structure. And Figure 2.1 f shows the barrier layer at the bottom of the film, from which we can clearly identify the close packed hexagonal units.

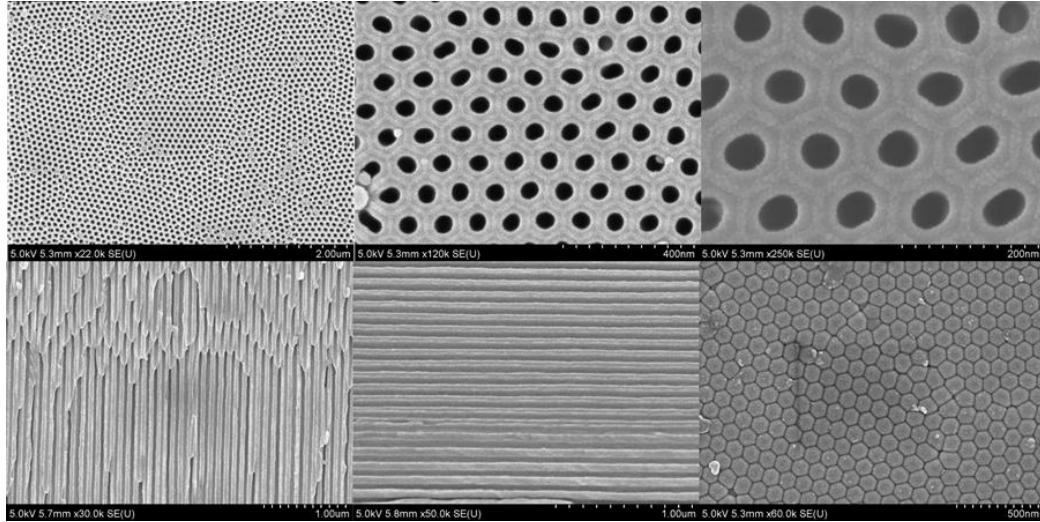


Figure 2.2 SEM images of homemade AAO

(a-c) top-view, (d, e) cross view of the pores, (f) bottom view of barrier layer. Film prepared by two-step anodizing process in oxalic acid for 20 hours.

Many aspects of the AAO architecture can be tailored, including pore size, pore uniformity, pore aspect ratio, template thickness, and porosity. Instead of producing a uniform parallel pores structure, porous AAO with control over both vertical and horizontal direction can also be fabricated by adjusting the anodizing conditions, resulting in unique architectures of step-pore size or different pore growth direction. In figure 2.3, we list several porous structures as examples to show the facile controllability of AAO nanoarchitecture. Figure 2.3 a, b show the controllable modulation in pore size realized by alternating the “hard” an “mild” electrochemical etching conditions, the so-called pulse anodization^{125–128} And the multi-branched Y structure in Figure 2.3 c, d is synthesized by sequentially reducing anodizing potential during anodization of the aluminum.¹²⁹ 3D interconnected porous AAO is also

fabricated by post-chemical etching that selectively occurs at certain location.¹³⁰
 Modification of the barrier layer is also explored and results in the “tree” morphology of pore channels as show in Figure 2.3 g, h.¹³¹

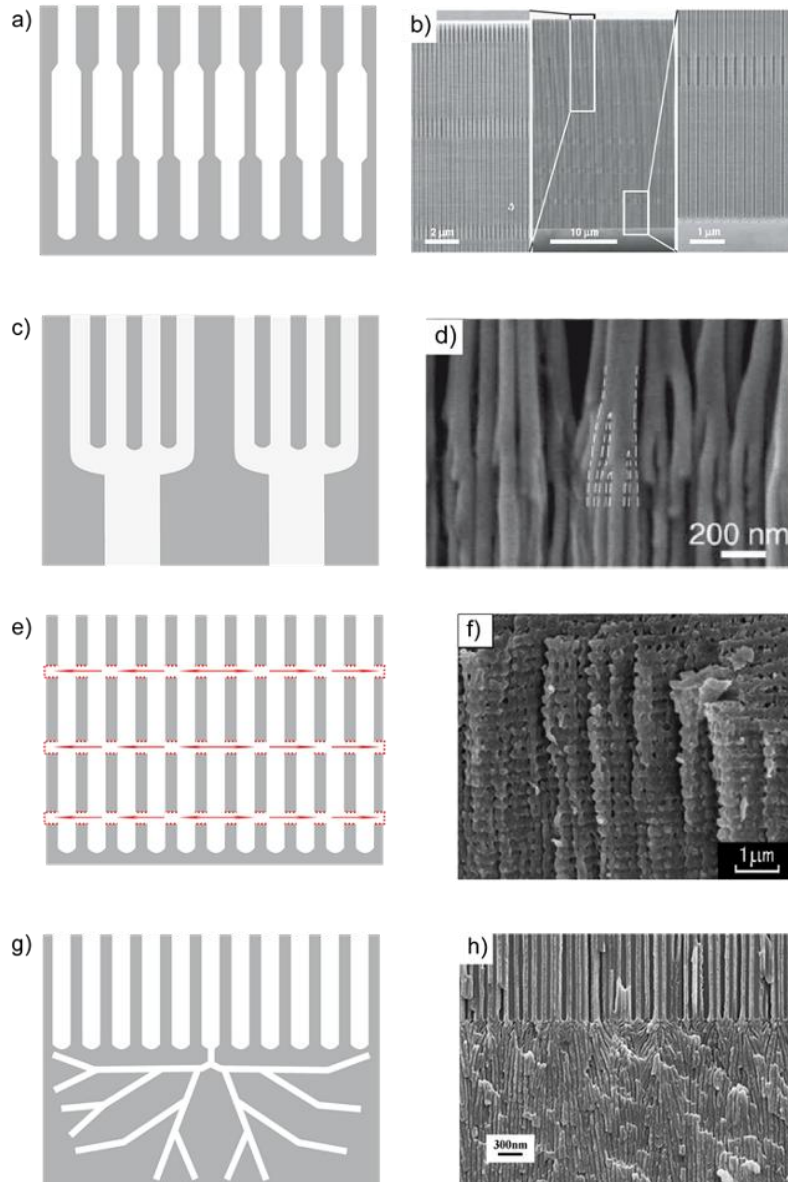


Figure 2.3 Graphic and SEM images of novel porous alumina structures

(a) Step pore size, (b) Y branch, (c) 3D interconnected, (d) tree morphology of pores.

(Adapted from reference¹²²⁻¹²⁸)

2.1.2 Electrochemical Deposition

Electrochemical deposition is one of the most commonly used methods that can be applied to grow metals, alloys, semiconductors, and conductive polymers. Electrodeposition has many superior merits, such as low cost, low temperature requirement, fast deposition rate, controllability over size and shape, and deposit uniformity. During the electrodeposition process, ions as precursor will be either oxidized or reduced at the electrode/electrolyte interface. This solid/liquid interface reaction leads to the conformal growth of the electrochemically synthesized material with high purity. Different electrochemical techniques including galvanostatic method (constant current), potentiostatic method (constant voltage), and cyclic voltammetry can be applied for synthesis to realize the kinetic/ thermodynamic control over the growth. Both the deposition rate and amount can be well defined by tuning the electrochemical parameters, such as potential, current density, and charge amount.

One of the most attractive qualities of electrodeposition is its great potential in synthesizing nanomaterial either by template-assisted method or template-free method. Hard templates are widely applied to define the shape the material is growing into during electrodeposition. By using a thin film current collector, we will obtain a film of electrodeposited materials growing on the top. If we add a hard template on top of the thin film current collector, material can only be synthesized within the defined space in the template. Based on this, our group has developed an AAO-assisted electrodeposition set-up to grow 1D-nanostructures of different materials. As shown in Figure 2.4, the electrochemical synthesis is carried out in a three-electrode

system. Ag/AgCl is the reference electrode, and platinum is used as counter electrode. The working electrode is an AAO template with Au sputtered on one side, acting as a current collector. The active deposition window is sealed and defined by sandwiching between two pieces of silicon rubber and stabilized by glass and polycarbonate pieces. After applying the electrodeposition condition, the material starts to grow within the AAO pores. AAO removal can be easily processed afterwards with NaOH solution, and well ordered-1D nano-arrays can be obtained. By adjusting the current collector electrode shape (ring-shape or flat-top shape), and bath composition, we can tailor the 1-D structure between nanowires and nanotubes for metals, alloys, and conductive polymers. Another great merit of ECD is that we can realize the fine-tuning of heterogeneous nanocomposites structure synthesis within 1D domain. We have discussed the importance of heterogeneous nanomaterials with synergistic properties for energy applications in chapter one. ECD has shown good controllability of directing composite materials growth within AAO template with different heterogeneous architectures. For example, by using ring-shape Au electrode, we can grow coaxial PEDOT/MnO₂ nanowires through the selective site growth of PEDOT on the Au ring edge. Also we can co-deposit MnO₂-RuO₂ heterogeneous nanowires by using electrodeposition bath containing both manganese and ruthenium cations as will be discussed in chapter 4.

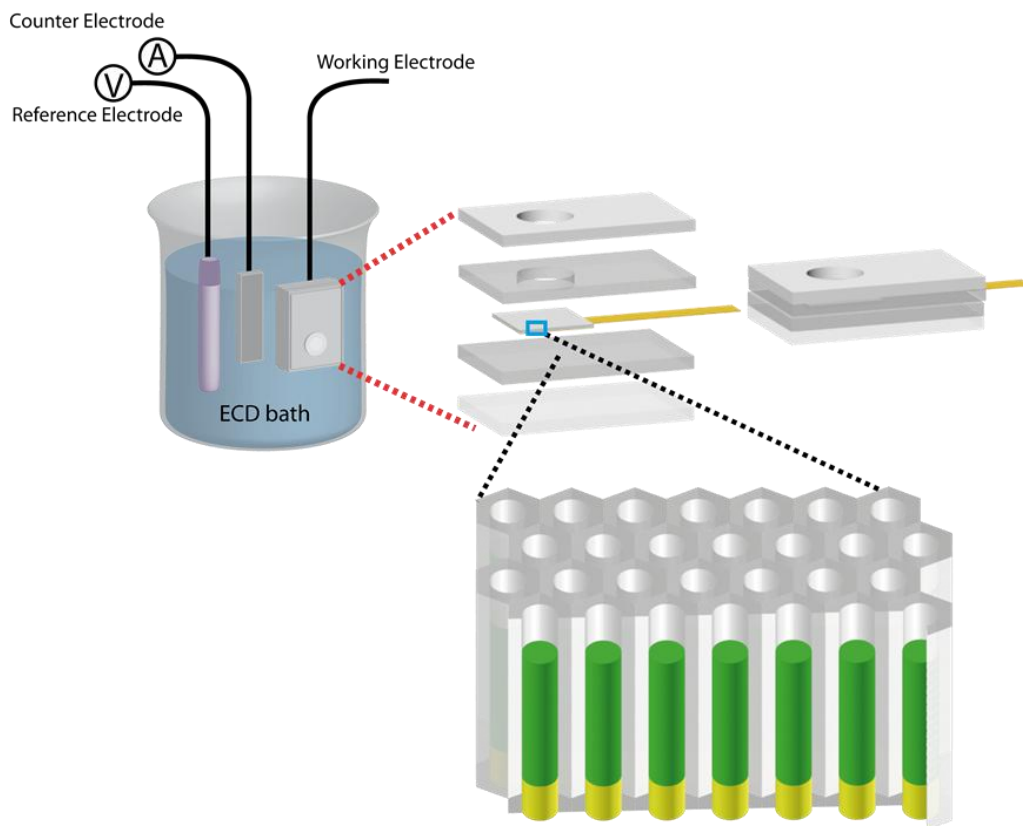


Figure 2.4 AAO assisted electrodeposition set-up

2.2 Characterization of Nanostructure Materials

With the fast development and promising prospect of nanomaterials, advancement in characterization techniques at nanoscale has been achieved accordingly. The forefront technology in this field for energy material involves the utilizations of multiple analyzing techniques at the same time, realizing the *in situ* characterization during the electrochemical reactions. The following sections describe the main structural and chemical characterization methods applied in our materials study.

2.2.1 Structural Characterization

As we discussed in chapter one, the structure, especially at nanoscale with high aspect ratio, will influence the material's electrochemical performance in a significant way. Therefore structural characterization is a very important part in understanding the material's electrochemical behaviors. Here microscope techniques are applied to investigate the material size, morphology and physical features.

2.2.1.1 SEM and TEM

Electron microscopy has proved invaluable for characterizing the structure of materials, especially at the nano-scale. Two main microscopy techniques, Scanning Electron Microscopy (SEM) and Transmission Electron Microscopy (TEM) are discussed below.

In a Scanning Electron Microscopy (SEM), a focused electron beam is scanning simultaneously in two perpendicular directions across the sample. Secondary electrons (SE) and backscattered electrons (BSE) signals are collected by the detector and converted into images that show the surface topography of the structure. Image resolution typically between 1 nm and 10 nm can be achieved in a modern SEM. For 1D array materials grown in AAO template, the SEM sample is prepared by the following steps: first, the AAO template with deposited materials is attached to a carbon tape or a parafilm with Au sputtered AAO side down to hold together the Au thin layer and 1D arrays. Then the AAO is removed by soaking the template in 3M NaOH for 20 minutes and generally rinsing with distilled water to remove any residue until pH reaches neutral. Following that, the arrays is rinsed with a drop of water,

ethanol, acetone, and ethyl acetate by sequence to obtain well standing, separate nanowires/nanotubes arrays without nanowires/nanotubes gathering together. The sample is left in air to completely dry before SEM.

In a transmission electron microscopy (TEM), a high-energy electron beam penetrates a thin specimen (10nm to 1 μm) after interacting with the sample and is then imaged by lens, and magnified on to an imaging device for direct observation (e.g. fluorescent screen). The image can be permanently recorded using a photographic film or in an electronic image recording device based on charge-coupled devices (CCD). TEM images provide more internal structure information compared to SEM, and can reach an even higher image resolution down to sub-Angstroms, advancing the capability for atomic-scale structure investigation. For example, TEM can identify partially tubular structure which SEM cannot. TEM can also be used to investigate the material's crystal structure by high resolution TEM (HRTEM) and selected area electron diffraction (SAED) techniques. TEM samples are prepared by dispersing the 1D nano-array in ethanol/water mixture and dropping 20 μL of the obtained suspension solution each time on to carbon coated copper TEM grid, and wait until air-dry for use. (Repeating the drop-cast procedure if necessary.)

In Figure 2.5, we show SEM and TEM images of Ni nanotubes.

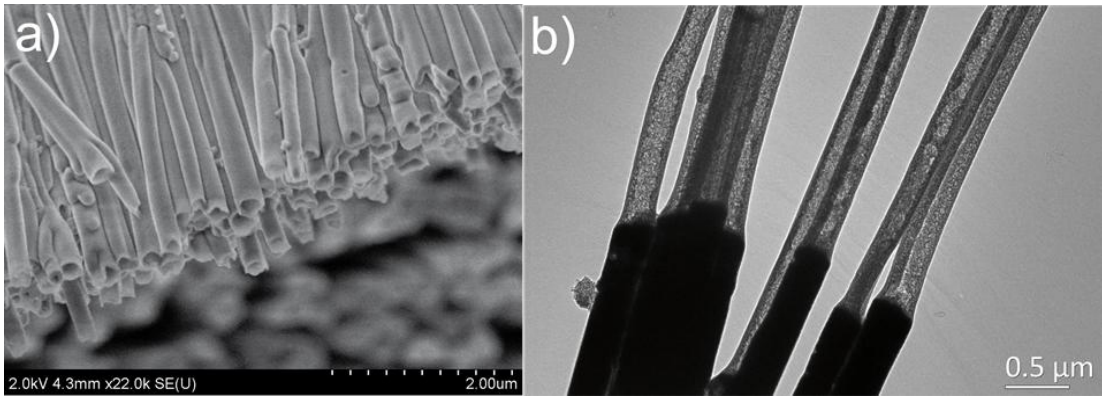


Figure 2.5 SEM and TEM image for 1D nanoarrays

(a) SEM and (b) TEM image of Ni nanotubes.

2.2.2 Chemical Compositions Characterization

The chemical composition is characterized by multiple analyzing techniques at both qualitative and quantitative levels. The distribution of different components and metal charge states can also be determined by different spectra techniques. Typical characterization results of element distribution and spectra are illustrated in the following discussion.

2.2.2.1 EDS

X-ray energy dispersive spectroscopy (EDS) is a very useful elemental analysis technique to investigate chemical compositions and elemental distribution of a sample. EDS can be carried out within SEM or TEM functionalized with a X-ray detector. Both quantitative and qualitative content information can be obtained based on the unique X-ray energy characteristic peak associated with different elements and

the relative count of detected X-ray from the electron bombardment of sample elements. Different modes of elemental analysis can be carried out within SEM or TEM microscopies, including spectra (over area or dots), line scan, and elemental mapping. For a TEM-EDS line scan across a single nanowire or nanotube, different intensity spectra will be obtained. As illustrated in Figure 2.6, for a nanowire structure, the X-ray intensity from the main component element will give a highest peak in the middle attributing to the largest thickness electrons penetrate through. Meanwhile, for a nanotube structure, the highest intensity peaks will show at the two edges corresponding to the shell of the nanotubes.

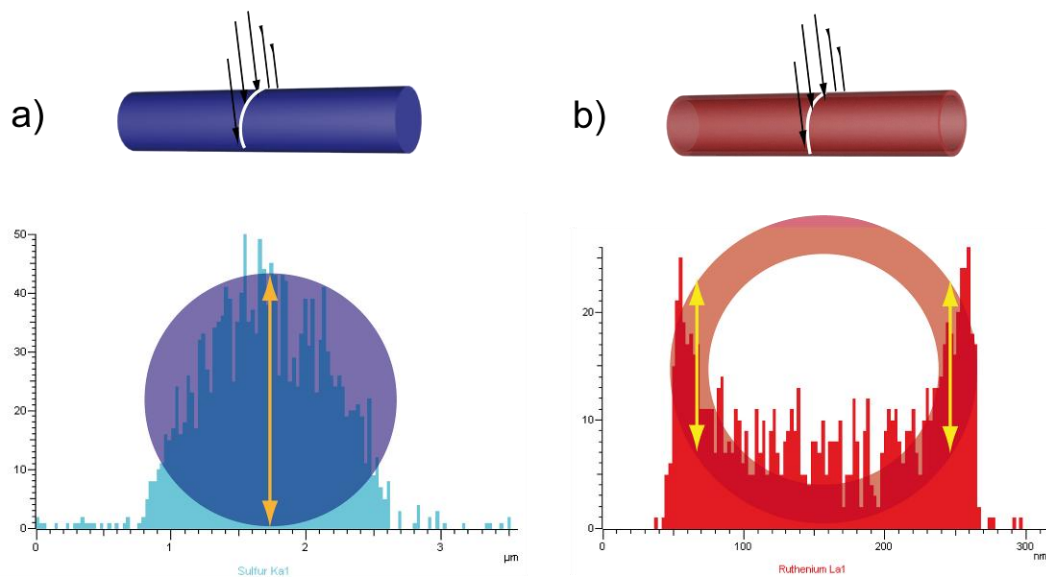


Figure 2.6 EDS line scan across a single nanowire or nanotube

(a)EDS line scan across a nanowire, (b) EDS line scan across a nanotube. The yellow arrows indicate the thickness the electrons are passing through. With increasing thickness, a high element signal will be obtained, and showing the corresponding intensity response features for nanowire and nanotube shape.

2.2.2.2 XPS

X-ray photoelectron spectroscopy (XPS) is a surface sensitive spectroscopic technique that can be used to analyze the chemical composition, electronic state, and empirical formula of material at the surface region (1-10 nm thick) of the sample. A beam of X-rays is applied to irradiate the specimen and the number and kinetic energy of the escaped electrons (termed photoelectron) are measured simultaneously. The binding energy (BE) of the photoelectron is determined by subtracting the kinetic energy and working function (instrumental correction term) from the X-ray photon energy. A plot of the electron count versus the BE is then plotted where each BE is characteristic for a core atomic orbital of certain element. Therefore chemical composition and electronic state can be determined. Meanwhile the quantitative information of the surface composition can be calculated by integrating the peak area of BE associated with different elements. For example the O^{2-} 1s peak and the Ru 3p peak can be used to determine the empirical formula of unknown ruthenium oxide. Sometimes overlap occurs between different element's BE spectra, for example the Ru 3d will overlap with the C 1s spectra due to adventitious carbon. In this case, deconvolution is performed to analyze the XPS data. Figure 2.7 show the deconvoluted XPS spectra for Ru 3d in sample of PEDOT-RuO₂ nanowires, which is interacted by the C 1s signal.

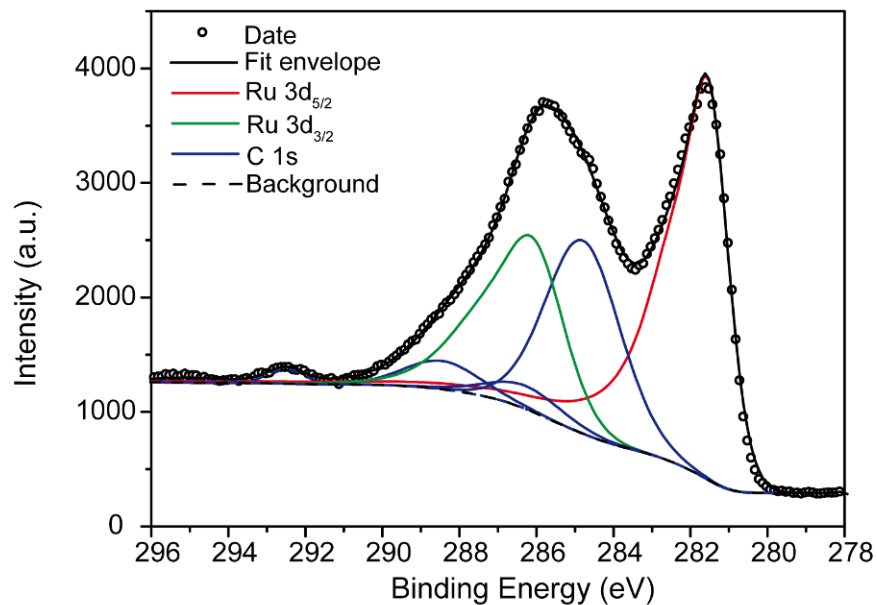


Figure 2.7 Deconvoluted XPS spectra

XPS spectra of Ru 3d and C 1s in PEDOT-RuO₂ nanowires samples

2.2.2.3 Raman

Raman scattering refers to the frequency shift of the emitted photon away from the incident radiation. Typically, a monochromatic laser light is used to excite the electron from the ground state to a virtual energy state, and most electrons will relax back to the same ground state and emit photons of same wavelength as the laser light used. This process is called Rayleigh scattering. However a small portion of the excited electrons will relax to a higher or lower vibrational state, resulting in a frequency decrease (so called Stokes scattering) or increase (Anti-Stokes scattering) of the emitted photons. The Raman shift is caused by a molecular vibration and is directly related to the vibrational state of the molecules. Therefore Raman

spectroscopy can be applied to study the intermolecular vibration, and provide structural information of inorganic and organic compounds. In my research, Raman is mainly utilized to identify the phase of MnO_2 . Birnessite phase of MnO_2 synthesized by electrochemical deposition is confirmed by Raman spectra. A typical spectrum for birnessite MnO_2 is shown below in Figure 2.8. The sample preparation is very simple. An as prepared sample for electrochemical characterization can be directly used for Raman characterization after air-drying overnight.

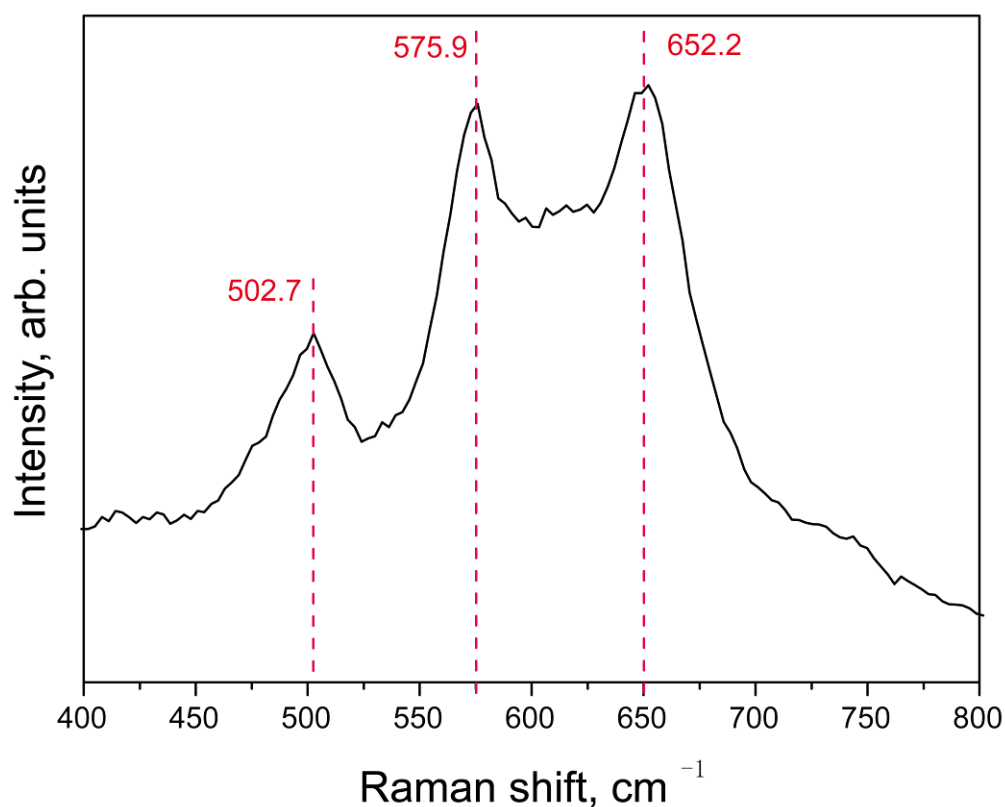


Figure 2.8 Raman spectra of electrodeposited MnO_2 with birnessite phase.

2.2.2.4 ICP-AES

Inductively coupled plasma atomic emission spectroscopy (ICP-AES) is a qualitative and quantitative analysis method for trace elements. A known volume of aqueous solution which contains sample elements is prepared and delivered by a peristaltic pump, which is then transferred into aerosol mist form in the nebulizer before being injected into the plasma flame. The plasma is composed of charged ions and electrons with temperature up to 10000 K, and will dehydrate, ionize/ atomize the injected analyte and excite the atom to excited state. When they relax to ground state, the wavelength and intensity of the emitted electromagnetic radiation are recorded which are characteristic for the element's electron configuration and its concentration in prepared solution. The advantages of ICP-AES includes low detection limit down to ppm concentration for certain elements, and the capability of simultaneous multi-elements detection.

The sample preparation for ICP-AES is carried out with great caution and care. Our free standing nanowires arrays containing metal elements (Mn or Ru) are firstly dissolved in freshly prepared aqua regia solution made of 3:1 concentrated HCl/HNO₃ and diluted by distilled water to certain volume. Meanwhile, standard solutions of analyzed elements at different concentrations are prepared with dilute HCl/HNO₃ aqueous solutions. The element concentration is obtained from the calibration curve made from the standard solutions. A calibration curve of Ru is shown in figure 2.9 using the emission wavelength at 240.272 nm.

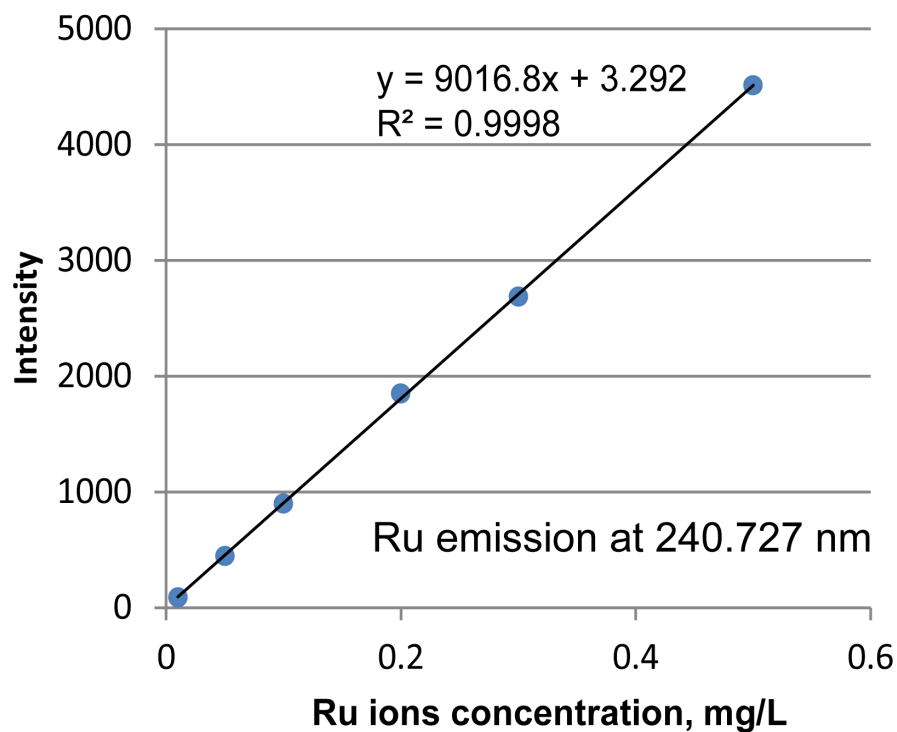


Figure 2.9 Calibration curve for Ru element

Concentrations from 0.01 to 0.5 mg/L were prepared in this calibration experiment.

2.2.3 Electrochemical Characterization

The electrochemical performance of supercapacitor materials is mainly characterized by a capacitance value which can be calculated based on cyclic voltammetry (CV) or galvanostatic charge/discharge (GV) data as will be described in the following section. Electrochemical impedance spectroscopy measuring the current response to voltage perturbation is also applied to gain insight into material electrochemical properties through equivalent circuit modeling.

2.2.3.1 GV and CV

Galvanostatic charge/discharge and cyclic voltammetry are two main electrochemical characterization methods for supercapacitor and battery. Both measurements can be carried out in either three-electrode or two-electrode systems. In a galvanostatic voltammetry measurement, the working electrode is charging and discharging at constant current within defined potential window. Typical GV curves for a supercapacitor and a battery are compared and shown in Figure 2.10 a. The difference in curve shape can be explained by their different charge storage mechanisms. The supercapacitor accumulated charge across the voltage window through double layer charge or fast surface redox reactions, while for battery, the charge is stored at a particular potential where the ion insertion and desertion occur accompanying by the phase transition. The capacitance can be calculated by the following equation,

$$C = \frac{it}{V} \quad 9$$

Where I represents current applied (A), t stands for the charge or discharge time (s), and V is the potential window tested (V).

Accordingly, CV cures of supercapacitors and batteries also show different current response to the line modulation of potential in time. Supercapacitors show rectangular mirror-image compare to the sharp peak feature found for battery as shown in Figure 2.10 b. Capacitance can be calculated based on the equation:

$$C = \frac{\int idV}{v\Delta V} \quad 10$$

Where charge is calculated by taking the area integral of the CV curve and divided by scan rate v (V/s) and the voltage window used. Note that the CV curve will deviate from the ideal square shape when pseudocapacitance is involved. A pair of broad peaks may appear due to the fast faradaic reaction that take place.

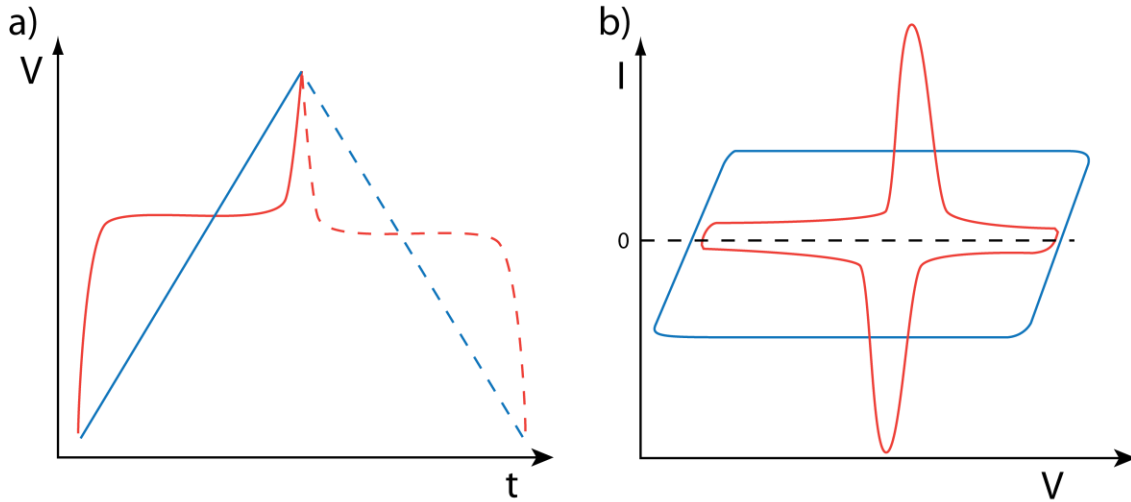


Figure 2.10 Typical GV and CV curves

(a) Galvanostatic charge/discharge (GV), (b) cyclic voltammetry (CV) curves for supercapacitor (represented by the blue curves) and battery (represented by the red curves).

Since the voltage of a supercapacitor is directly related to the charge state of the electrode, rather than staying at a singular value as for a battery, the energy stored in supercapacitor is different from battery even if both systems are charged to same potential with same amount of charge. As illustrated in Figure 2.11, plots of potential

versus the charge state for both supercapacitor and battery are compared. The energy can be calculated based on equation:

$$E = \int Vdq \quad 11$$

Therefore the energy stored by the supercapacitor is only half of the battery when same charge and device potential are defined.

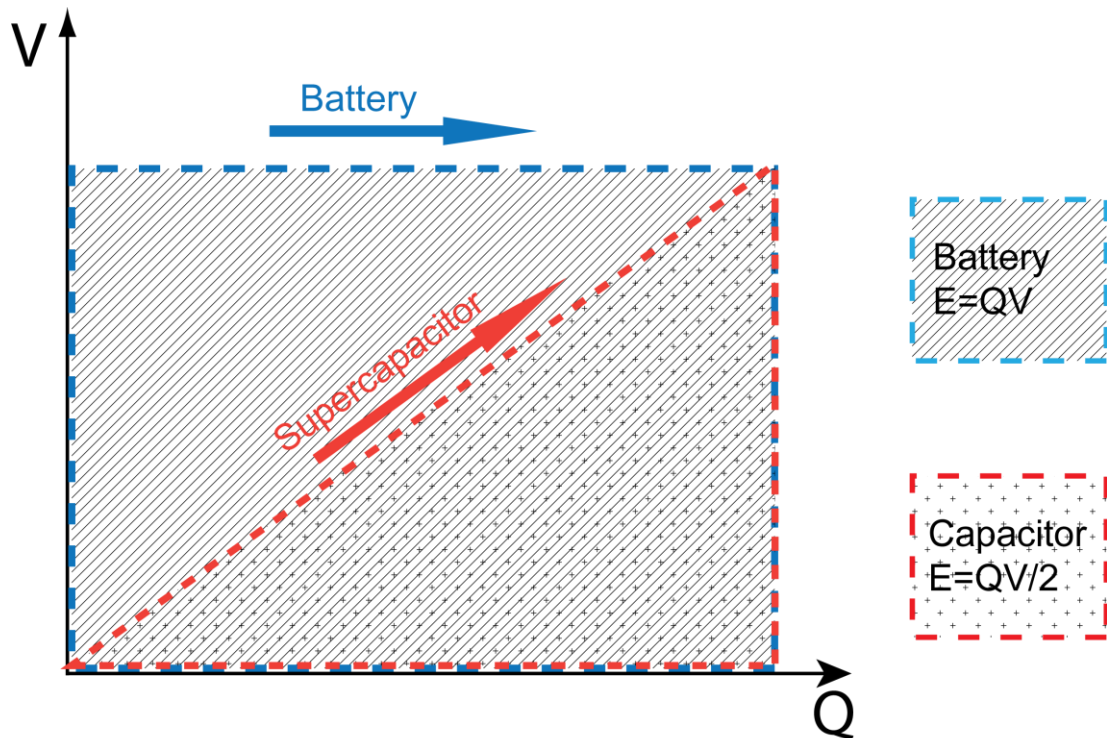


Figure 2.11 Illustration of the energy stored in supercapacitor and battery

Energy is presented by the under area size of plots of device potential versus charge accumulated.

2.2.3.2 Electrochemical Impedance Spectroscopy

During an electrochemical impedance experiment, the magnitude and phase relation of an ac current generated in response to an applied low amplitude alternating voltage (typical 5 mV) is evaluated and recorded by a phase-sensitive recording device. A complex-plane plot of imaginary (Z'') versus the real (Z') resolved components of $|Z|$ over the range of frequency studied, called Nyquist plot, is produced to interpret the impedance behavior of electrochemical system based on equivalent circuit modeling. In figure 2.11, we list several simple circuits and their Nyquist plots. In the case of a simple series RC circuit (Figure 2.11 a), Nyquist plot shows a vertical line with Z' intercept indicating R value. For a simple parallel RC circuit in Figure 2.11 b, a semicircle is obtained with diameter of the semicircle equals to the resistance R. Electrochemical components for a supercapacitor involves: double-layer capacitance, C_{dl} ; Faradaic charge transfer resistance, R_{ct} ; solution resistance, R_s . A typical circuit for electrochemical capacitor and corresponding Nyquist plot are shown in Figure 2.11 c. R_s , R_{ct} values can be directly determined from the plot. However, interpreting the impedance behavior by equivalent circuit and modeling is arbitrary and limited by many factors, especially when complex systems are studied. Therefore we use the impedance measurement for the main purpose of side-by-side comparison electrochemical properties of similar systems, different by one changeable factor at a time, such as electrical conductivity or ion accessibility.

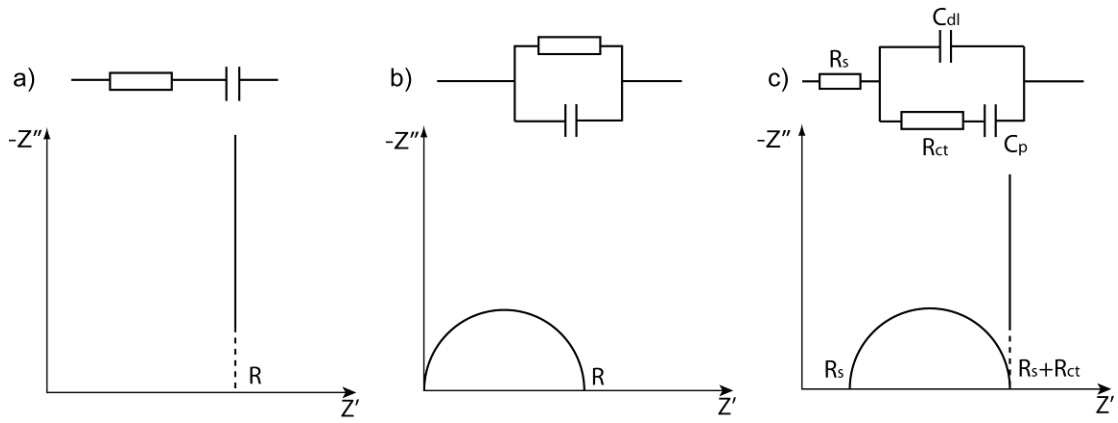


Figure 2.12 Simple equivalent circuits and their Nyquist plots.

(a) Series RC, (b) parallel RC, (c) ECs circuits

Chapter 3: Natural Cellulose Fibers as Substrate for Supercapacitors

** This is a joint project cooperated with Dr. Hongli Zhu (in co-first authorship) from Professor Liangbing Hu's group at Department of Materials Science and Engineering of University of Maryland. Dr. Zhu's equal contribution in this work includes fabricating the cellulose paper, conducting the CNT coating, and characterization of the conductive paper before MnO₂ deposition.*

3.1 Introduction

During the past century, increasing attention and efforts have been devoted to the development of alternative energy sources and energy storage devices due to the urgent need to replace rapidly consumed fossil fuels and alleviate the climate change problem. To make the renewable and volatile energy produced from sun and wind feasible in daily use, we need viable storage devices to carry and deliver the energy. One field of great potential is supercapacitors, which provide high power and good cyclability. The charge is stored in a supercapacitor in two ways, a non-faradaic double layer electrostatic charging process and a faradaic surface redox process. Popular materials explored in this field include high-surface-area carbon materials, transition metal oxides and conductive polymers.¹⁻⁴ During the charge/ discharge process, the rates of electron transfer and ion diffusion directly affect the supercapacitors performance.⁵ For certain energy materials, *e.g.* MnO₂, approaches to facilitate the charge transfer processes include synthesizing composite components for better electrical conductivity as well as modification of the active material's structure to produce shorter diffusion lengths.⁶⁻¹⁰ In our previous work, we have

successfully engineered and synthesized MnO₂/poly(3,4-ethylenedioxythiophene) (PEDOT) coaxial nanowires and MnO₂ nanoparticles enriched PEDOT nanowires, both of which effectively enhance the electrical conductivity by incorporating the conductive polymer PEDOT.¹¹¹ Some work has also been devoted to solving the ion diffusion issue by using different substrates like mesoporous carbon, carbon nanofiber, graphite nanoplatelets, nanoporous gold and conductive nanotubes for the synthesis of high surface area structures with shortened diffusion pathways for ions.¹⁴⁻¹⁹

Cellulose is an abundant and renewable raw material, suitable for industrial manufacturing. Cellulose and its derivatives have been applied to many aspects of our life for over 150 years and have been used for recent applications in fields like electronics, biomaterials, and pharmaceuticals where cellulose structure and properties have been found to be valuable.²⁰⁻²⁴ Cellulose is well-known as the main component of the plant cell wall, which permits the passage of nutrients like water, ions and small molecules, and maintains the cell shape with strong tensile strength. These attractive properties can also be applied to "energy cells". The native cellulose fibers applied here function like a cell wall that uptakes electrolyte from the bulk electrolyte bath. Electrolyte, like nutrients to the energy active materials, is then transported *via* the pores through the matrix of cellulose fiber to the active materials. In this way, the mesoporous channels inside the fibers act as an extra ion diffusion pathway for the charge/discharge processes. Previously, porous cellulose fibers have been applied as template for the synthesis of noble metal nanoparticles less than 10

nm²⁵ and different wood tissues have been utilized to grow zeolites, demonstrating the mesoporous structure of the cellulose fibers.²⁶

Here, we carried out a series of experiments using MnO₂ as the active material. We chose MnO₂, a very popular material for supercapacitors, because of its low cost, natural abundance, and environmental benignity. Both cellulose fibers (termed as “paper”) and polyester fibers (termed as “textile”) with and without electrolyte-blocking alumina coatings were used as the substrates for the deposition of MnO₂ to study the electrolyte absorption effect on supercapacitor performance. Carbon nanotubes (CNT) layer was applied on to those substrates before electrodeposition to provide electrical conductivity. Results show MnO₂ on cellulose fiber substrate has improved electrochemical performance compared to the ones on Al₂O₃ blocked fibers. This is attributed to the extra electrolyte uptake through the porous fibers. But textile fibers lack the capability to act as an electrolyte reservoir like in paper fibers, which will be shown. Further optimization of the supercapacitor electrode was realized by coating the electrode paper/CNTs/MnO₂ with another CNTs layer on top to enable the delivery of electrons to all the active materials.¹⁶ Therefore, in the electrode with configuration of paper/CNTs/MnO₂/CNTs (P-CMC), dual ion diffusion and electron transfer paths were enabled, resulting in high capacitance and good rate capacity. In this work, we have experimentally demonstrated the scientific significance of electrolyte absorption inside the cellulose fibers of paper for the application in supercapacitors substrates.

3.2 Experimental Section

3.2.1 Electrode Fabrication

Conductive paper preparation 170 mg native cellulose fiber disintegrated from Southern Yellow pine was added to 340 mL distilled water, and stirred with IKA RW20 digital mixer at 700 RPM for ~20 min. A uniform fiber suspension was obtained and poured into a Buchner funnel with fritted discs for vacuum filtration. A wet sheet was formed in ~3 min and dried in an oven at 100 °C for 5 minutes. The whole process is water based and additive free. Textile composed of polyester fibers was commercially available from Walmart. US. P3 SWNTs (As prepared single wall carbon nanotubes purified with nitric acid and left in highly functionalized form. This material contains 1.0-3.0 atomic% carboxylic acid which can be derivatized with a variety of functional groups.) were purchased from Carbon Solutions (California. US). 10mg CNTs were added to 10mL DI water with 1% sodium dodecylbenzenesulfonate (SDBS), followed by 5 minutes bath sonication, 3 min probe sonication and centrifugation purification. 1 mg/mL SWNT ink was prepared. The lab-made paper/textile sheet was dipped in the CNTs ink for 2~3 min and dried in an oven at 100 °C. This procedure was repeated three times to achieve a resistance around 30 ohms (measured by a four-point probe technique (EDTM)). The conductive paper/textile was then rinsed with DI water to remove the residual surfactant. For Al₂O₃ coated paper/textile substrates, the ALD Al₂O₃ coating was performed in a commercial TFS-500 Atomic Layer Deposition System from BENEQ with a base pressure of 2 mbar. Trimethyl aluminium [TMA, Al(CH₃)₃] and DI water were used as precursors at 150

°C. After 240 cycle's deposition, the thickness of the ALD Al₂O₃ is around 17 nm, estimated by measuring the thickness of ALD Al₂O₃ film deposited at the same condition on a silicon wafer using a Spectrophotometer from N&K Technology.

Electrochemical deposition of MnO₂ on CNTs-papers. First, the CNTs-paper was cut into square pieces. The electrochemical deposition of manganese oxide was performed by using a three electrodes set-up, where Ag/AgCl electrode was used as the reference electrode and platinum as the counter electrode. The working electrode was made of a piece of CNTs-paper, which was sandwiched by two small pieces of platinum at one end and connected to an alligator clip to avoid side reaction that may occur at the alligator. Then CNTs-paper was immersed in the aqueous electrolyte bath consisting of 20 mM manganese acetate and 100 mM sodium acetate. A constant potential of 0.65 V *versus* Ag/AgCl electrode was applied until the charge passed reached 600 mC. After the electrodeposition, the CNTs-paper was rinsed with distilled water twice and dried in air at room temperature.

3.2.3 Characterizations

The MnO₂-CNTs-paper structure was investigated using a field emission scanning electron microscope (Hitachi SU-70 SEM, operated at an acceleration voltage of 5 keV) and a transmission electron microscope (JEM 2100 FE-TEM). The microtomed sample was mounted in Spur epoxy resin and cut with a Reichert Ultracut E Ultratome microtome with a diamond knife (Leica, Vienna, Austria) at room temperature.

All the electrochemical studies were conducted in a standard three-electrode system using a bi-potentiostat (BI-STAT; Princeton Applied Research). A platinum counter electrode was used in conjunction with a Ag/AgCl reference electrode for all the measurements. In order to calculate the specific capacitance of the MnO₂-CNTs-paper, cyclic voltammetry at different scan rates (10mV/s-200mV/s) was performed by cycling the voltage between 0 and 0.8 V in 1 M Na₂SO₄ solution. The specific capacitance was calculated from cyclic voltammograms based on the equation:

$$C_{sp} = Q / \Delta E m$$

where the Q is the charge stored in the CV curve (charge stored by the double layer capacitance of the CNTs layer has been subtracted) and ΔE is 0.8 V and m is the mass of MnO₂, calculated from the charge passed in the electrochemical deposition. Specific capacitances were calculated by subtracting the double layer capacitance of CNTs layer estimated from the paper-CNT (P-C) or textile-CNT (T-C) electrodes. We want to point out here that the double layer capacitances of the CNTs in P-C/ T-C will not necessarily equal to the capacitance contribution of the CNTs in the composited electrodes. Double-layer capacitance is determined by the surface area, and the CNTs exposed surface area will become smaller after being covered by the MnO₂ layer. Here we use approximate value for the calculation. Electrochemical impedance spectroscopy was also conducted in a three electrode configuration, with a frequency range from 100 kHz to 100 mHz at open circuit potential.

3.3 Results and Discussion

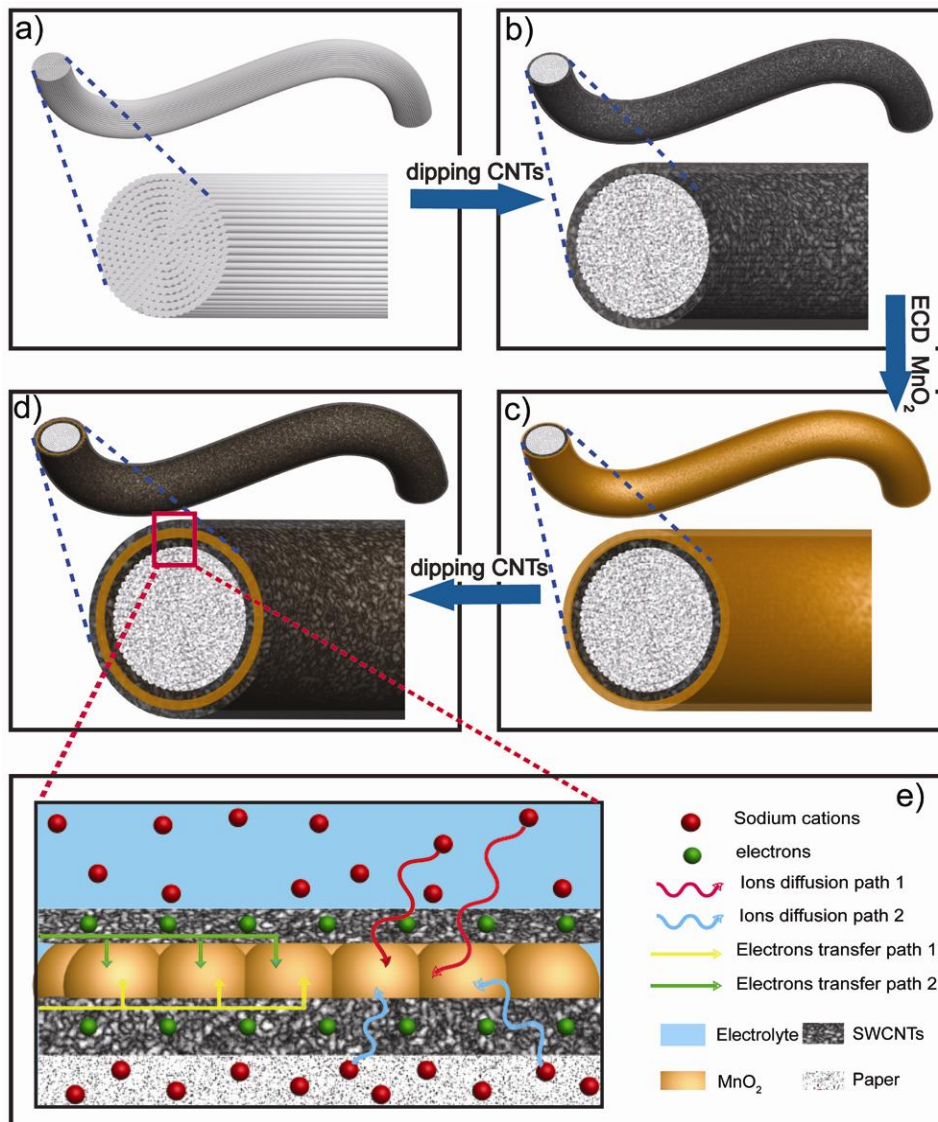
3.3.1 Structural Characterization

Hybrid electrode preparation. We prepared a group of MnO_2 samples on these fiber substrates, engineered with either one or two ion diffusion pathways to study the effect substrates have on ion diffusion (see Table 1). An electrode with an additional CNTs layer, paper/CNTs/ MnO_2 /CNTs (P-CMC), featuring dual diffusion paths for both ions and electrons was also prepared to demonstrate further optimized supercapacitive performance. Scheme 3.1 illustrates the preparation of electrode P-CMC. We started with a small piece of home-made paper prepared from Southern Yellow pine cellulose fibers using a vacuum filtration process. Conductive paper was prepared by dipping the paper into CNTs ink, followed by drying in an oven.^{33,34} We used an aqueous solution of manganese acetate and sodium acetate for the electrodeposition bath of MnO_2 . After applying a constant potential of 0.65 V (vs. Ag/AgCl), MnO_2 started to grow on the surface of the conductive paper and eventually formed a conformal thin layer (see Scheme 3.1b). The loading amount of the MnO_2 can be controlled by changing the charge passed during the electrochemical deposition. Another layer of CNTs was deposited on the top of MnO_2 afterwards as shown in Scheme 3.1d by applying the same method used in step one. In Scheme 3.1e, we show the cross-section of configuration P-CMC and indicate the dual ion diffusion pathways (indicated by the red and blue curved arrows) and electrons transfer pathways (indicated by the yellow and green straight arrows). For the ion diffusion process, besides the direct pathway 1 from bulk solution between each fiber to MnO_2 ,

ions can also diffuse through path 2 from the inside of each water-absorbing cellulose fiber to MnO₂. Further improved capacitive performance of MnO₂ can be realized by wrapping the materials with another layer of CNTs on top to serve as a second electron transfer path for the MnO₂. Additionally, the top layer of CNTs functions as a protective layer to alleviate the loss of MnO₂ caused by the material's detachment from the fiber's surface during cycling.

Table 3.1 Summary of the samples with different configurations.

Samples	Configuration	Ion path #	Electron path #
P-CM	Paper/CNTs/MnO ₂	2	1
P-ACM	Paper/Al ₂ O ₃ /CNTs/MnO ₂	1	1
T-CM	Textile/CNTs/MnO ₂	1	1
T-ACM	Textile/ Al ₂ O ₃ /CNTs/MnO ₂	1	1
P-CMC	Paper/CNTs/MnO ₂ /CNTs	2	2



Scheme 3.1 Schematic illustration of the synthesis process

(a) One single cellulose fiber was used to illustrate the process. (b) CNT-dipping coating. (c) Electrodeposition of MnO_2 . (d) Second CNTs-dipping coating. (e) Magnification of the square area highlighted in d to illustrate the dual electrons charge transfer and ions diffusion paths in the paper/CNTs/ MnO_2 /CNTs (P-CMC) configuration

Cellulose fibers structure. Natural cellulose fibers are made of multiple individual microfibrils, which are in turn comprised of microfibrils which result from aggregation of the cellulose glucan chains. These chains are stabilized by the hydrogen bonds and van der Waals forces between the hydroxyl groups on the D-glucose units, resulting in regions with both amorphous and crystalline character.^{27,28} Figure 3.1a shows the surface morphology of bare cellulose fiber. The network of microfibrils can be clearly identified. A cross-section of a single fiber (indicated by the half-circle area) is shown in Figure 3.1b. In the corresponding high magnification image (Figure 3.1c) of the red-squared area, the ends of the microfibrils that comprise the fiber and voids and pores between fibrils are visible. The mesoporous structure of each fiber can be seen from the SEM image in Figure 3.1d. Pores are formed as voids between neighboring rod-like cellulose microfibrils that are packed in parallel pattern mainly along the fiber axis. The pore size in the fiber is measured to be around 10-20 nm, as shown in the size distribution histogram in Figure 3.1d. It was reported that the cellulose fiber has a high specific surface area of 230 m²/g accessible for water sorption.²⁹ Due to the pores and voids inside each fiber and the hydrophilic groups (hydroxyl group) along the cellulose chains, cellulose fibers can absorb water very well. When fully wetted, cellulose can take up to 140 w.t. % water inside the fibers as measured by pulsed gradient spin-echo method.³⁰ When swollen in the aqueous electrolyte, all of the pores in the fibers are open compared to the dry state, in which pore closure happens due to hydrogen bonding between adjacent microfibrils.^{31,32} This pore characteristic is ideal for providing channels for electrolyte uptake. Meanwhile, the electron-rich oxygen atoms of the polar hydroxyl

and ether groups in cellulose can also interact with electropositive transition metal cations,²⁵ like sodium ions, therefore favoring the absorption of the electrolyte ions. With all these properties, cellulose fiber can provide good diffusion channels for electrolyte solution, enhancing ion transportation to the active material. As a result, better electrochemical performance is to be expected. For comparison, we prepared cellulose fiber with blocked ion diffusion paths by coating a thin layer of alumina on the surface of the fiber using atomic layer deposition method. To highlight the advantage of cellulose fibers over other flexible substrates for electrolyte absorption, we also test polyester fibers with and without Al₂O₃ coating as substrates. SEM images of ALD-coated cellulose fiber and bare polyester fiber at the same magnification as Figure 3.1d are shown in Figure 3.1e, f, respectively. After ALD treatment, all of the pores at the surface of cellulose fiber are successfully blocked by the Al₂O₃ layer (compare Figure 3.1 d to e). SEM image in Figure 3.1f (compare to Figure 3.1d) reveals the nonporous and relatively smooth surface morphology of polyester fiber. The small cracks observed in the image are due to the exposure of the electron beam.

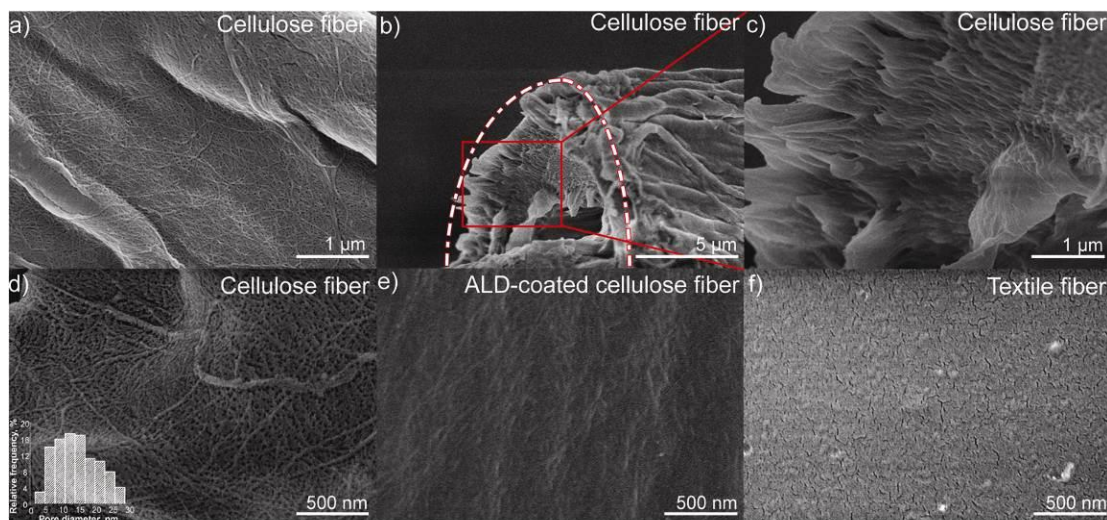


Figure 3.1 SEM characterizations on the different fibers.

SEM images of the (a) surface and (b) cross-section of a cellulose fiber. (c) SEM image of the framed area in (b). (d-f) SEM images at 50K magnification of the surfaces of a cellulose fiber, ALD- Al_2O_3 coated cellulose fiber, and a polyester fiber, respectively. All of the fibers were sputtered with 2~5 nm gold to prevent localized charging and distortion. Inset of (d) shows the size distribution histogram of the pores in cellulose fiber surface build by counting pores in the SEM image.

Electron microscopy was used to characterize fiber structure and the morphologies of deposited MnO_2 and CNTs layers. Figure 3.2a shows the CNTs-paper before (left) and after (right) MnO_2 deposition. The area below the red dashed line in the right paper was immersed into the electrodeposition bath for MnO_2 growth. The SEM image of the CNTs-paper (Figure 3.2b) shows clearly the CNTs network layer covering and bridging between each fibril. This macroporous CNTs layer will not influence the diffusion of electrolyte from the paper fibers underneath to the

MnO₂ deposited on top. The CNTs wrapped paper fibers were coated by a conformal MnO₂ layer (500~1000 nm in thickness) by electrodeposition, forming the P-CM electrode. The corresponding high magnification SEM image (Figure 3.2c) shows that the MnO₂ layer was comprised of petal-shape nanoclusters in close arrangement, and each nanocluster was composed of nanosheets of a few nanometers in thickness.³⁵ This kind of architecture maximizes the surface area and facilitates the ion diffusion process. The electrodeposited MnO₂ has been characterized by Raman spectroscopy as well, showing three major features at 503, 576, and 655 cm⁻¹ that correspond to the Birnessite phase (see Figure 3.3).³⁶ The P-CMC electrode was produced by the addition of another CNTs layer on top of the MnO₂. In the high magnification SEM image Figure 3.2d, we can clearly see the CNTs on the top as indicated by the red arrows (SEM images at higher magnification are provided in Figure 3.4). A cross-sectional view of the P-CMC sample prepared by microtome was also characterized by both SEM (Figure 3.2e) and TEM (Figure 3.2f). The red arrow in Figure 3.2e indicates the electrodeposited MnO₂ layer with a width around 1 μm at selected region. EDS mapping results of O and Mn further verify the location of the MnO₂ layer. The CNTs layers on both side of the MnO₂ are hard to observe due to the low contrast signals. However, due to the mechanical stress during the microtome sample preparation process, the MnO₂ layer detached from the fiber surface. In the void between the fiber surface and the MnO₂ layer we can identify some individual CNTs and CNTs bundles as indicated by the white arrow in Figure 3.2e. The same geometry was obtained by the TEM image in Figure 3.2f. A TEM image of MnO₂ at higher resolution is provided at bottom left. Some pairs of parallel lines patterns can be

identified in the image, presenting the cross-section of the nanosheets that compose the MnO_2 layer with a width around 3 nm for each nanosheet (see Figure 3.5).

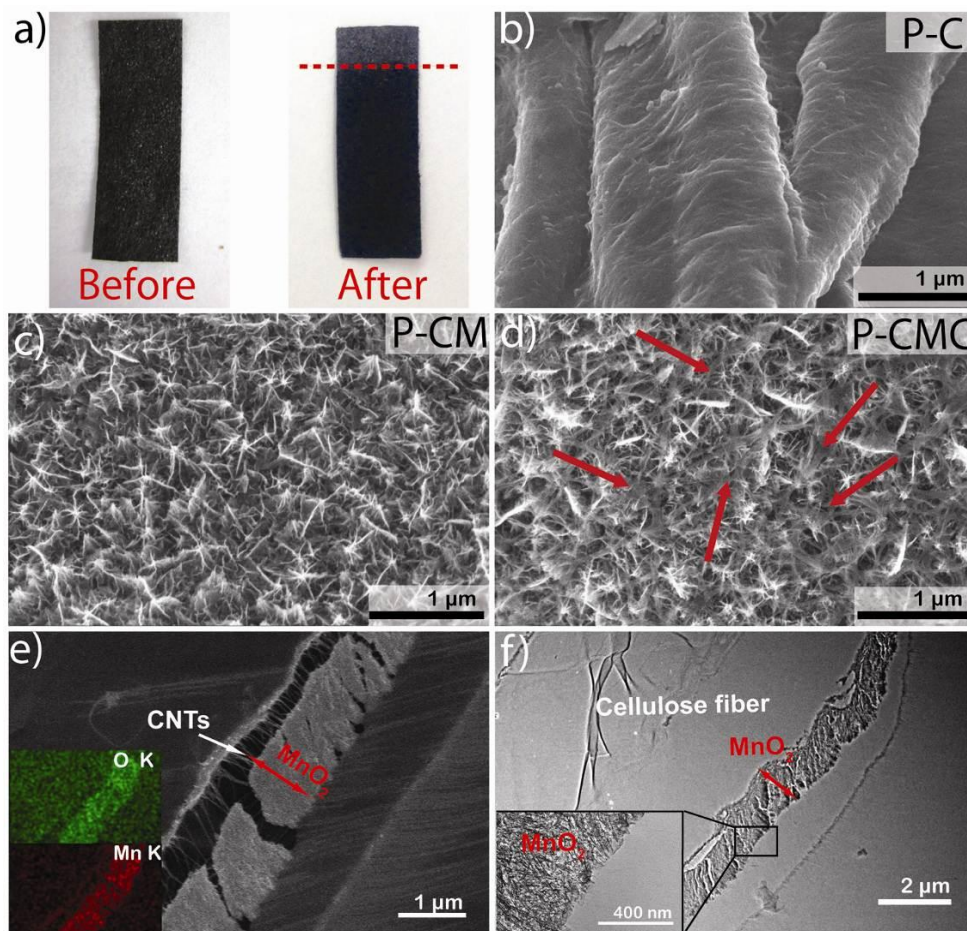


Figure 3.2 SEM and TEM images on different CNT-paper based electrodes.

(a) Digital images of CNT-paper before (left) and after MnO_2 deposition (right). (b-c) SEM images of CNTs-paper (P-C), Paper/CNTs/ MnO_2 (P-CM), and paper/CNTs/ MnO_2 /CNTs (P-CMC), respectively. Red arrows in (d) indicate the location of CNTs. (e) SEM and (f) TEM images of cross-section of P-CMC prepared by microtome. Inset of (e) shows the corresponding EDS mapping of O (green) and Mn (red). Inset of (f) represents the TEM image of the framed area at higher magnification.

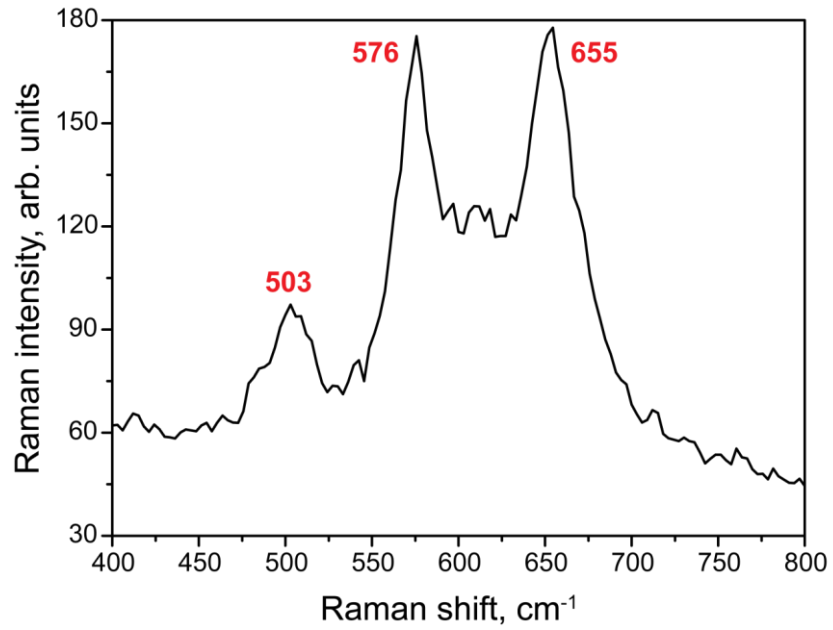


Figure 3.3 Raman spectra of MnO₂ electrodeposited on cellulose paper

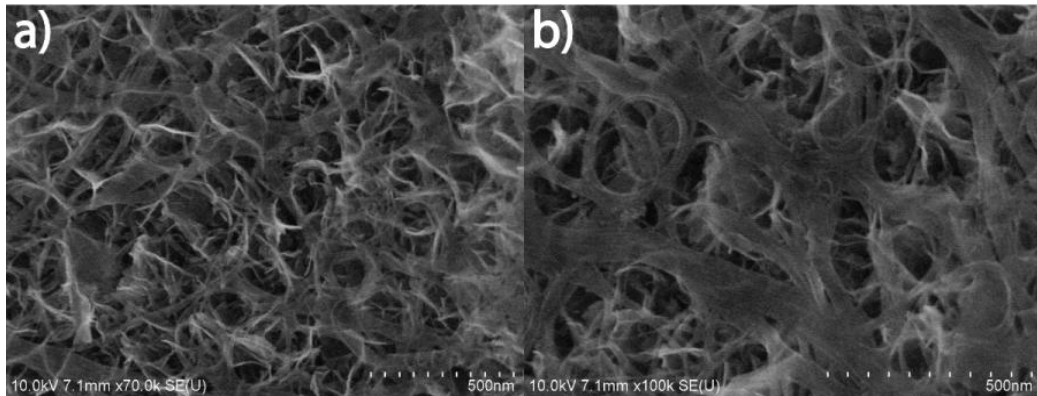


Figure 3.4 SEM images of P-CMC at higher magnifications

(a) 70k and (b) 100k. CNTs on top of the MnO₂ layers can be clearly identified in these images.

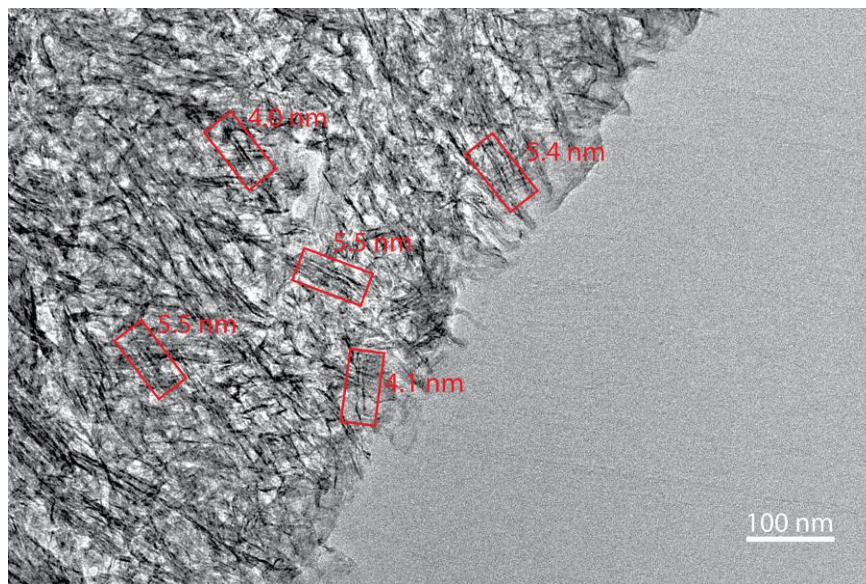


Figure 3.5 HRTEM on the MnO₂ nanosheets structure.

TEM image of the MnO₂ layer in the microtomed cross-section of sample P-CMC. Square areas in red show pairs of parallel lines presenting the cross-sectional view of MnO₂ nanosheets. Distances between parallel lines are roughly estimated as the thickness of the nanosheet.

3.3.2 Electrochemical Characterizations

Electrochemical characterization. To clearly verify the advantage of the additional ion diffusion pathway realized by the cellulose fibers, we compared the electrochemical performances of two samples in the configurations of paper/CNTs/MnO₂ (P-CM) and paper/Al₂O₃/CNTs/MnO₂ (P-ACM) (a schematic illustration can be found in Figure 3.6a). Paper fibers without Al₂O₃ coating have both ion diffusion paths as indicated in Scheme 3.1e. However, for the paper fibers with Al₂O₃ coating (~ 17nm), the pores on the surface of each cellulose fiber will be

mostly blocked by the nonporous Al_2O_3 layer, preventing the fiber from absorbing electrolyte. Therefore electrolyte can only access to the space between each fiber, but not inside the fiber. As a result, ions can only diffuse from the bulk electrolyte to MnO_2 . Successfully coating of Al_2O_3 layer was confirmed by the EDS mapping images of paper fibers coated with Al_2O_3 and CNTs layers (see Figure 3.7). Additionally, we prepared samples in the same way, starting from textile substrate composed of nonporous polyester fibers and wrapped with conductive CNTs (see Figure 3.6b). Therefore, the textile-based electrodes with or without Al_2O_3 layer will both have only one ion diffusion path. This pair of textile-based samples demonstrates that the Al_2O_3 layer has no effect on electrochemical performance. The corresponding SEM images of a single fiber for P-ACM and T-ACM (textile/ Al_2O_3 /CNTs/ MnO_2) electrodes are shown in Figure 3.8a, d respectively. CNTs used in the electrode preparation for conductivity will also contribute to the double-layer capacitance out of the total capacitance. Therefore electrochemical tests were also carried out on CNTs-wrapped paper/ textile samples without active MnO_2 (P-C, T-C) and the results are shown in Figure 3.8. The cyclic voltammetry (CV) curves for the two textile-based MnO_2 samples at 20 mV/s are shown in Figure 3.8e, and demonstrate no difference. This means that the Al_2O_3 layer itself has no contribution to the capacitance, and will not store any charge. For the paper-based samples, the CV curve of electrode P-CM shows a much more square shape than the P-ACM electrode (see Figure 3.8b.), which can be attributed to the extra ion diffusion pathway in P-CM. In both paper and textile substrates, the capacitance contributions of the CNTs layer are small (compare the green curve to the others in Figure 3.8e,

b). The rate performances for the two samples of paper-based and of textile-based MnO_2 are shown in Figure 3.8c, f respectively. Specific capacitances were calculated by subtracting the double layer capacitance of the CNTs layer estimated from the P-C/T-C electrodes. As the scan rate increases from 10 mV/s to 200 mV/s for the paper-based MnO_2 samples, the capacitance of electrode P-CM was maintained better than P-ACM. This is because the higher scan rates require faster ion diffusion speed, to access all of the active material and so, sample P-CM with better ion diffusion access can better utilize the MnO_2 and maintain specific capacitance at higher scan rates or current density than P-ACM. For comparison, the two textile-based samples show nearly identical capacitances even at higher scan rates. These results confirm that the ion diffusion process can be effectively boosted by using an electrolyte-absorbing cellulose paper substrate.

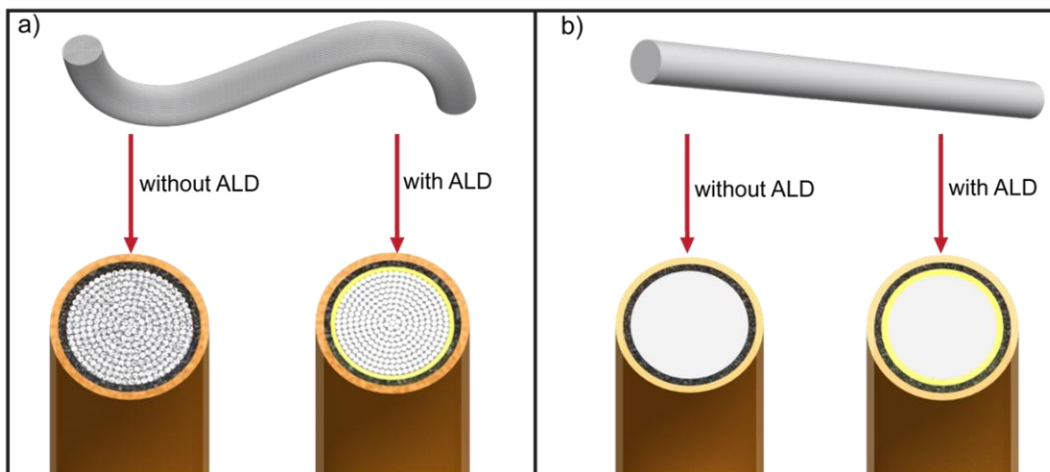


Figure 3.6 Schematic illustration of the fabrication process.

(a) Cellulose fibers and (b) polyester fibers. For both fibers (white color), electrodeposition of MnO_2 (brown color) was prepared on CNTs (black color) coated fibers with and without Al_2O_3 coating (yellow color) by ALD process.

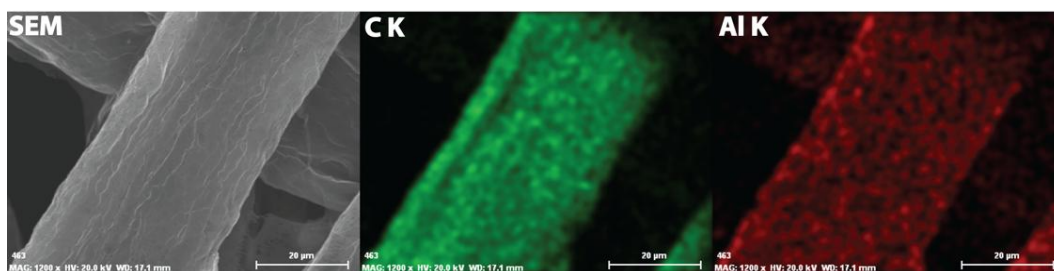


Figure 3.7 SEM-EDS characterization on ALD alumina coated fiber

SEM image and EDS mapping of C (green color) and Al (red color) on a segment of cellulose fibers coated with Al_2O_3 and CNTs layers (paper/ Al_2O_3 /CNTs).

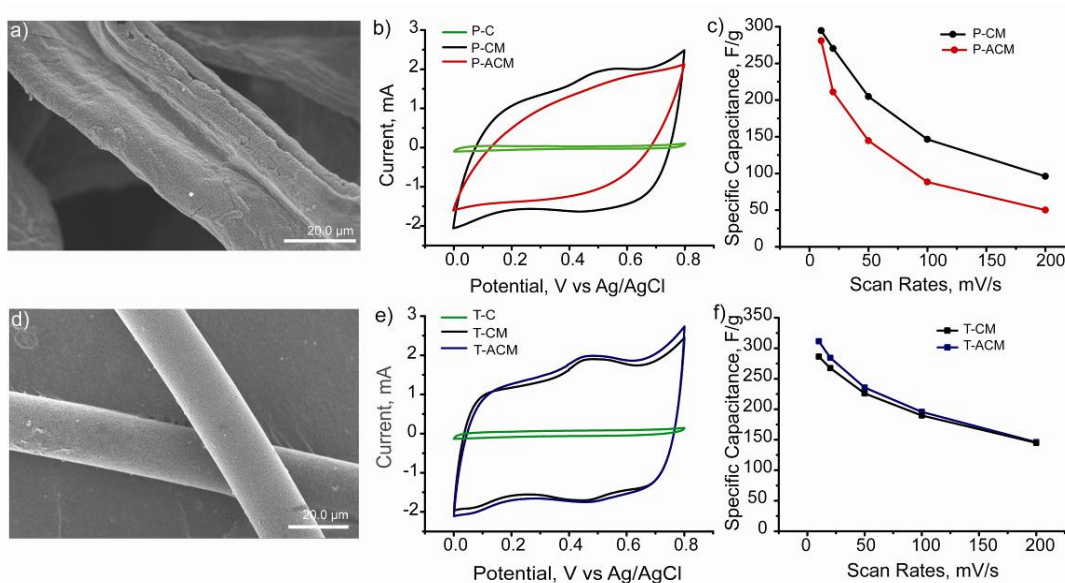


Figure 3.8 Electrochemical performance of MnO_2 on different substrates.

SEM images of Al_2O_3 coated (a) paper fibers and (d) textile fibers after MnO_2 deposition forming P-ACM and T-ACM respectively. (b) Cyclic voltammetry curves of P-C (green), P-CM (black) and P-ACM (red) at 20mv/s. (c) Specific capacitances of P-CM and P-ACM at different scan rates. (e) Cyclic voltammetry curves of T-C (green), T-CM (black) and T-ACM (blue) at 20mv/s. (f) Specific capacitances of T-CM and T-ACM at different scan rates. The electrolyte in all experiments was 1M Na_2SO_4 .

While performance can be improved by the double ion diffusion paths realized by the cellulose paper substrate, further optimization of the hybrid electrode can be achieved by doubling the electron paths as well. By simply wrapping the P-CM electrode with one extra layer of CNTs coating on the top, we produced electrodes in the configuration of paper/CNTs/MnO₂/CNTs (P-CMC). Both P-CMC and P-CM have two ion diffusion paths, but different electron transfer paths numbers. As illustrated in the Scheme 3.1e, the P-CMC sample with two CNTs layers provides two electron transfer paths for the active materials while sample P-CM has only one electron transfer path. The cyclic voltammetry (CV) curves at 50mV/s in Figure 3.9a show that sample P-CMC had a more square shape CV curve than the electrode P-CM, which indicates better capacitive performance, as is expected from a supercapacitor with higher conductivity. Specific capacitances at different scan rates from 10mV/s to 200mV/s for the two samples are shown in Figure 3.9b. MnO₂ has poor conductivity of 10⁻⁵-10⁻⁶ S cm⁻¹, so electron transfer will limit the capacitance especially at high scan rates. Therefore, the P-CM sample demonstrates significantly worse rate performance, with specific capacitance value dropping from 295 F/g at 10 mV/s to only 96 F/g at 200 mV/s (32.5% maintained). The P-CMC sample shows much better rate performance as well as a higher initial specific capacitance. The dual electron pathways in the P-CMC sample result in specific capacitance of 327 F/g at scan rate of 10 mV/s and 201 F/g at 200mV/s (61.5% maintained). The amount of CNTs coated on the paper can be controlled by changing the dip and dry procedure repeating times. In this work we dipped only one time for the second CNTs layer, but

it is possible that even better rate performances could be achieved by optimizing the dipping times of the CNTs layers

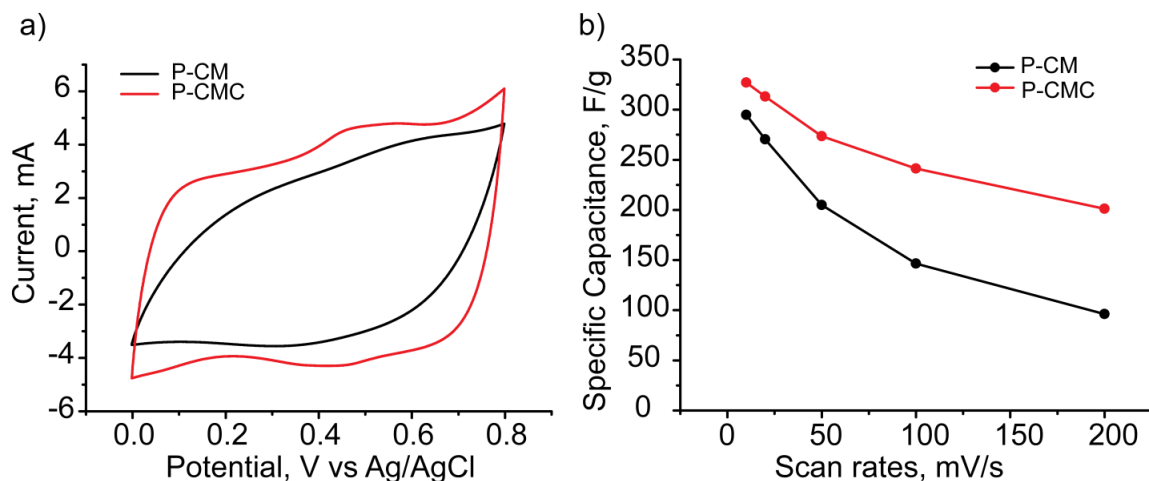


Figure 3.9 Electrochemical performance

(a) Cyclic voltammetry curves of P-CM (black) and P-CMC (red) at 50mV/s in 1M Na₂SO₄ electrolyte. (b) Specific capacitances of P-CM (black) and P-CMC (red) at different scan rates in 1M Na₂SO₄ electrolyte.

3.3.3 Electrochemical Impedance Spectroscopy

Electrochemical impedance spectra. To further study the charge transfer resistance in the paper based MnO₂, electrochemical impedance spectroscopy results from three different samples were collected and compared as shown in Figure 3.10 a. The P-CMC sample was compared to the sample P-CM without the second electrical pathway as well as the sample P-ACM with only one electrical and one ionic diffusion pathway, to demonstrate the effect of each aspect of this design on charge transfer resistance (see Table 3.1 for sample configurations). At high frequency, the

intercept of the real axis represents the equivalent internal resistance (R_s), which includes the electrolyte resistance, intrinsic resistance of the active materials and contact resistance at the interface between the current collector and the active materials. The R_s for the sample P-ACM was 21.4 ohm. This value was higher than the 15.7 ohm of sample P-AC because of the non-conductive Al_2O_3 layer deposited onto the fiber surface. For sample P-CMC, an even lower R_s value of 10.7 ohm was obtained, which can be attributed to the extra conductive CNTs layer. At the medium-high frequency range, all three curves show well-defined semi-circles. The diameter of the semi-circles corresponds to the charge transfer resistance (R_{ct}) at the interface where faradaic reaction takes place, involving both ion and electron transfer processes. The R_{ct} value was lowest for the sample P-CMC (0.7 ohm) with dual charge transfer paths for both electrons and ions, and highest for sample P-ACM (8.2 ohm) with only one path for electron transfer and ion diffusion. From our simple model (as illustrated in Scheme 3.1e), the charge transfer resistance of P-CM with both sides of MnO_2 layer accessible for ions insertion/desertion should be around 50% of the value of P-ACM which has only one side been used for ions diffusion due to the Al_2O_3 blocking. The charge transfer resistance measured from EIS is 3.2 ohm for sample P-CM, which is approximately half of the value for samples P-ACM blocked by Al_2O_3 . The deviation from exactly 50% may be due to the sample preparation variation and the limited transport of electrons. At high frequency, both P-CMC and P-CM electrode show near 90° linear region, which indicates the ideal capacitor behavior, while for P-ACM, EIS curve deviates much more with an angle from vertical line.^{37,38} This result further confirms that more electron transfer and ion diffusion paths are provided

within the configuration of P-CMC, and the internal resistance and charge transfer resistance are effectively reduced.

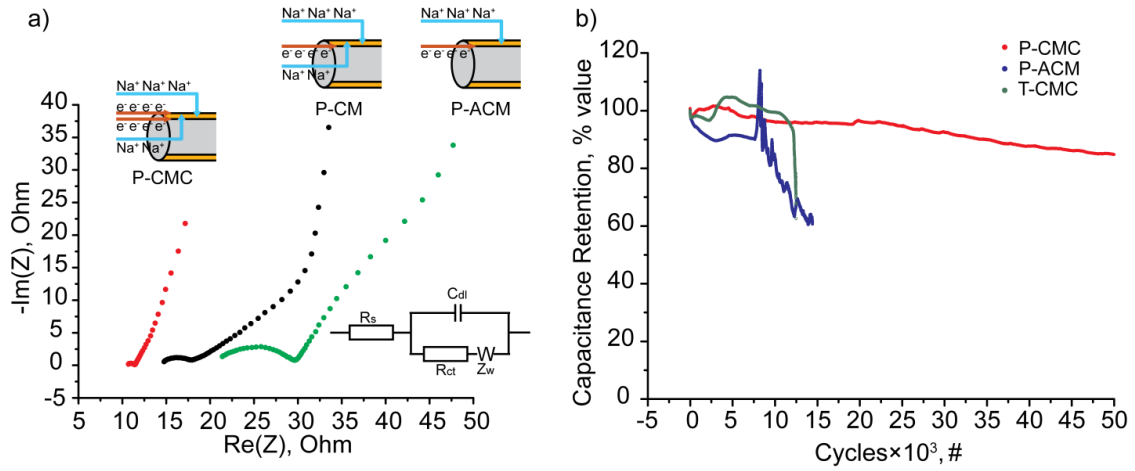


Figure 3.10 Impedance spectra and cycling test

(a) Nyquist electrochemical impedance spectra of three samples: P-CMC (red), P-CM (black), P-ACM (green) measured in 1M Na₂SO₄ under open circuit voltage conditions. Ion diffusion paths were presented by the blue arrows and electrons transfer paths were indicated by the red arrows in the cartoons. Inset of (a) shows the equivalent circuit. (b) Cycling performance of P-CMC (red), P-ACM (blue), and T-CMC (green) at 3 mA/cm² in 1M Na₂SO₄ electrolyte for up to 50K cycles.

3.3.4 Cycling Performance

Cycling performance of P-CMC. Figure 3.10 b shows the cycling performance of three electrodes evaluated by galvanostatic charge/discharge at current density of 3 mA/cm² for up to 40000 cycles. For the first few hundred cycles, the specific

capacitance of all three electrodes dropped by around 4%. For both P-CMC, T-CMC electrodes, the curves show increasing capacitance retention up to 3000th, 5000th cycles, respectively. This phenomenon can be attributed to the complete electrolyte wetting effect of the cellulose and polyester fibers over time. As paper/textile became saturated by the electrolyte, faster ion diffusion process was enabled. Polyester textile can only be wetted between fibers, while cellulose paper can also absorb water inside each fiber. Therefore the saturated point appeared earlier for the P-CMC (at 3000th cycle) than the T-CMC (at 5000th cycle). The capacitances for both electrodes started to decrease after the saturated points, a change which is likely due to the dissolution of MnO₂ into the electrolyte after long-time cycling.⁹ T-CMC showed fast capacitance decay from 10000th cycle, and maintained only 62% capacitance at 12500th cycle. While for P-CMC, much better capacitance retention was reached with 96%, 93%, 88% and 85% capacitance retentions at 20000th, 30000th, 40000th and 50000th cycles, respectively. This longer cycling life of MnO₂ deposited on cellulose fibers than on polyester fibers is likely due to the fibers' different surface roughness. For polyester fiber with a relative smooth surface, the MnO₂ layer peeled off easier. While for cellulose fiber with a more rough surface geometry, the MnO₂ stuck to the substrate better and survived a longer cycling test. For the P-ACM electrode, the wetting of electrolyte was prevented by the blocking ALD layer at first. When it came to around 8000th cycle, the capacitance increased suddenly which can be explained by the breaking of the Al₂O₃ layer after thousands of cycles, and following electrolyte wetting of the fibers that were exposed to the bulk solution. Due to the breaking of the ALD layer, it started to peel off from the fibers together with the MnO₂ deposited

above. Therefore we see quick decay of the capacitance of P-ACM afterwards. The cycling performance of P-CMC achieved in this work shows much better capacitance retention than many of the previous reported MnO₂ retention capabilities, improving on reported performances of 75-90% for up to 2000 cycles.^{39,40} The P-CMC electrode also survived a much longer cycling life at similar capacitance decay rate compare to the MnO₂ deposited on conductive polyester textile fibers reported by Bao *et al.*, which showed good capacitance retention around 95% over 3000 cycles at a current density of 1 mA/cm².¹⁶

3.4 Conclusion

In summary, we use cellulose fibers with a porous internal structure as the substrate for the deposition of electrochemical energy storage materials to facilitate the ion diffusion process. Different substrates, either with or without open pores, were studied for comparison, and results show that cellulose fibers with open pore channels extending along the fiber gave better electrochemical performance, which can be attributed to the extra ion diffusion pathway realized through the electrolyte uptake by the cellulose fibers. Further improved electrochemical performance can be achieved by applying an additional conductive wrapping of CNTs on the surface of P-CM, resulting in configuration of P-CMC. In this P-CMC electrode, dual ion and electron paths are realized and provide even better capacitive performance. The cellulose paper based substrate also show excellent cycling performance, retaining 85% of its capacitance up to 50k cycles. This work was able to demonstrate the specific advantages of improved ion pathways that can be provided by mesoporous cellulose

fibers substrate and its substantial potential for other energy materials as well in energy devices design.

Chapter 4: RuO₂-MnO₂ Composite Nanowires for Supercapacitors with High Energy and Power Densities

4.1 Introduction

Among all the transition metal oxides, MnO₂ is a very widespread choice for supercapacitor materials due to its abundance, low cost, and environmental friendliness. However, its performance is ultimately limited by its intrinsically poor electrical conductivity of 10⁻⁵-10⁻⁶ S cm⁻¹.⁵⁷ Lots of effort has been devoted to overcoming this drawback.^{47,45,48,85} First, nanoscopic structures with high surface areas have been widely explored for MnO₂ along with enhancing its connection to the current collector in order to facilitate the electron transfer process. Well-ordered 1D nanoarrays and 3D porous structures of MnO₂, synthesized by using templates (AAO) or nanostructured current collectors (metal arrays, 3D porous metal), have been reported to show superior electrochemical and mechanical properties over its bulk counterparts.¹³²⁻¹³⁵ For the second approach, varieties of conductive materials have been explored as composite materials to improve the MnO₂'s electrical conductivity, including carbon materials and conductive polymers. The most commonly applied experimental method is physically mixing the conductive additives with MnO₂. A more effective way is to integrate the MnO₂ with conductive components with precise control, resulting in sophisticated architectures, e.g. MnO₂/CNT coaxial nanotubes,¹⁰⁰ and MnO₂ wrapped with graphene.¹¹⁸ In this approach, conductive supplementary materials are added either before MnO₂ growth or through additional layer, coating, or wrapping methods after MnO₂ synthesis.^{136,137,117,88} Recently, modifications of the

MnO₂ with other metal oxides have also been studied.^{138–142} Different metal oxides including Ni,^{140,138} Fe,¹⁴³ Co,¹⁴⁰ V,^{142,144} Mo,¹⁴¹ Ru,¹⁴⁵ Cu¹⁴⁶ oxides have been reported. Some of these mixed oxides show improved conductivity while others show better stability.

RuO₂ xH₂O which has mixed ionic and electrical conductivity is known to give a high specific capacitance as well as high power performance.³⁵ However, due to its high cost and the environmental friendliness associated with the acidic electrolyte (H₂SO₄) that it uses, the application of solely RuO₂ itself for energy storage devices is limited in real applications. Nevertheless, RuO₂ is considered a good component to couple with MnO₂ to target better electrical conductivity.

Tarascon et al.¹⁴⁷ just reported a study on Li₂Ru_{1-y}Mn_yO₃ as a lithium battery material that demonstrated improved conductivity and stability. For applications in supercapacitors, electrospinning has been utilized to produce MnO₂-RuO₂ nanofiber mats, resulting in a capacitance of 208 F/g.¹⁴⁵ Oxidative co-precipitation of MnO₂ and RuO₂ is also reported to give a high specific capacitance of 273 F/g with 9 w.t.% RuO₂; however, the acetylene black (20 w.t.%) added in the electrode preparation also contributes partially to this high value.¹⁴⁸

Here we present the synthesis of MnO₂-RuO₂ nanowires arrays without any other additives by a simple one-step electrochemical co-deposition, resulting in uniform and homogeneous hybrid nanoarrays. Electrodeposition merits the ease of implementation of a template for nanostructuring as well as component control by adjustments on the deposition parameters and bath concentrations. In the pre-annealed nanowires, RuO₂ nanoparticles are homogeneous distributed in the MnO₂

matrix. The prepared nanowires were annealed at 200 °C before the removal of the AAO template. The higher conductivity in the composite material is supported by electrochemical impedance spectroscopy (EIS) characterization results. A high specific capacitance of 302 F/g was obtained with only 6.70 w.t. % RuO₂. Further study on the RuO₂ loading amount effect was conducted by comparing the electrochemical performance of composites samples with different RuO₂ weight percentages. Samples with higher amounts of RuO₂ show higher capacitances. By deconvoluting the capacitance of these different samples, we found that the improvement in the composites sample is mainly attributed to the increase of the surface stored charge, which is facilitated by the enhanced electrical conductivity in the co-deposited materials, while there is less influence of the RuO₂ loading amount found on the insertion capacitance. This work induces a simple promising approach to improve poor conductive MnO₂ materials for supercapacitor application, and can be applied to synthesize many other ceramic hybrid structures for synergistic properties.

4.2 Experimental Section

4.2.1 Nanowires Synthesis

Electrodeposition: First a layer of gold is sputtered onto the branched side of an AAO template by a Denton Vacuum Desktop III sputter machine. Copper tape (3M) is then attached to the sputtered side of the AAO for connection to the electrical circuit. Defining and sealing the electroactive window (0.32 cm²) is performed using silicone rubber. The prepared AAO is used as the working electrode with Ag/AgCl as

the reference electrode and platinum as the counter electrode during the electrodeposition process. RuO₂-MnO₂ composite nanowires are synthesized potentiostatically at 0.75V in an aqueous solution of RuCl₃ (1-20 mM), MnAc₂ (20-100 mM) and NaAc (100 mM) until the charge reached 200 mC. Electrodeposition solutions were used with Ru/Mn ion ratios of 1/100, 1/20, 1/2 having the total compositions of: 1 mM RuCl₃-100 mM MnAc₂, 1 mM RuCl₃-20 mM MnAc₂, and 10 mM RuCl₃-20 mM MnAc₂, respectively (all contain 100 mM NaAc). The electrodeposited nanowires in the AAO template were then annealed in air at 200°C for 1 hr. The AAO template is subsequently dissolved in 3 M NaOH solution and rinsing with distilled water to obtain the nanowires arrays for characterization.

4.2.2 Characterizations

Elemental analysis by the inductively coupled plasma atomic emission spectroscopy (ICP-AES) is performed by a PerkinElmer ICP-Optima 4700 to measure the masses of RuO₂ and MnO₂, which can be used to calculate the RuO₂ weight percentages and specific capacitances. Calibration curves were made from Ru, Mn standards traceable to the National Institute of Standards and Technology (NIST). Samples were dissolved in freshly made aqua regia solution (prepared by mixing 3:1 concentrated HCl: HNO₃) and diluted to a known volume before being administered to the plasma. Intensities of Mn at 257.610 nm and Ru at 240.272 nm were collected to obtain quantitative information of the two elements. Samples were prepared in solutions with composition of: 1 mM RuCl₃-20 mM MnAc₂, 5 mM RuCl₃-20 mM MnAc₂, 10 mM RuCl₃-20 mM MnAc₂.

Imaging of MnO₂ nanowires was acquired using a field emission scanning electron microscope (Hitachi SU-70 FEG-SEM, operated at 5 eV) and transmission electron microscope ((JEOL JEM 2100 FE-TEM), 200 keV).

Raman spectra were collected on Horiba JobinYvonLabRAM Raman microscope (model ARAMIS) with excitation lines that included 532 nm and 633 nm. In these experiments, green laser line (532 nm) excitation was utilized for the nanowires.

XPS analysis was done on Kratos AXIS 165 spectrometer. Adventitious hydrocarbon C1s signal at 284.6 eV was used as the energy reference to correct for charging.

The electrochemical studies of the MnO₂ nanowire arrays were performed in a standard three-electrode system utilizing a bipotentiostat (BI-STAT, Princeton Applied Research). Ag/AgCl was used as the reference electrode and Pt was used as the counter electrode. Cyclic voltammetry and galvanostatic charge/discharge were performed in 1 M NaSO₄ with potential window from 0-1 V vs. Ag/AgCl. The specific capacitance was calculated from cyclic voltammograms based on the equation:

$$C_{sp} = \frac{Q}{\Delta E m}$$

Where the Q is the charge stored in the CV curve and ΔE is 1.0 V and m is the mass of electrode materials determined by the elemental analysis of ICP-AES. Electrochemical impedance spectroscopy was conducted in a three electrode

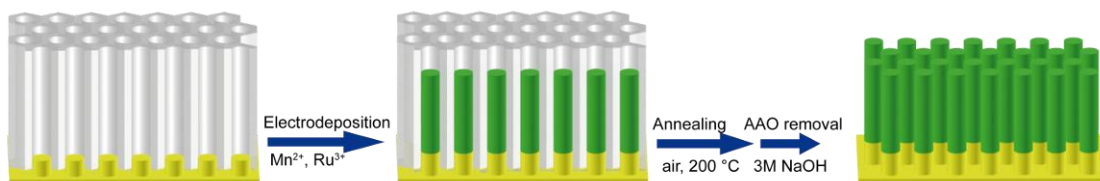
configuration, with a frequency range from 100 kHz to 100 mHz at open circuit potential.

4.3 Results and Discussion

4.3.1 Structural Characterization

Schematic 4.1 shows the preparation process for the RuO₂-MnO₂ composite material nanowire arrays. Anodic alumina oxide (AAO) with gold sputtered on one side is used as a template here. An electrolyte bath consisting of both manganese (II) ions and ruthenium (III) ions is used for the deposition. After applying a constant potential of 0.75V vs. Ag/AgCl, MnO₂ and RuO₂ start to co-deposit inside the AAO template and grow into nanowires. After electrodeposition, the nanowires are annealed at 200°C in air for 1 hour followed by the removal of the AAO template. The purpose of the annealing treatment is to convert the RuO₂ into a more conductive phase. The electrical conductivity of amorphous RuO₂ is on the order of 1 S/cm; 10³ S/cm in its polycrystalline form; and up to 10⁴ S/cm as a single crystal.¹⁴⁹ The mild temperature of 200°C chosen here can effectively improve the electrical conductivity without sacrificing good ionic conductivity, which is known to drop dramatically when all the water in hydrated-RuO₂ is removed.^{150,33,151,39} It has been reported that hydrated-RuO₂ with around 0.5 H₂O will give the best performance as a supercapacitor with both electronic and ionic conductivity well balanced.³³ In this work, RuO₂ co-deposited in the MnO₂ nanowires matrix can facilitate fast charge

transfer during the charge/discharge process while improving the capacitive performance of the MnO₂ nanowires.



Scheme 4.1. Schematic illustration of the electrochemical co-deposition process.

The structure of the nanowire arrays were characterized by SEM and TEM images. Figure 4.1a shows the SEM image of an RuO₂-MnO₂ composite nanowire array grown on a flat-top gold electrode after the removal of AAO template. The nanowires are shown aggregating due to the surface tension during the evaporation of the water. A TEM image of a nanowire, 200 nm in diameter, which corresponds to the pore size of the AAO template, is shown in Figure 4.1b. In the corresponding high resolution TEM (HRTEM) image (Figure 4.1c), crystals with sizes around 5 nm are found. The formation of these crystals is likely due to the electron beam annealing effect. Average d-spacing of 0.21 nm and 0.25 nm are observed from the lattice resolved TEM images (see Figure 4.2). These fringe values correspond well to the spacing between the 200 plane and 112 plane of Birnessite MnO₂ (JCPDS No. 43-1456). EDS mapping on a segment of a single nanowire (as indicated by the square area in Figure 4.1d) was performed to confirm and locate the RuO₂ in the MnO₂ nanowires. Almost identical mapping images of Ru and Mn signals demonstrate the homogeneous co-growth of RuO₂ throughout the MnO₂ nanowires. This kind of architecture with

conductive RuO₂ incorporated facilitates fast delivery of electrons into the MnO₂ matrix for better capacitive performance.

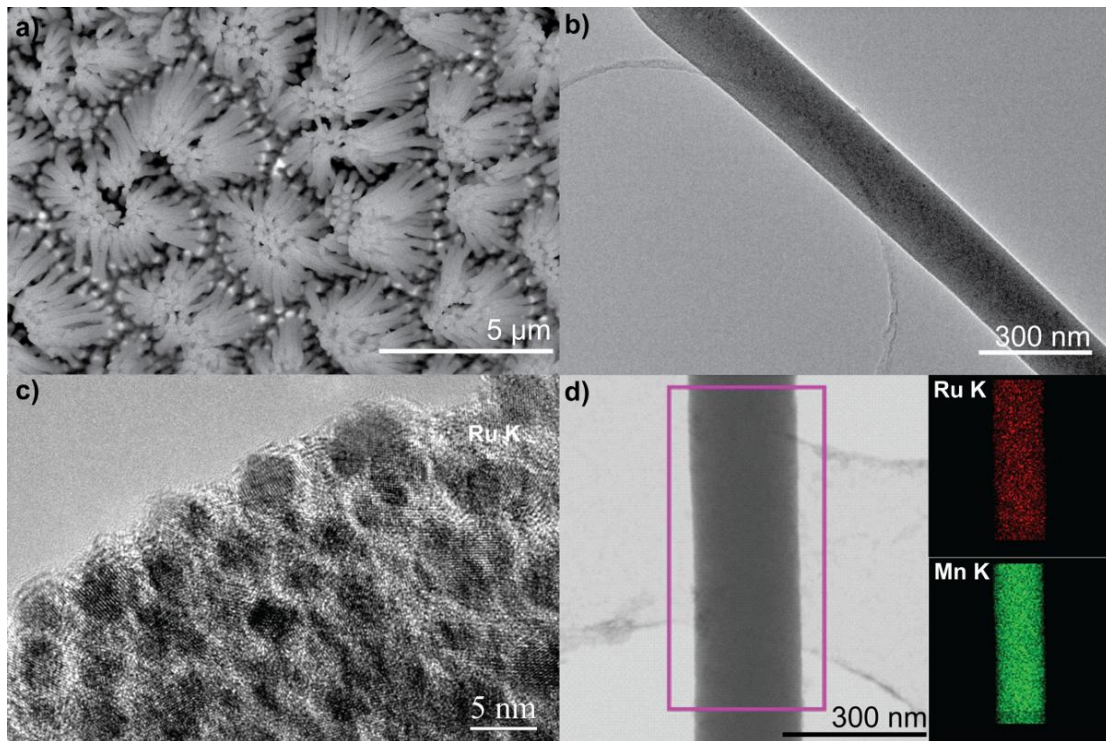


Figure 4.1 SEM, TEM, and EDS images of RuO₂-MnO₂ composite material

(a) SEM image of RuO₂-MnO₂ composite nanowires arrays (b) TEM image of a RuO₂-MnO₂ composite nanowire, (c) High resolution TEM (HRTEM) image of a section of a RuO₂-MnO₂ composite nanowire, (d) TEM image(left) and EDS mapping of Ru (top right), and Mn (bottom right) on a segment of a RuO₂-MnO₂ composite nanowire.

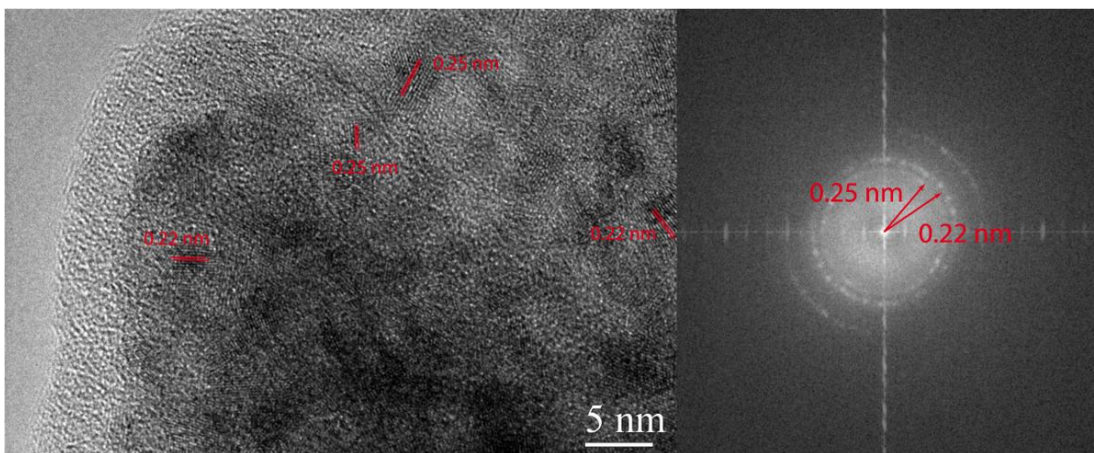


Figure 4.2 d-space measurements on TEM image and FFT resolved image.

TEM image of the RuO₂-MnO₂ composite material with d-space measured and marked on the TEM images. The corresponding FFT resolved image is shown on the right, same result of d space values are obtained here.

To confirm the chemical constituents of the nanowires arrays, Raman spectroscopy and X-ray photoelectron spectroscopy were used to characterize these samples. The Raman spectra of both pure and composite MnO₂ nanowires are shown in Figure 4.3a. For pure MnO₂, three major bands can be recognized around 503, 576, 652 cm⁻¹, which correspond well with Birnessite MnO₂.¹⁵² The Raman band at 576 cm⁻¹ is attributed to the (Mn–O) stretching in the basal plane of the MnO₆ sheet, while the feature at 652 cm⁻¹ can be viewed as symmetric stretching vibration (Mn–O) of the MnO₆ octahedron in the MnO₂·H₂O. For the RuO₂-MnO₂ samples, different Raman features are obtained. Here we show three Raman spectra obtained from RuO₂-MnO₂ grown in solutions with different RuCl₃ concentrations. With Ru³⁺ present in the electrodeposition bath, the peak at 652 cm⁻¹ disappeared and the 502

cm^{-1} peak becomes broader compared to the pure MnO_2 spectra. With increasing Ru ion concentration, the 576 cm^{-1} feature has decreasing signal intensity. This Raman change is caused by a structure distortion during RuO_2 co-deposition. A less ordered phase is formed with the addition of RuO_2 , resulting in fewer features in the Raman spectra. Due to the small loading amount, RuO_2 peaks were not detected in the Raman spectra. Therefore, we used XPS to confirm the RuO_2 deposition. Figure 4.3f shows the Ru 3d and C1s spectra of RuO_2 - MnO_2 nanowires. Although the Ru $3d_{3/2}$ spectra is obscured by the C 1s spectra, through deconvolution, we can still identify the Ru 3d doublet peaks located at the binding energy of 285.8 eV and 281.7 eV for Ru $3d_{3/2}$ and Ru $3d_{5/2}$, respectively.^{153,154} The Ru 3p spectra centered at 463.2 eV as shown in Figure 4 further confirms the presence of RuO_2 inside MnO_2 nanowires.

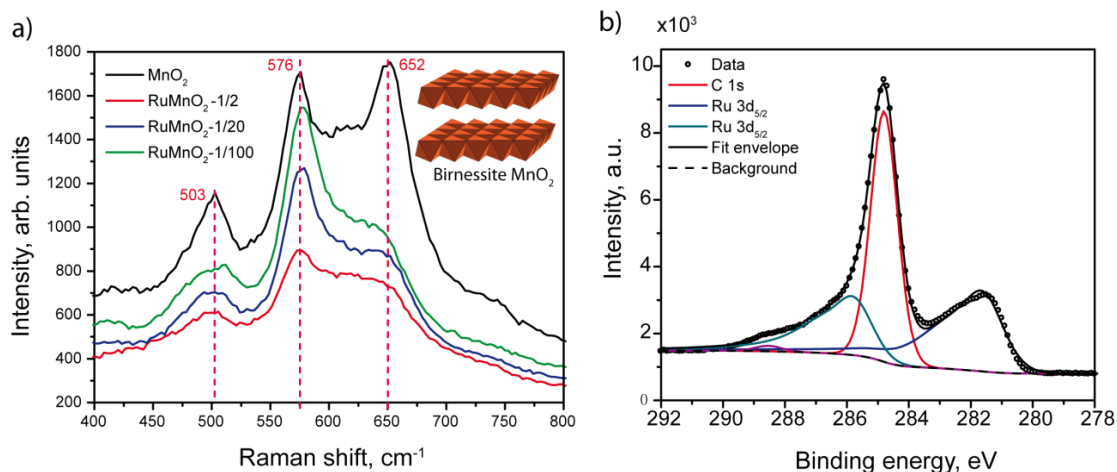


Figure 4.3 Raman and XPS characterization

(a) Raman spectra of pure MnO_2 (black curve) and $\text{RuO}_2\text{-MnO}_2$ prepared in solutions of different Ru/Mn ions concentrations ratios (red: 1/100, blue: 1/20, green: 1/2) and (b) XPS spectra of a $\text{RuO}_2\text{-MnO}_2$ sample. Ru $3d_{3/2}$ (red curve) and Ru $3d_{5/2}$ (blue curve) are deconvoluted and indicated. Inset of image a shows the schematic illustration of Birnessite MnO_2 structure.

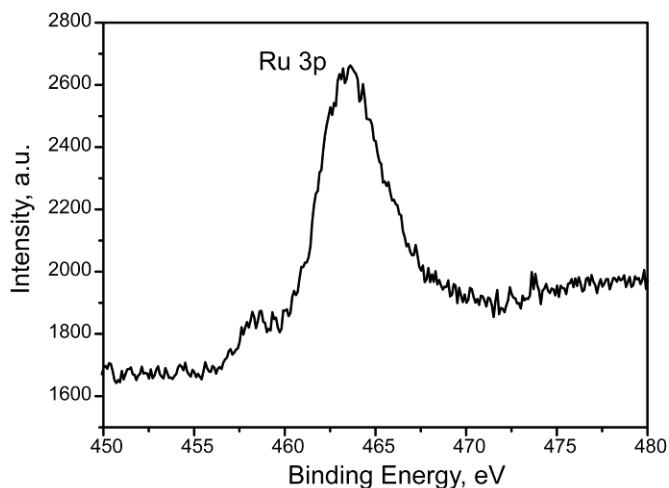


Figure 4.4 XPS spectra for Ru 3p in the $\text{RuO}_2\text{-MnO}_2$ composite material

4.3.2 Electrochemical Characterizations

For the electrochemical study of the RuO₂-MnO₂ composite nanowire arrays, we tested both MnO₂ nanowires with and without RuO₂ in a three-electrode system. As shown in Figure 4.5a, the cyclic voltammetry curve at 100 mV/s of a composite sample demonstrates a more rectangular shape than the pure MnO₂ sample as well as a higher cumulated area size. The squarer CV curve indicates a higher conductivity in the composite sample. While for the pure MnO₂ nanowires arrays, the intrinsic low conductivity causes the CV curve to deviate from the rectangular shape.¹¹ The higher cumulative area of the CV curve for the composite MnO₂ indicates a higher charge storage capability, which agrees with the galvanostatic charge/ discharge results for the two samples as shown in Figure 4.5b, evidenced by the longer charge/ discharge time for the composite nanowires at the same current density of 1.57 mA/cm². The CV curves of composite samples at different scan rates from 20-200 mV/s are shown in Figure 4.5c. The square shape of the CV curve is well-maintained even at high scan rates up to 200 mV/s. This is attributed to the improved conductivity from the RuO₂ loading. Specific capacitances calculated at different scan rates from 20 to 500 mV/s for both composite and pristine MnO₂ samples are compared in Figure 4.5d. The specific capacitance for pristine MnO₂ is calculated as 210 F/g at 20 mV/s, while for the composite samples, the capacitance increases by 44 % to 302 F/g. At a high scan rate of 500 mV/s, the capacitance is 112 F/g for pure MnO₂ and increased by 65 % to 185 F/g for composite sample. The significant improvement in capacitance, especially at high scan rates where performance is limited by the charge transfer speed, is attributed to the co-deposited RuO₂. RuO₂ itself is a well-known

supercapacitor material with mixed ion-electron conductivity and high capacitance.³³ Therefore, both the intrinsic high capacitance and good conductivity of RuO₂ may play a role in the capacitive improvement. However, the high capacitance value for RuO₂ in the literature is usually obtained only in tests using environmentally unfriendly acidic electrolyte. In this work, we use neutral aqueous electrolyte for all the electrochemical measurements. The reported value for RuO₂ in neutral electrolyte is around 230 F/g,¹⁵⁵ which cannot explain the high capacitance of the hybrid nanowires with a capacitance of 300 F/g. Therefore, we believe that the improved conductivity of the hybrid nanowires is playing a crucial role in advancing the electrochemical performance, as confirmed by the more rectangular shaped CV curve for the RuO₂-MnO₂ composite nanowires. Investigation of the charge transfer resistance, utilizing electrochemical impedance spectra, is discussed below to help gain insight into this composite material.

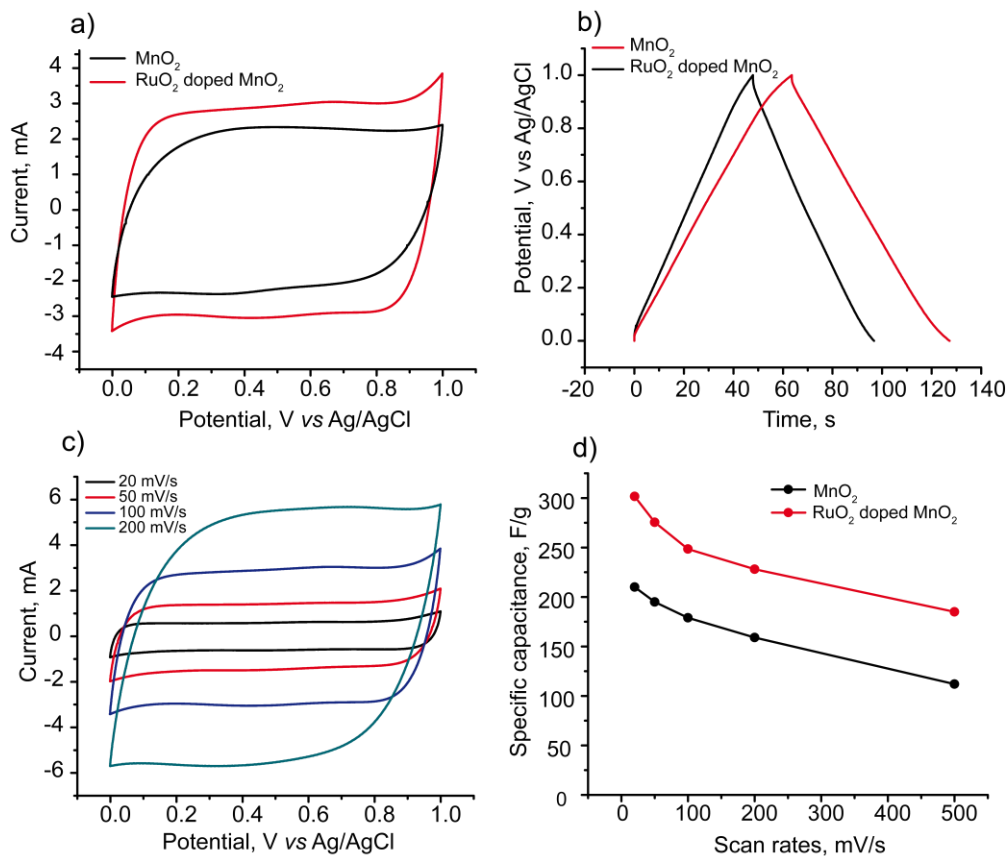


Figure 4.5 Electrochemical performance for bare MnO₂ and RuO₂-MnO₂ composite

(a) Cyclic voltammograms curves scanned at 100mV/s, and (b) galvanostatic curves at current density of 1.56 mA/cm² for pure MnO₂ nanowires (black curves) and 6.70 w.t. % RuO₂-MnO₂ composite nanowires (red curves), (c) CV curves of composite MnO₂ at different scan rates (20mV/s -200mV/s), (d) specific capacitances of RuO₂-MnO₂ (6.70 w.t.% RuO₂) nanowires (red), and pure MnO₂ (black) measured at different scan rates. All experiments were done in 1M Na₂SO₄ electrolyte with a potential window of 0-1 V vs. Ag/AgCl.

4.3.3 Effect of RuO₂ loading amount

To investigate the loading amount effect, we prepared MnO₂ nanowire arrays with different RuO₂ loading amounts (0.21%, 0.56%, 2.96%, and 6.70%, calculated by ICP-AES measurement on Ru and Mn peaks' intensities) by adjusting the solution compositions (see experimental part for solution concentrations and ICP-AES characterization). Figure 4.6a shows the rate performance for the four samples. The specific capacitances are 235 F/g, 253 F/g, 285 F/g, 302 F/g at 20 mV/s, and 154 F/g, 181 F/g, 206 F/g, 228 F/g at 200 mV/s for samples with increasing loading percentages (from 0.21% to 6.70%) of RuO₂, respectively. At the same scan rate, the capacitance increased with increasing RuO₂ amount. This phenomenon is attributed to contributions from two aspects: one is the intrinsic capacitance of RuO₂ and the other is the improved conductivity of the composite materials. In Figure 4.6b, we compare the Nyquist plots of the four samples with different RuO₂ weight percentages. All four plots approximate the behavior of a transmission line model developed by Macdonald.¹⁵⁶ Based on the extended study of the transmission line model, important electrochemical information can be extracted from the impedance behavior at low and high frequency.¹⁵⁷⁻¹⁵⁹ As shown in the Fig 4b, the high frequency real axis intercepts for the four samples are very close with a value around 10 ohms. This value represents the uncompensated solution resistance R_s . Therefore, all sample tested in the sample electrolyte of 1M Na₂SO₄ have the same R_s values. The real axis impedance of the almost vertical region at low frequency indicate the R_L that equals $R_s + R_e/3$, where R_e represents the electron transfer resistance in the MnO₂ nanowires. The R_e values for the four samples are calculated and listed in the inset

table in Figure 4.6b. With higher RuO₂ weight percentage, the electronic resistance of the composites calculated is lower. For example, the resistance of the sample with 0.21% RuO₂ is 223.8 ohm, while the one with 2.96% RuO₂ is 96.9 ohm. These EIS results confirm that the electronic resistance was effectively reduced by the co-deposition of RuO₂. These results also explain the improving capacitive performance of the samples with increasing RuO₂ loading amount.

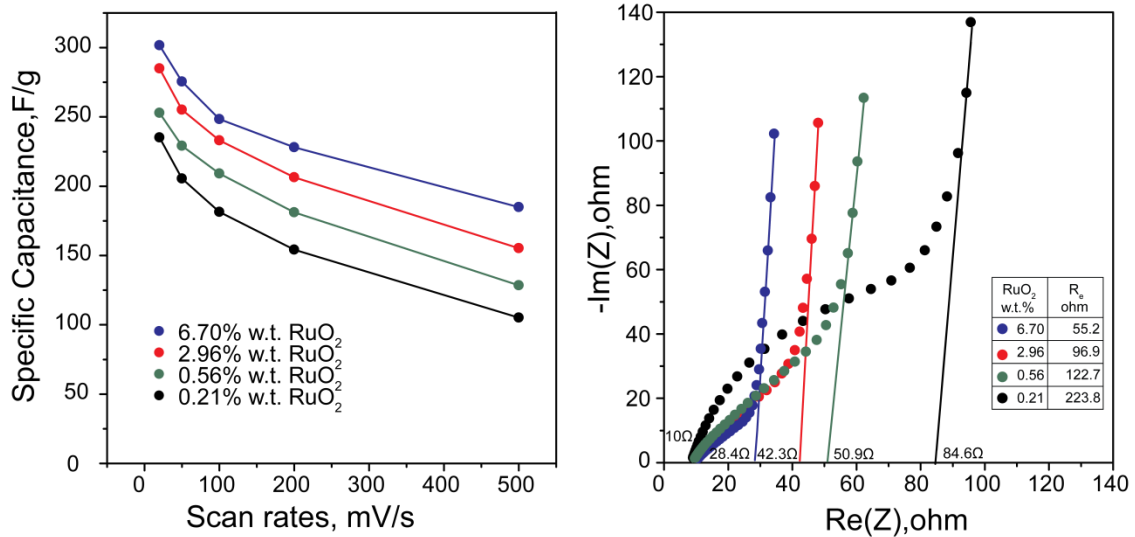


Figure 4.6 Capacitance and impedance behavior of RuO₂- MnO₂ composite nanowires

(a) Specific capacitances of RuO₂-MnO₂ composite nanowires at different scan rates from 20 mV/s to 500 mV/s, (b) Nyquist plot of different samples. Four samples with different loading amount of 0.21%, 0.56%, 2.96%, and 6.70% were prepared and tested here. Inset of image b show the electrical resistance values extracted from the Nyquist plot of the four samples.

4.3.4 Deconvolutions of the Capacitance

The charge storage in MnO_2 involves two processes. One is through the ions adsorption/desorption at the surface of MnO_2 and the second is through the proton (H^+) or alkali metal cations (C^+) intercalation/ deintercalation into the bulk MnO_2 material.⁴⁶ To explore the contribution of the RuO_2 on each of these two charge storage processes, we use two methods to quantitatively discriminate the two different processes. Deconvolution of the capacitances were conducted on both bare MnO_2 and composite MnO_2 samples with different RuO_2 percentages.

In the method developed by Trasatti,¹⁶⁰ voltammetric charges q stored at different scan rates v were first calculated. The extrapolation of q to $v=\infty$ of a plot of q versus $v^{-1/2}$ projects the charge accumulated at an infinite scan rate, which is associated with the surface stored charge q_{cap} through absorption/desorption processes. The extrapolation of q^{-1} to $v=0$ of a plot of q^{-1} versus $v^{1/2}$ gives the maximum charge q_{T} that can be stored in the active materials at slow enough scan rate when all the material will be reacted. Therefore, the charge q_{T} equals the sum of charges stored through both processes. Subtracting q_{cap} from q_{T} gives the charge that is stored by the diffusion-control insertion process, q_{in} . The corresponding specific capacitance values of q_{cap} and q_{in} can be calculated afterwards, representing the capacitive and insertion capacitance. The deconvoluted capacitive and insertion specific capacitance values for samples with different RuO_2 amount are listed in Figure 4.7a, 7b, respectively.

We also use the voltammetric sweep rate dependence to determine, quantitatively, the different process contributions to the current response according to a procedure reported previously by Dunn,¹⁶¹ and recently used by Penner *et al.*¹⁶² and our group¹⁶³. The current at a certain voltage is expressed by the following equation:

$$i=k_1v+k_2v^{0.5} \quad 1$$

In which the k_1v represents the current derived from the surface charge storage process, noted as the capacitive component, while $k_2v^{0.5}$ is associated with the diffusion controlled ion intercalation/deintercalation mechanism. To calculate the constant k_1 and k_2 values, equation 1 is converted to the following form:

$$i/v^{0.5}=k_1v^{0.5}+k_2 \quad 2$$

Plots of $(i/v^{0.5})$ versus $v^{0.5}$ were made at a specific potential based on the voltammogram data at different scan rates to obtain the k_1 (slope) and k_2 (intercept) values. The current contributions from the surface capacitive absorption (represented by k_1v term) and diffusion-controlled insertion processes (represented by $k_2v^{0.5}$ terms) were then deconvoluted for all samples. Based on the quantified voltammetric results (see examples in Figure 4.8), we can determine the capacitive and insertion based capacitance values at different scan rates. The capacitive capacitances deduced from both methods for MnO_2 with different RuO_2 amounts are plotted in Figure 4.7a. The capacitive capacitance shows an almost linearly increase with RuO_2 weight percentage in both Dunn's (red curve) and Trasatti's (black curve) deconvoluted results. While for insertion capacitance, as shown in Figure 4.7b, an increasing trend

is found from the bare MnO_2 to the composites with a small loading amount of RuO_2 (0.56 w.t.%) in all different color curves associated with different scan rates. Typically, in the Trasatti approach (black curve in Figure 4.7b), capacitance values increased from 92 F/g (for MnO_2) to 134 F/g (for RuO_2 - MnO_2). With further increasing RuO_2 amount, no significant enhancement in insertion capacitance was observed. Based on the different trends in the capacitive and insertion capacitance plots *versus* increasing RuO_2 percentages, we conclude that the RuO_2 has a different influence on the two charge storage processes in MnO_2 . This phenomenon is explained by the different limiting factors in the two processes. The capacitive contribution is stored through the surface ion absorption/desorption. Since ions have easy access to the surface of the nanowires, electrical conductivity dominated the capacitive performance. Therefore, composite samples with higher electrical conductivity will achieve better utilization of the active materials and obtain higher capacitive capacitance. For the insertion capacitance, which is ion diffusion limited, a less significant enhancement was found with increasing RuO_2 amount, since it only affects the electric conductivity. From the consistent charge separation results based on two methods, we confirmed that the advanced electrochemical performance demonstrated by the RuO_2 - MnO_2 composite nanowires originates from the enhancement in the materials electrical conductivity, which facilitates the capacitive charge storage process at the surface, showing an overall improved specific capacitance.

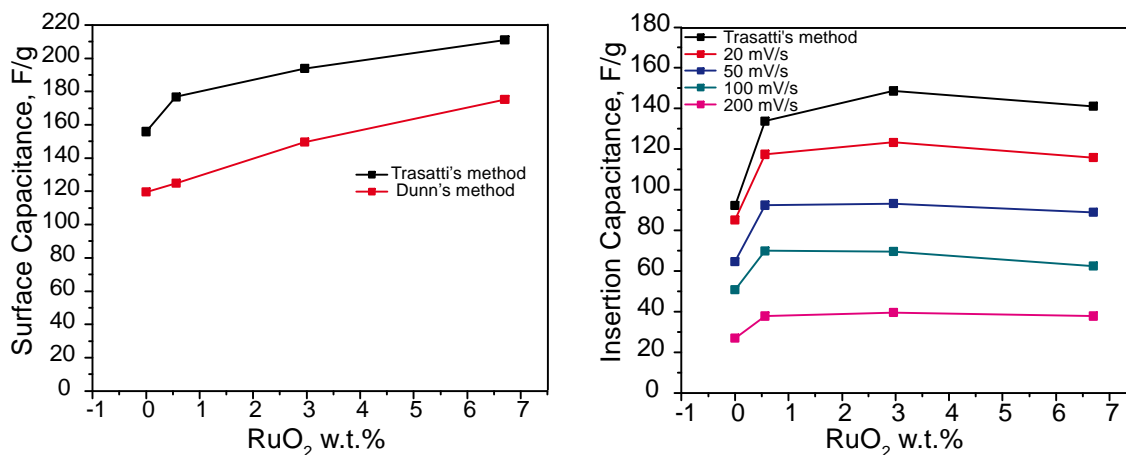


Figure 4.7 Deconvoluted capacitances for MnO₂ with different RuO₂ loading amount

Deconvolution result of the (a) capacitive capacitances, and (b) insertion capacitance for MnO₂ with different w.t.% of RuO₂.

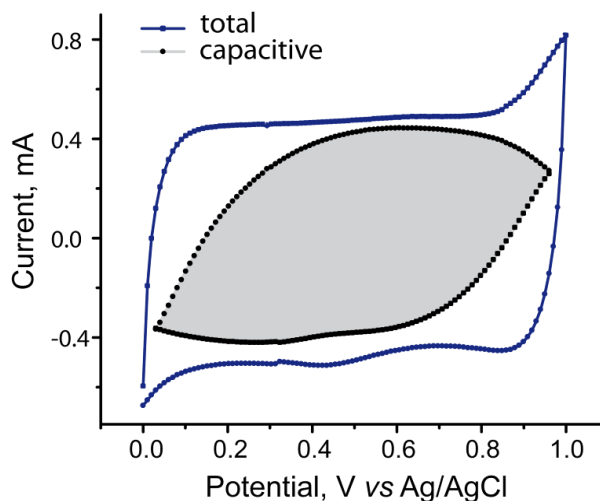


Figure 4.8 Voltammetric responses at 20 mV/s for the pristine MnO₂ nanowires

The total current (blue curve) is obtained experimentally. The capacitive currents (black curve in gray shadow) are deconvoluted by the Dunn's method. The capacitive capacitance is calculated based on the quantified capacitive voltammetry curve. And

the insertion capacitance is derived by the difference between the total and capacitive capacitance.

4.4 Conclusion

In this work, we use a one-step electrochemical co-deposition technique to obtain RuO₂-MnO₂ composite nanowires. The composite material shows a significant improvement in specific capacitance utilizing a neutral electrolyte. Increasing enhancement of the electrical conductivity with increasing RuO₂ weight percentage was confirmed by EIS results. Higher capacitances were found in samples with higher RuO₂ amounts. The RuO₂ contributions to the two charge storage processes in MnO₂, which either take place at the surface or in the bulk, were analyzed by two methods introduced by Trasatti and Dunn. Both capacitance separation results lead to the conclusion that the RuO₂ mainly influences the capacitive capacitance that is stored through ion adsorption/ desorption at the surface. This result is explained by the fact that the electron transfer limiting step in the capacitive capacitance is boosted while the ion diffusion limiting factor for the insertion capacitance is not influenced with increasing RuO₂ percentage. These easily prepared RuO₂-MnO₂ nanowire array, without any conductive additive, show promising supercapacitor performance. The synthesis method as well as the analysis of the RuO₂ loading amount effect can also be applied to other hybrid energy materials for better understanding of the synergistic co-operation mechanism and further optimization for their synthesis conditions and performances.

Chapter 5: Redox-Exchange Induced Heterogeneous RuO₂-Conductive Polymer Nanowires

5.1 Introduction

With the increasing demand for high performance energy storage devices, growing attention and research has been devoted to the fields of batteries and supercapacitors. Compared to high energy density batteries, which now have the highest energy storage device market share, supercapacitors with high power density are playing an increasingly important role in our lives in fields like transportation, industry and other consumer applications.^{9,7}

The most commonly used materials for supercapacitors include activated carbons, conductive polymers, and transition metal oxides.^{1,3-5} Among these, conductive polymers have drawn great interest due to their higher specific capacitance (100-250 F/g) compared to activated carbons (100-140 F/g) while still maintaining good conductivity.⁸ The charge in these polymers is stored through a highly-reversible near-surface redox process.^{58,59} The electrochemical performance can be improved by shortening the ion diffusion path for this redox reaction. Synthesis of variety of 0-D (nanoparticles), 1-D (nanowires, nanofibers, nanotube), and 2-D (nanoplates, nanobelts) nanostructured materials have been reported with this shorter path length ambition in mind.^{85,165-168,69,81,169} Porous anodic alumina has been widely applied for the synthesis of nanowire/ nanotube structures.¹⁷⁰⁻¹⁷³ Previously, our group has published accounts on the electrochemical deposition of conductive

polymer nanowire/nanotube arrays for high power supercapacitor materials using porous anodic aluminum oxide (AAO) as a template.^{110,109}

However, the energy density of these polymers is still restricted by their intrinsically low RuO₂ loading level, which is around one electron per two or three monomeric building blocks.⁵⁸ Therefore, heterogeneous nanomaterial combining the properties of conductive polymers with high energy density materials can be applied here to address this problem. In our previous work, we reported a simple method to synthesize MnO₂-nanoparticle enriched-PEDOT nanowires through a redox reaction between the sulfur in the thiophene group and the permanganate ion. This heterogeneous material was shown to successfully increase the total capacitance by 4-fold over the unmodified polymer nanowire.¹¹¹

Here, we expanded the study of this method to synthesize RuO₂-loaded nanowires made of different conductive polymer (PEDOT, PPY) matrices utilizing K₂RuO₄. RuO₂ is known to exhibit a mixed proton-electron conductivity, with electron transport along the dioxo bridge and proton transport through the structural water resulting in a superior supercapacitor performance.^{33,174} Electrodeposited RuO₂ nanotubes were reported to show a ultrahigh capacitance of 1300 F/g after annealing post-treatment by Hu *et al.*⁴⁰ By applying the redox-exchange method, RuO₂ is shown here to be redox-exchange induced through the reaction with sulfur in the thiophene (resulting in sulfone group)¹¹¹ in the PEDOT matrix and through reaction with β-carbon of the pyrrole ring, forming carbonyl groups in the PPY backbone (resulting in overoxidized polypyrrole).^{175,176}

Interestingly, the RuO₂ synthesized by reaction with the PPY nanowires forms a thin layer of coating on the outside of the nanowires, while for the reaction with PEDOT, RuO₂ exists in the form of nanoparticles randomly dispersed throughout each nanowire. This difference in RuO₂ loading location is thought to be due to different porosity of these two polymers. For the relatively porous PEDOT with an open-ended tip, K₂RuO₄ solution can easily penetrate into the nanowires, and the pores inside the nanowires can provide vacancies for the redox exchange-induced RuO₂ nanoparticles. While in the dense PPY nanowires, the reaction only takes place on the exposed outer shell of the nanowires. Therefore, RuO₂ forms a thin layer on the outside as a shell.

Even so, in both heterogeneous nanocomposites, RuO₂ has a short diffusion path for fast ion insertion and a conductive polymer backbone for facile electron transfer. Therefore, high specific capacitances of 371 F/g and 500 F/g were reached for the heterogeneous PEDOT and PPY based nanomaterials, respectively. The specific capacitances attributed to RuO₂ in PPY and PEDOT polymers was calculated to be around 800 and 1200 F/g, respectively, which are close to the theoretical value of amorphous RuO₂ · xH₂O (1360 F g⁻¹ when x=0.5).^{44,39} We present this as a general route to grow metal oxides XO₂ (X=Ru, Mn) into different conductive polymer nanowires in order to target synergistic properties out of the two energy materials in a heterogeneous nanostructure. Accordingly, these heterogeneous materials have potential application for electrochemical biosensing. Both PEDOT and PPY have been used as the immobilization matrices in biosensors due to their good

conductivity, biocompatibility, and chemical stability.^{177,178} By using the nanostructured polymer, faster response times and higher output intensities can be achieved in the biosensor's performance.^{179,180} RuO₂ has also been applied for H₂O₂ and glucose detections.^{181,182} Peng et al. have reported a highly sensitive microRNA biosensor using RuO₂ nanoparticles.¹⁸³ The hybridization of the polymer and RuO₂ materials within the nanowire structure can be suitable for enzyme immobilization with immense detecting ability

5.2 Experimental Section

5.2.1 Chemicals and Materials

3,4-Ethylenedioxythiophene (EDOT), potassium perruthenate, potassium permanganate, and acetonitrile were obtained from Sigma Aldrich (Milwaukee, WI). Lithium perchlorate was obtained from Fisher Scientific (Fair Lawn, NJ). Gold electroplating solution (Orotemp 24) was purchased from Technic (Cranston, RI). Deionized water (ca. 18MΩ • cm resistivity) was made by a Milli-Q water purification system from Millipore (Dubuque, IA). Alumina membranes, with a pore diameter of 200 nm and thickness of 60 μm, are commercially available from Whatman (Clifton, NJ).

5.2.2 Synthesis

PPY nanowires were synthesized potentiostatically in aqueous solution of 0.1 M pyrrole and 0.1 M lithium perchlorate using an anodic aluminum oxide (AAO) membrane as a template. First, a thin layer of gold (ca. 500 nm) was sputtered on the

branch side of an alumina membrane. A strip of 3M copper tape was attached to the gold side of the template in order to connect it to an electrical circuit. An electroactive window of AAO template (0.49 cm^2) was defined and sealed by silicone rubber. First, a flat-top gold electrode was grown inside the AAO by electrodepositing gold galvanostatically at a cathodic current of 1.0 mA/cm^2 for 15 min using a gold plating solution. This working electrode was then placed into the electrolyte bath with a Ag/AgCl reference electrode and a platinum foil counter electrode. A constant voltage of 0.8 V was applied until a total charge of 300 mC was passed. A vertically aligned array of freestanding PPY nanowires was obtained by soaking the template in 3 M NaOH for 15 minutes followed by rinsing with deionized water. PEDOT nanowires were prepared in the similar way, but by using an acetonitrile solution of 0.1 M EDOT and 0.1 M lithium perchlorate as the electrodeposition bath and applying a higher constant potential of 1.2 V vs. Ag/AgCl. Both polymer nanowire arrays were subsequently exposed to a 10 mM potassium perruthenate solution for 6 min to form the heterogeneous nanocomposites composed of RuO_2 decorated polymer (PEDOT or PPY) nanowires.

To prepare an efficient amount of polymer samples for the BET measurement, we used electrodeposited polymers films. Both PEDOT and PPY were grown on to Au-sputtered glass slide. After air-drying at room temperature, the polymer film was peeled off from the glass slide. Electrodeposited PPY formed a continuous film and can be easily peeled off from the glass-Au substrate. While for the PEDOT film, there was a strong adhesion between the polymer film and the Au layer. As we peeled the

film, PEDOT came off together with the Au layer from the glass slide. There were also some black powders loosely deposited at the film surface as well. For comparing purpose, a charge of 30 C was applied for both polymer depositions onto Au-sputtered glass slide substrates with an active deposition area of 8.75 cm² using the same conditions as applied for the nanowire growth. The nitrogen adsorption isotherms were measured at 77 K, and the polymer samples were degassed at 343.15 K for 4 hours before the measurement.

5.2.3 Characterizations

Imaging of RuO₂-polymer nanowires was acquired using a field emission scanning electron microscope (Hitachi SU-70 FEG-SEM, operated at 5 eV), and a transmission electron microscope (JEOL JEM 2100 FE-TEM).

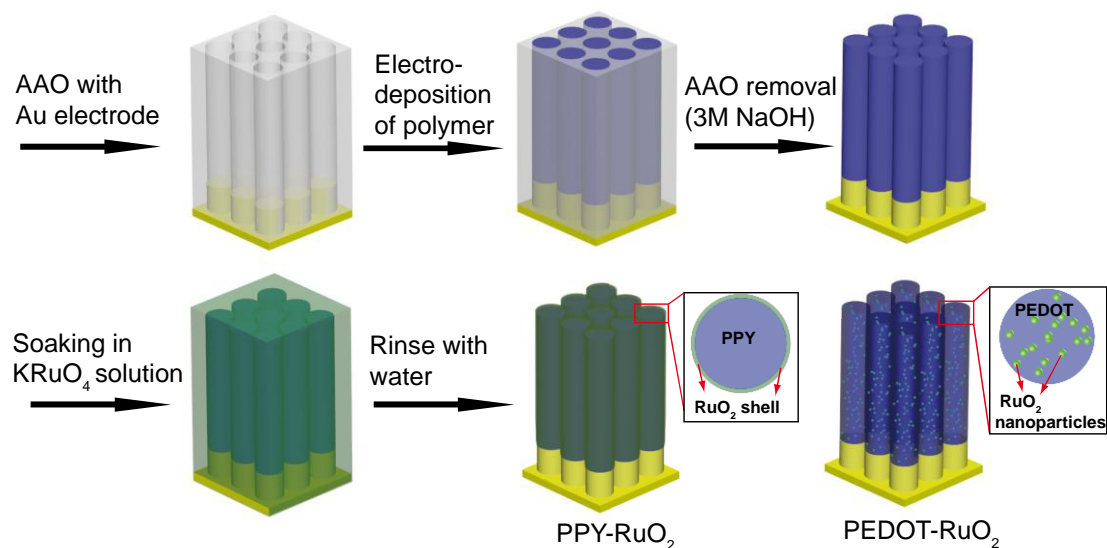
XPS analysis was done on a Kratos AXIS 165 spectrometer. The C 1s peak was calibrated at 284.8 eV. Casa XPS software was used to obtain the components for the fitted curves.

Inductively Coupled Plasma-Atomic Emission Spectroscopy (ICP-AES) characterization was performed on a Perkin Elmer ICP-Optima 4700. Intensities were measured at 240.272 nm for Ru. Calibration curves were made from Ru standards traceable to the National Institute of Standards and Technology (NIST). RuO₂-polymer samples were dissolved in freshly made aqua regia solution (prepared by mixing 3:1 concentrated HCl: HNO₃) and diluted to a known volume before being administered to the plasma.

The electrochemical studies of RuO₂-polymer nanowires were performed in a standard three-electrode system utilizing a bipotentiostat (BI-STAT, Princeton Applied Research). Ag/AgCl was used as the reference electrode and Pt was used as the counter electrode. Both cyclic voltammetry and galvanostatic charge/ discharge tests were done in an electrolyte of 1 M H₂SO₄ with a potential window of 0.6 V or 1 V.

5.3 Results and Discussion

5.3.1 Growth Scheme and Structural Characterizations



Scheme 5.1 Synthesis of heterogeneous RuO₂-Polymer nanowires

Two different architectures were obtained using different polymer nanowires (PPY or PEDOT), as represented by the last two figures (insets of the two figures show the cross-section views). For PPY nanowires, RuO₂ was preferentially formed on the

surface of the PPY nanowires as a shell. For PEDOT nanowires, RuO₂ grown all through the nanowires as nanoparticles.

Scheme 5.1 shows the synthesis process for the RuO₂-Polymer nanowires. First conductive nanowires were grown by an electrochemical method inside an AAO template (Scheme 1a-c). After removal of the template (Scheme 1d), the free-standing polymer nanowires were soaked in potassium perruthenate solution for 6 min (Scheme 1e), resulting in redox-induced RuO₂ loading of the polymer. In this study, we use two kinds of conductive polymers as the matrix: PEDOT and PPY.

As shown in Figure 5.1, we can see that the current transients for the PEDOT and PPY potentiostatic electropolymerization are very different. The PEDOT transients show a higher growth rate than the PPY, and the current is changing during the polymerization process. While for PPY, the current remained at steady low level for most of the time. At higher polymerization rates, the polymer tends to be less ordered and more porous. On the other hand, with low growth rate, monomers and counter ions have enough time to diffuse to the bottom of the AAO template, leading to the growth of rigid, dense nanowires. The average lengths for intact PEDOT/PPY polymer nanowires were also measured as shown in Figure 5.1. With the same charge density for electrodeposition, PEDOT nanowires have an average length of 8 μm, compare to 3-4 μm for PPY, which indicated more dense nanowires for PPY and more porous structure for PEDOT. Different morphologies of electropolymerized PEDOT, PPY, and polyaniline under different conditions have been reported.^{110,184} In addition, electropolymerized PEDOT has been previously shown to have a more porous structure than PPY.^{185,186} Thus, we investigated PEDOT's and PPY's surface

area and pore distribution by measuring nitrogen adsorption isotherms of electrodeposited polymer films. As shown in Figure 5.2, PEDOT film is characteristic of a higher surface area and wider pore range than the PPY film, indicating a more porous morphology compared to the PPY.

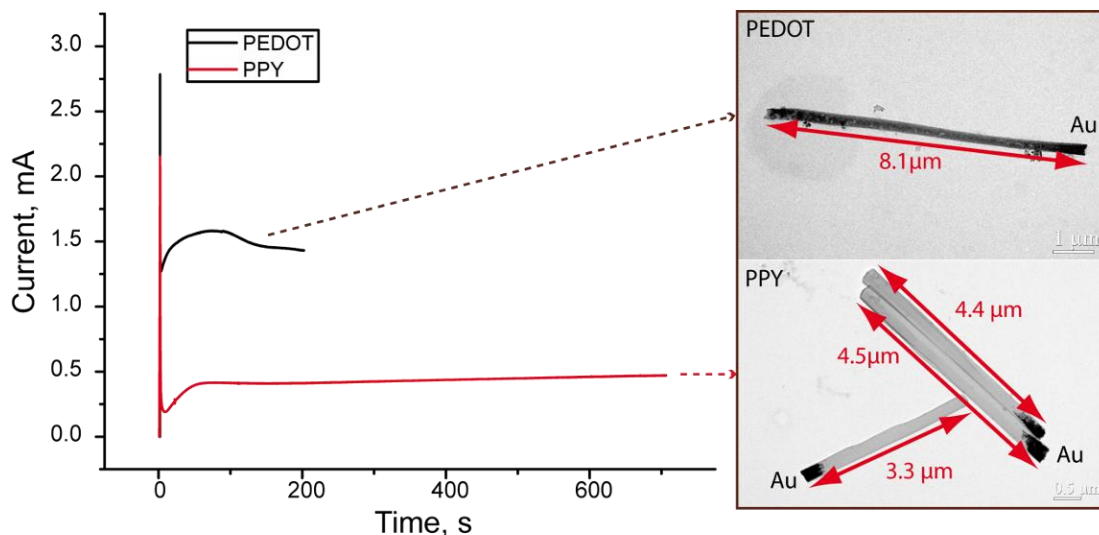


Figure 5.1 Potentiostatic transients for the Polymer electrodeposition

Potentiostatic transients for the growth processes of PPY (red curve) and PEDOT (red curve) nanowires with charge of 300 mC. The corresponding TEM image of intact individual polymer nanowires are shown on the right with Au bottom indicated. The lengths of the individual nanowires are marked. Based on a large amount of sample length measurements, the average length of 300 mC PEDOT is around 8 μm , and the length for 300 mC PPY is around 3-4 μm .

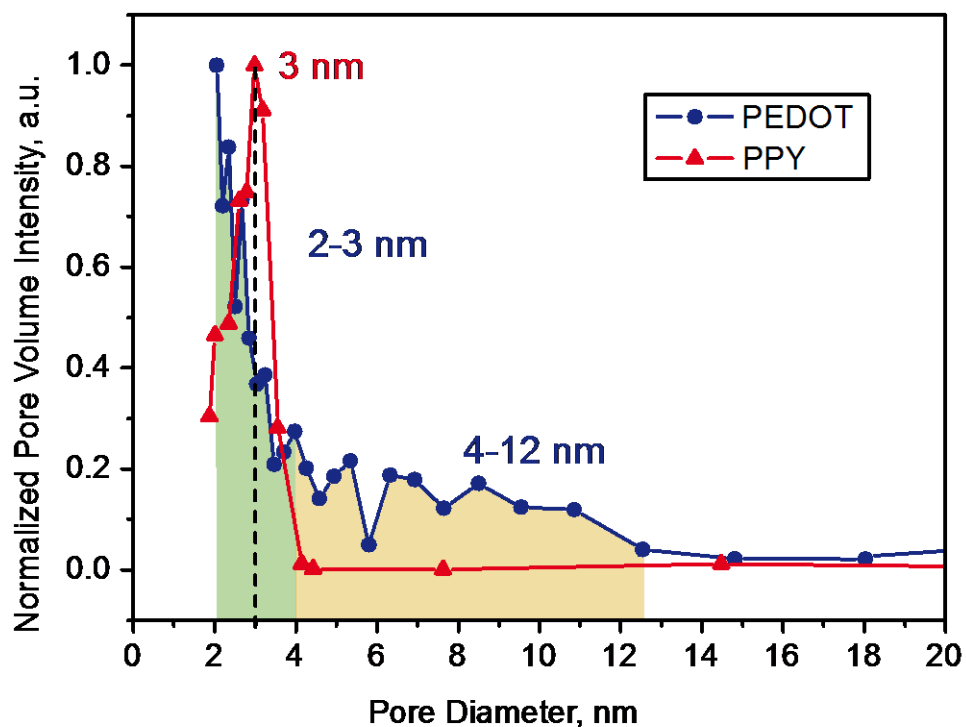


Figure 5.2 Barrett-Joyner-Halenda pore-size distribution curves from N_2 adsorption branches of PEDOT and PPY films.

Figure 5.3 a shows the SEM images of RuO_2 loaded PEDOT nanowire arrays. As can be seen, the nanowires are flexible and reveal a cigar shape at the end of these nanowires. We can see some dark spot areas along the nanowire from the TEM image in Figure 5.3 b (taken from a segment of a single nanowire), which becomes clear in Figure 5.3 c at higher resolution.

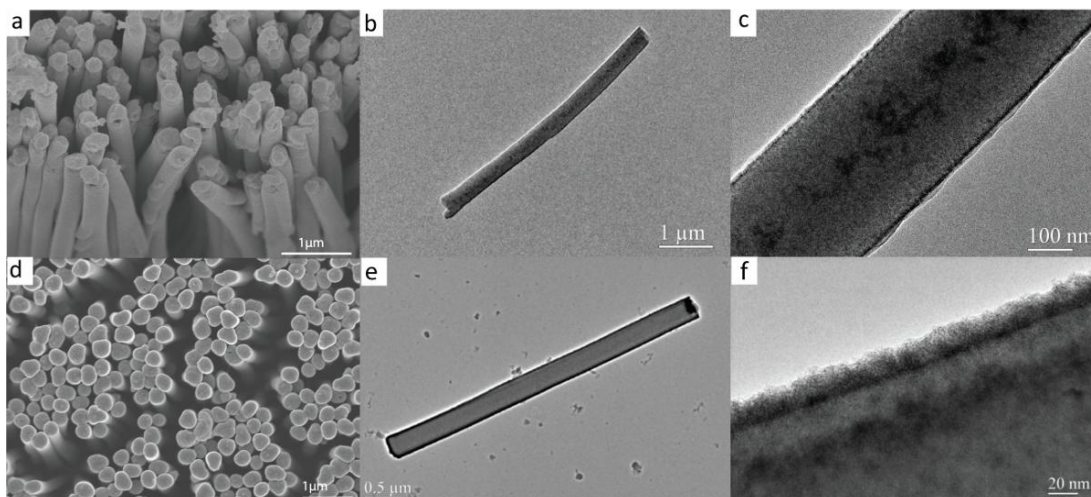


Figure 5.3 SEM and TEM images for different polymer nanowires

(a) SEM and (b,c) TEM images of PEDOT nanowires after being treated with KRuO_4 for 6 minutes, (d) SEM and (e,f) TEM images of PPY nanowires after being treated with KRuO_4 for 6 minutes.

To confirm and analyze the RuO_2 loading within the polymer, we did both energy dispersive spectroscopy (EDS) mapping and line scans on a segment of a RuO_2 -PEDOT nanowire. The Ru K map and S (sulfur from the thiophene ring on PEDOT) K map results are shown in Figure 5.3 a-c. The S K map shows same S signal intensity all through the map area, and the Ru K map shows higher signal intensity in some area, which matches well with the dark areas in the TEM image. This indicates that the dark spots throughout the nanowires present the RuO_2 loading inside the PEDOT matrix.

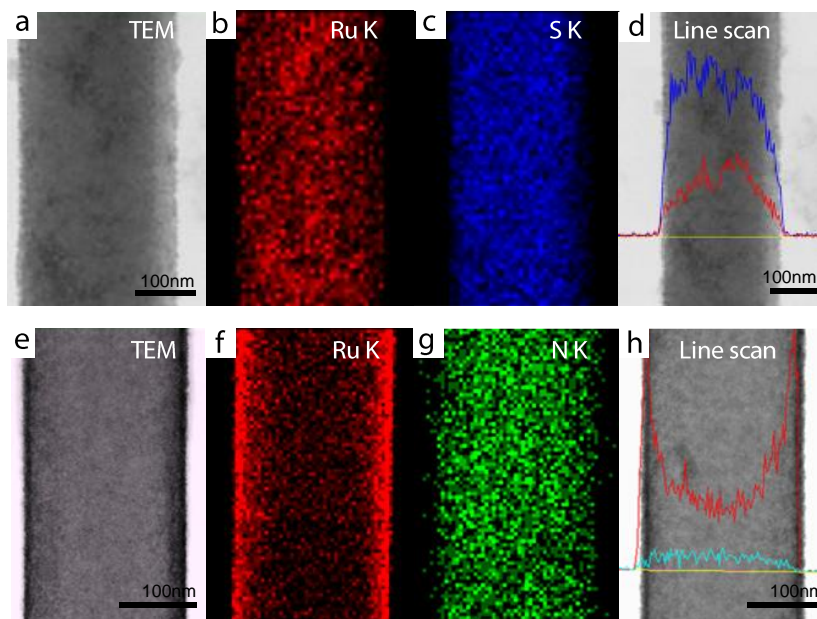


Figure 5.4 EDS element mapping and line scan results

(a) TEM image and EDS mappings of (b) Ru, and (c) S on a segment of a RuO₂-PEDOT nanowire, (d) line scan of Ru (red line) and S (blue line) across a single RuO₂-PEDOT nanowire, (e) TEM image and EDS mappings of (f) Ru, (g) N on a segment of a RuO₂-PPY nanowire, (h) line scan of Ru (red line) and N (blue line) across a single RuO₂-PPY nanowire.

It is thought that the RuO₂ formation sites are provided by the PEDOT intrinsic porous structure. As discussed in previous work on MnO₂-PEDOT nanowires, PEDOT synthesized by electrochemical deposition have nanoscale pores.¹¹¹ EDS line scan result (Figure 5.4d) across the nanowire also shows that Ru exists all throughout the nanowire. The distribution of RuO₂ in the PEDOT polymer is similar to the result in our previous work on MnO₂ nanoparticle enriched-PEDOT nanowires, in which

MnO₂ nanoparticles were formed well throughout the PEDOT matrix via the redox exchange of permanganate ions with the sulfur in the thiophene ring of PEDOT.¹¹¹

SEM and TEM images of K₂RuO₄ treated PPY nanowires are shown in Figure 5.3 d-f. Compared to PEDOT nanowires, the PPY nanowires appear more rigid with smooth surfaces (see Figure 5.3e). This is attributed to the slow growth rate we used for the PPY nanowires. As shown in Figure 5.3d, even the top of the PPY nanowires are dense and flat, different from the tubular top of the PEDOT ones (Figure 5.3a). A TEM image (Figure 5.3e) of a single nanowire shows a darker color at the edges of the nanowires than in the center. Higher resolution image (Figure 5.3f) reveals that there is a thin layer of coating on the PPY nanowires presented by the roughened and darkened layer on the outside of the nanowire.

To confirm the distribution of RuO₂ in the polymer nanowires, we again used EDS mapping and line scan characterization. The Ru K map in Figure 5.4 f shows that Ru signal mainly came from the outer shell of the nanowires. The line scan result for Ru K in Figure 5.4 h clearly shows two signal peaks at the two outside edges of the nanowire, which confirms that the RuO₂ was preferentially formed on the outer surface of the PPY nanowires. This phenomenon was also observed when KMnO₄ solution was used for PPY nanowires: as shown in Figure 5.5. After a 6 min soaking time in 10 mM KMnO₄, a roughened layer was formed onto the surface of PPY nanowire (see Figure. 5.5 a, b). In Figure 5.5 c, the EDS line scan result of Mn K across a single MnO₂-PPY nanowire shows the same shape as in Figure 5.4 h for Ru K line scan result across RuO₂-PPY nanowires. This indicates the same structural characteristic was observed for both MnO₂-PPY and RuO₂-PPY nanowires. The

redox exchange product (MnO_2 or RuO_2) was formed as a layer on the PPY nanowires due to the dense nanowires structure of PPY comparing them to the porous PEDOT ones.

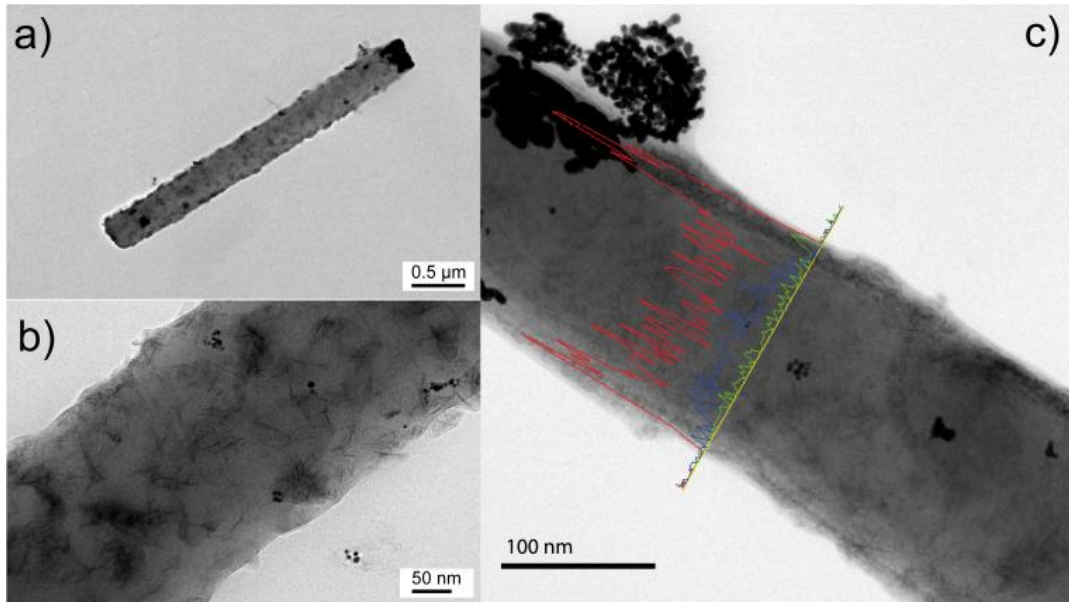


Figure 5.5 TEM images and EDS line scan result on MnO_2 -PPY nanowires

(a,b)TEM images of MnO_2 -PPY nanowires, and (c)line scan of Mn (red line) and N (blue line) across a single MnO_2 -PPY nanowire. As shown in image a,b, MnO_2 forms as a coating on the PPY nanowires, and the EDS line scan of Mn shows a peak signal at the two edges corresponding to the MnO_2 coating formed as a shell on the nanowires. This demonstrates the same growth mechanism was observed for both MnO_2 and RuO_2 .

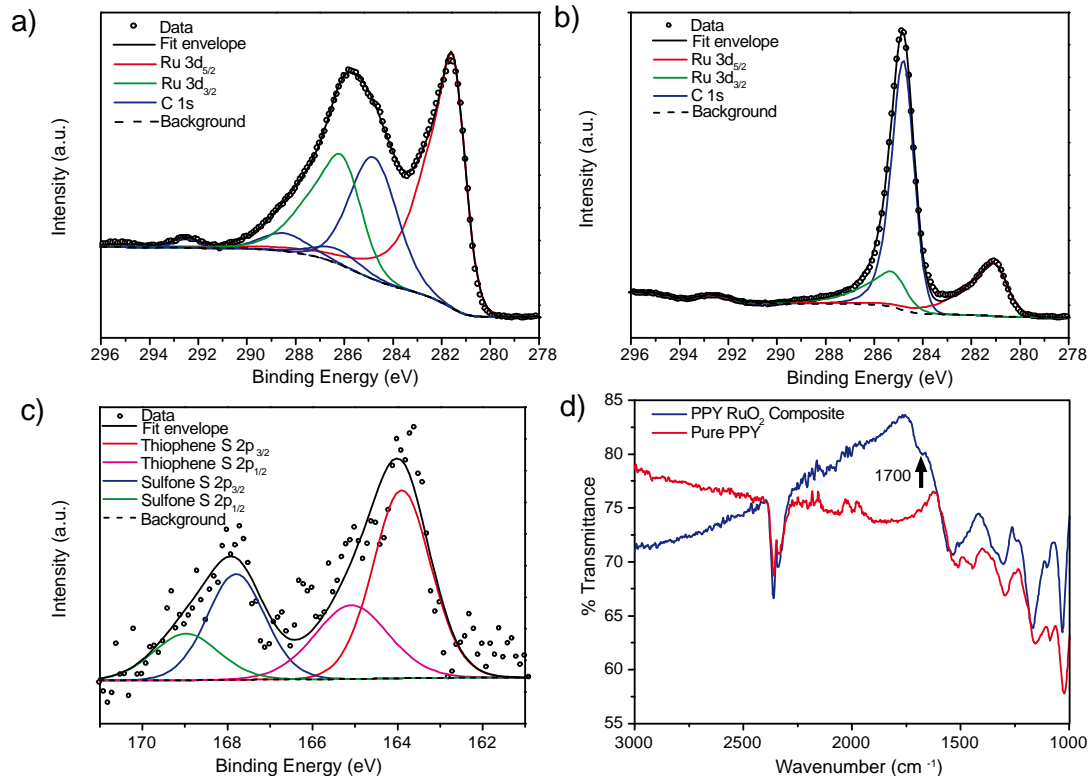


Figure 5.6 XPS and FTIR on the hybrid RuO₂-polymer nanowires

(a, b) XPS spectra and deconvolution of C 1s and Ru 3d spectra for KRuO₄ treated (a) PEDOT and (b) PPY nanowires, (c) XPS spectra and deconvolution for S 2p spectra in KRuO₄ treated PEDOT nanowires, (d) FTIR spectra for pure and KRuO₄ treated PPY film deposited on ITO, inset show optical images of both.

The chemical composition of the ruthenium oxide is supported by X-ray photoelectron spectroscopy (XPS) results. Figures 5.6 a and 5.6 b shows the Ru 3d and C 1s spectra of RuO₂-PEDOT nanowires and RuO₂-PPY nanowires, respectively. Since the C 1s spectra overlap with the Ru 3d signal, deconvolution has been performed. Both samples show one spin-orbit doublet with Ru 3d_{5/2} peak at

BE=281.6 for PEDOT and BE=281.1eV for PPY composite nanowires, and Ru 3d_{3/2} peak at BE=286.2 eV for PEDOT and BE=285.3 eV for PPY composite nanowires. Both doublet positions are in agreement with the reported data for hydrous RuO₂.^{154,187–189}

Accordingly, the XPS result for the RuO₂-PPY nanowires show a molar ratio of 1: 7.206 for Ru to O based on the Ru 3d and O 1s signal intensities and sensitivity factors. The O 1s can be deconvoluted into three contributions, including O²⁻ (oxygen bound to ruthenium), OH⁻, and H₂O (surface bound O).^{190,191} With 27.04 % of the O signal attributed to the O²⁻, we were able to calculate that the ruthenium oxide had the chemical formula of RuO_{1.95}, which further confirms the formation of ruthenium (IV) oxide. The Ru 3p spectra were also investigated to further confirm the existence of RuO₂. (See Figure 5.7).

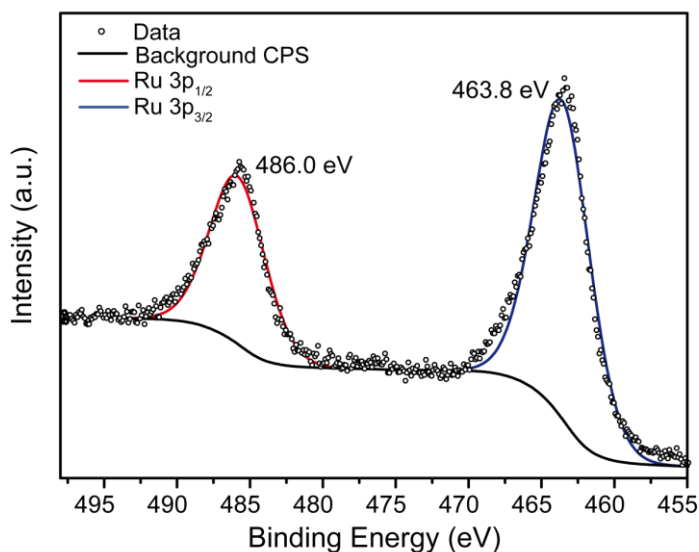


Figure 5.7 XPS Ru 3p spectra of composite PEDOT-RuO₂

The Ru 3p peaks at 486.0 and 463.8 eV agree with the reported value for hydrous RuO₂.¹⁻² Similar Ru 3p spectra was also found for PPY- RuO₂ sample.

As discussed in the previous work, the thiophene sulfur in the PEDOT is oxidized to sulfone by the strong oxidizing agent KMnO₄. Because KRuO₄ has very similar oxidizing properties as KMnO₄, the same redox reaction thought to occur here with PEDOT. As shown in Figure 5.6c, the S 2p spectra of RuO₂-PEDOT nanowires show two peaks representing two different sulfur functional groups in the sample. By deconvoluting the spectra, we obtained two pairs of S 2p peaks, corresponding to the sulfur in the thiophene group and sulfone group in the polymer. The sulfone peak was only formed after soaking the PEDOT nanowires in the potassium perruthenate solution.¹¹¹

We also investigated the N 1s spectra of RuO₂-PPY (see Figure 5.8). However, because the PPY nanowires were covered by a thin layer of RuO₂, the N 1s spectra signal collected by the XPS surface characterization (around 6 nm) was too weak to be analyzed. Since it has been reported that the PPY can be overoxidized with the formation of carbonyl and hydroxyl groups, we decided to use FTIR to investigate this process.^{176,192-194} Here FTIR spectra of the PPY film before and after soaking in KRuO₄ were compared in Figure 5.6d. The raised band at 1700 cm⁻¹ of the blue curve was ascribed to the carbonyl group formed on the β-position of the pyrrole ring during the overoxidization process by KRuO₄.¹⁷⁶ In addition, the absorbance of the electronic transition band (slope of the baseline) decreased after loaded with RuO₂, in agreement with the previous reported result on overoxidized polypyrrole.¹⁹³

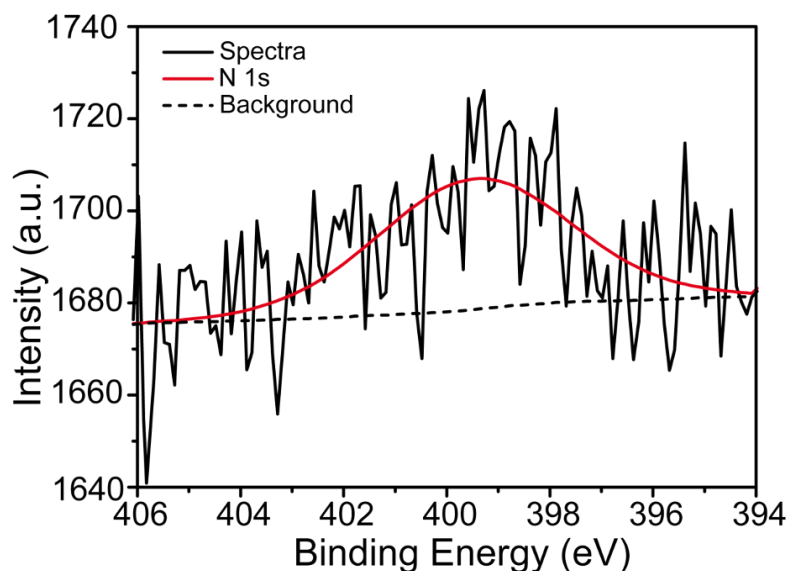


Figure 5.8 XPS spectra of N 1s of PPY-RuO₂

In this work, it is thought that the initial seeds of RuO₂ are formed from perruthenate through the reaction with the polymers, and these seeds catalyze the further water reduction of the highly oxidized RuO₄⁻ to RuO₂. For accurate determination of the loading amount of RuO₂, an ICP-AES instrument was utilized. Results from this indicate that for a 6 min soaking treatment, the RuO₂ mass is 66.9 μg in 300 mC PEDOT and 66.7 μg in 300 mC PPY. The molar ration of RuO₂ over monomeric unit is 0.37 for both polymers with the 6 min soaking time. The RuO₂ loading capability with different soaking times was studied based on the ICP-AES results as shown in Figure 5.9. With increasing soaking time, more RuO₂ was induced into the conductive polymers matrices as indicated by the almost linearly increasing ratio (Ru/polymer unite) values. The loading amount can also be tailored by controlling the concentration of KRuO₄ as discussed in our previous paper.¹¹¹

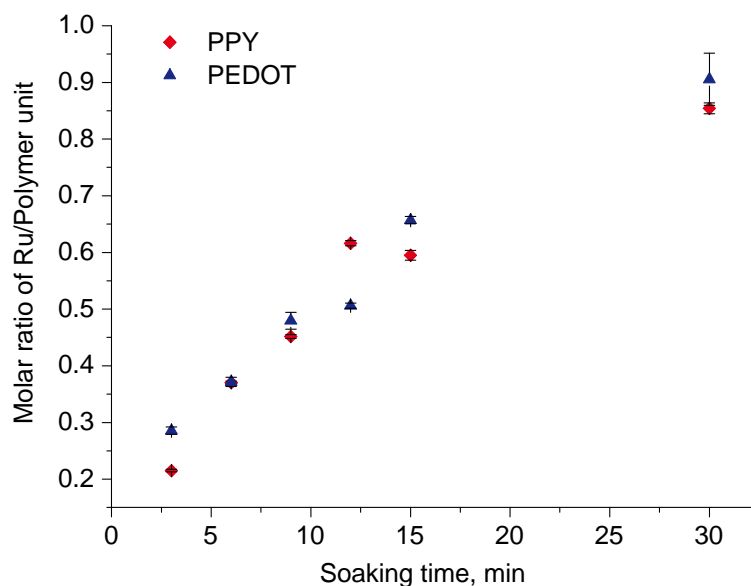


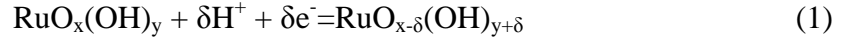
Figure 5.9 Effect of soaking time on the RuO₂ mass loading.

Loading capacity of RuO₂ (presented by the molar ratio of Ru/polymer unit) versus soaking time in 10 mM K₂Cr₂O₇. Both PEDOT and PPY nanowires were prepared with a charge density of 0.61 C/cm² over AAO template. Different soaking time of 3 min, 6 min, 9 min, 15min, and 30min were applied (Error bars indicate the standard deviation of three replicates measurements for each samples).

5.3.2 Charge Storage Mechanism and Electrochemical Characterizations

In order to characterize the electrochemical performance of the RuO₂ polymer hybrid nanowires, we use both cyclic voltammetry and galvanostatic charge/discharge techniques. PEDOT nanowires with and without RuO₂ loading were tested in 1 M H₂SO₄ in the voltage window from 0 to 1 V vs. Ag/AgCl electrode. An anodic peak appears at 0.5 V after the treatment with K₂Cr₂O₇ solution in Figure 5.10a which is

caused by the following reaction, where protons are intercalated and de-intercalated from the ruthenium oxide material:



The specific capacitance was calculated to be 371 F/g at a scan rate of 20 mV/s for the composite RuO_2 -PEDOT nanowires based on the total mass of the hybrid nanowires, compared to 82 F/g for the pure PEDOT nanowires at the same scan rate. As shown in Figure 5.10 b, the red galvanostatic curve of PEDOT based composite nanowires show a longer charge/discharge time than the pure PEDOT nanowires (black curve) at the same current density, indicating a high charge storage capability.

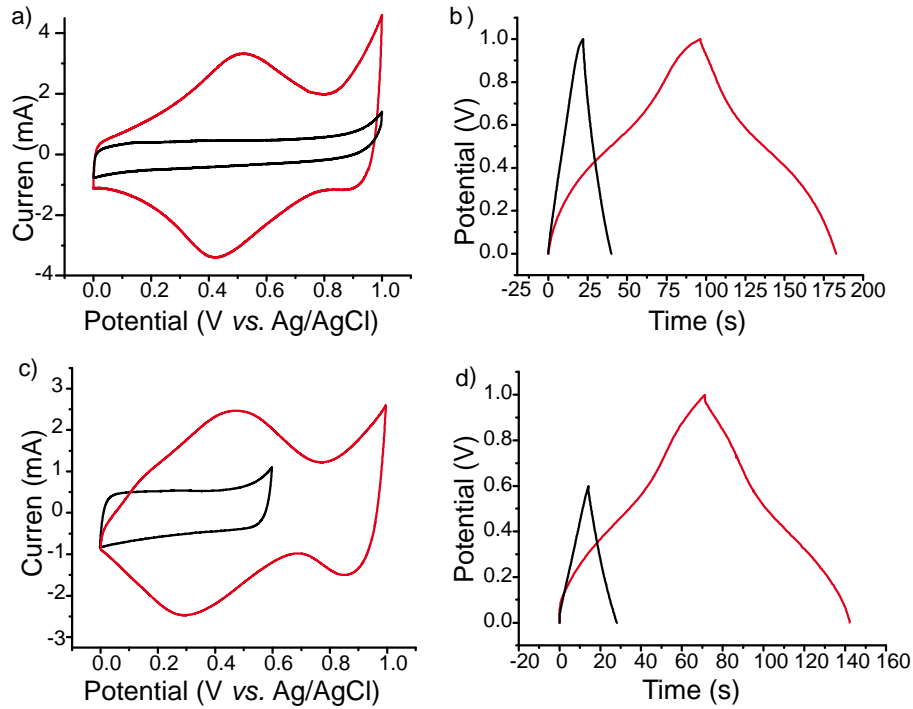


Figure 5.10 Electrochemical characterizations of the RuO_2 -polymer nanowires

(a) Cyclic voltammogram PEDOT nanowires before (black) and after (red) being treated with 10mMKRuO₄ for 6 minutes at a 20 mV/sec scan rate in a 0.1 M H₂SO₄ aqueous electrolyte (b) Galvanostatic charge/discharge curves of PPY nanowires before (black) and after (red) being treated with 10m MKRuO₄ for 6 minutes at current density of 2 mA/cm² in a 0.1 M H₂SO₄ aqueous electrolyte

Figure 5.10 c shows the cyclic voltammetry curve of pure polypyrrole nanowires and KRuO₄ treated polypyrrole nanowires. For pure polypyrrole nanowires, a voltage window of 0 - 0.6 V vs. Ag/AgCl was chosen. At higher voltages, polypyrrole is known to undergo an irreversible oxidization process, and changes into an overoxidized polypyrrole with a concomitant loss of conductivity and electroactivity.¹⁷⁶ As shown in the black curve in Figure 4c, the anodic current start to increase when the potential approaches 0.6 V, beyond which the overoxidization will start to occur.^{195,196} However, after being treated with KRuO₄ solution, the RuO₂ coating was formed on the outside of the nanowires, which functions here as a protective film and helps extend the voltage window to 1V as shown in Figure 5.10c. The anodic redox peak that appears at 0.5 V vs. Ag/AgCl demonstrates the proton desertion process in RuO₂. The galvanostatic charge/discharge measured at 2mA/cm² in 1 M H₂SO₄ are shown in Figure 5.10 d for the PPY nanowires with (red curve) and without RuO₂ loading (black curve). The composite RuO₂-PPY nanowires can sustain over 140 s discharge time, which is almost 4 fold longer than 30 s of pure PPY operated at the same current density. This improvement in charge storage capability is contributed to the simple soaking treatment in KRuO₄. Taking account of added RuO₂

mass determined by ICP-AES measurement, the composite RuO₂-PPY nanowires have a specific capacitance of 500 F/g, compared to 252 F/g for the PPY nanowires at scan rate of 20 mV/s. Keep in mind that the energy density is proportional to the product of the specific capacitance and the square of voltage window. Here by coating the PPY with RuO₂ shell, we improved the voltage window from 0.6 V to 1.0 V in aqueous electrolyte. Therefore higher energy density performance can be expected from this composite material.

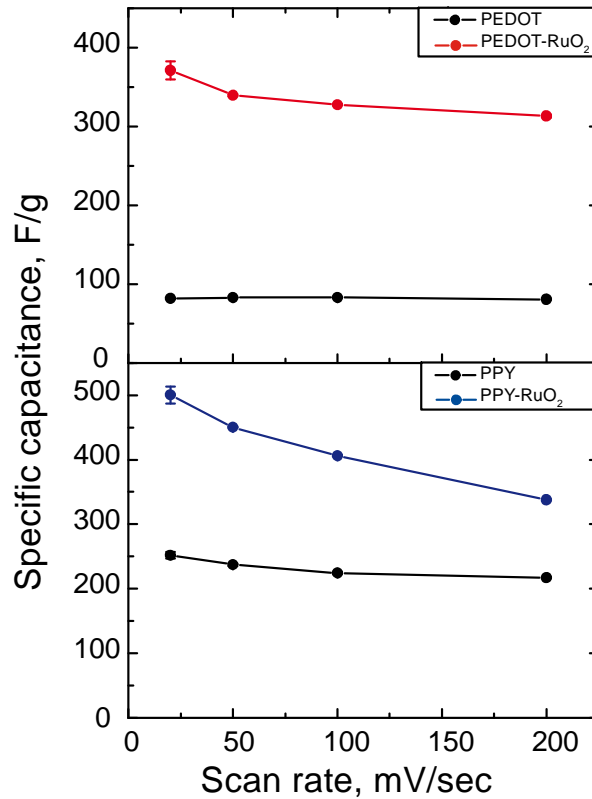


Figure 5.11 Specific capacitance of RuO₂-polymer nanowires.

Specific capacitances of PEDOT nanowires, PPY nanowires before and after addition of the RuO₂ materials through the redox-exchange reaction. (Error bars show the standard deviation for three replicates measurements at each scan rate).

In Figure 5.11, we show the specific capacitances of both polymer nanowires and RuO₂-polymer composite nanowires at different scan rates from 20 to 200 mV/s. According to the mechanism of RuO₂ formation, polymers will lose some of their electrical conductivities after reacting with K₂RuO₄ solution. However this part is not detrimental to the performance of the hybrid nanowires. For PEDOT, the rate performance is well maintained after addition of RuO₂ (with 85% capacitance retention with scan rate increasing from 20 mV/s to 200 mV/s). In the case of PPY, worse rate performance is seen after RuO₂ induction, the specific capacitance is still significantly improved compare to pristine PPY even at high scan rate of 200 mV/s, with capacitance value of 338 F/g (for PPY-RuO₂) compare to 217 F/g (for solely PPY). The calculated pristine specific capacitance values for RuO₂ in PPY and PEDOT reached 829 F/g and 1191 F/g respectively at 20 mV/s, compared to the theoretical capacitance number of 1360 F/g.^{44,39} There are mainly two reasons for these high capacitance values. First, both the PPY and PEDOT nanowires are conductive polymers, providing a conductive matrix for the charge/discharge process of the RuO₂ materials. Second, both the thin layer of RuO₂ on the surface of PPY nanowires and the highly dispersed RuO₂ nanoparticles throughout the PEDOT nanowires allow very short diffusion paths for proton insertion and desertion. Therefore, high utilization of the RuO₂ was achieved here.

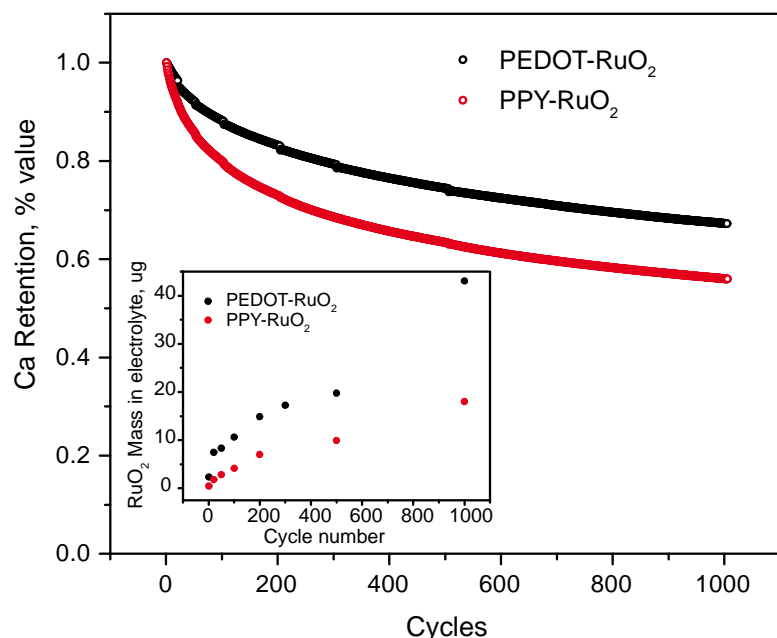


Figure 5.12 Cycling ability of the two polymer-RuO₂ nanowires

Tested in 1M H₂SO₄ at a current density of 20 mA/cm² for 1000 cycles. Inset figure shows the calculated mass loss of RuO₂ based on the detected Ru ions concentrations in the electrolyte during this cycle testing by ICP-AES

The cycling performances of the two RuO₂-polymer composite materials were investigated and the variations of the specific capacitance over 1000 cycles are shown in Figure 5.12. During the initial 200 cycles, the capacitance of the PEDOT and PPY based electrodes quickly drops to 83%, 73%, respectively. This is caused by the fast dissolution of RuO₂ into the electrolyte as evidenced by the increasing mass loss of RuO₂ with increasing cycle number based on ICP-AES results (see the inset of Figure 5.12). Thereafter, a slower decrease in the capacitance (around 15%) was observed for both materials through the 1000th cycle, corresponding to a slowly increasing

mass loss of RuO₂ during the following cycles. The fast loss of RuO₂ at low cycle numbers is probably caused by the loosely embedded/bonded RuO₂ particles formed into/onto the polymers during the redox reaction. After this initial degradation, the surviving composite material is more stable and retains the capacitance better during the remaining cycles. Although the cycling stabilities of the composite materials are not as good as pristine polymers, they still show synergistic properties resulting from the two energy materials and maintain higher capacitances than the pristine polymers even after long-term cycling.

5.4 Conclusion

In summary, we have successfully synthesized RuO₂ onto and into conductive polymer nanowires. These morphologies enable the RuO₂ to be embedded into and onto a conductive matrix while still maintaining its nano-scale size, thus enabling the high utilization of the RuO₂ in these conductive polymer nanowires. The RuO₂ nanoparticles dispersed all throughout the PEDOT nanowires were produced through a redox reaction between the perruthenate ion and the sulfur atom in PEDOT thiophene group, the latter of which was oxidized to sulfone. This further confirms the soaking method used in previous work published by our group on MnO₂ nanoparticles-enriched PEDOT. For polypyrrole nanowires, a thin layer coating of RuO₂ was formed on the PPY nanowires surface through reaction with PPY (PPY was overoxidized). In this paper, we further support our previous proposal that the redox reaction between conductive polymers and high oxidation state transition metal

oxide ions (permanganate and perruthenate) can be applied for synthesis of heterogeneous materials. This easy fabrication of heterogeneous nanomaterial shows a high utilization for the active materials and achieves both the high power and high energy density requirements that will be needed for supercapacitors in the future.

Chapter 6: Summary and Outlook

6.1 Summary

The overall goal of this project is to design beneficial architecture with synergistic energy components to fully utilize and advance the electrochemical energy in materials for energy storage application which is mainly hindered by the following factors: (1) poor electrical conductivity (e.g. MnO_2), (2) long ion diffusion process (e.g. in bulk structure).

This thesis introduced different approaches to achieve this goal. These include:

1. Applying cellulose fibers as the substrate for energy material deposition.
Cellulose fibers act as an internal electrolyte reservoir and boost ion diffusion process
2. Electro co-deposition $\text{RuO}_2\text{-MnO}_2$ composite nanowires, which demonstrates a simple effective way to directly improve the electrical conductivity in MnO_2 , of which the electrochemical performance is limited by its intrinsic poor conductivity
3. Induce a straight forward way to grow metal oxides into/onto conductive polymer nanowires, which demonstrates a general route to prepare synergistic architecture for energy applications

In all these projects, charge transfer process is the interest of focus at both scientific and applied levels, different aspects associated with this process are tailored by different methods. Summary of each chapter include:

Chapter 3:

- I. Cellulose fibers are applied as substrate for the deposition of MnO_2 ; meanwhile, function as an internal electrolyte reservoir which enables additional ion diffusion pathway from the substrate to the MnO_2 layer.
- II. CNT wrapping on top of the MnO_2 layer was fabricated and act as additional electron pathway to active materials.
- III. Excellent cycleability up to 50k cycles were observed in the P-CMC electrode, which is attributed to the soft flexibility of cellulose fibers and its strong affinity to MnO_2 layer deposited on top, compared to the smooth polyester fiber with less cycling stability.
- IV. A series of electrodes with different number of electron/ion pathways were designed and compared in this study. Direct improvement was observed with increasing charge transfer pathway, which confirmed the importance of advancing the charge transfer process for the success in future electrochemical energy storage systems.

Chapter 4:

- I. Free standing 1D nanoarrays with good connection to current collector was synthesized by electrodeposition assisted with AAO template. This array nano architecture facilitates both the ion diffusion and electron transfer processes between the material and the current collector.
- II. Electrochemical co-deposition of $\text{RuO}_2\text{-MnO}_2$ composite material was applied here and homogeneous nanowires were grown, showing improved electrical conductivity with RuO_2 loading

- III. The RuO₂ loading amount effect was carefully studied by the EIS characterization and deconvolution of the capacitance of samples prepared with different RuO₂ weight percentages.

Chapter 5:

- I. Conductive polymer nanowires were explored here as conductive matrixes for the metal oxides growth through the redox reaction between high-charge stated metal ions with polymer reductive sites.
- II. A general route to grow 1D nanoarrays of polymer-metal oxide hybrid materials was demonstrated in this work.
- III. Depending on the ions permeability in different polymer nanowires, two different RuO₂-polymer structural integrating ways were shown, either as core-shell structure or as nanoparticle enriched nanowires structure.

6.2 Outlook

This thesis work has been focus on tailoring the factors that influence the charge (electron/ion) transfer process in energy storage and systematic studying their roles. Different approach realized through substrate, structure, or compositions regulations were explored in this work. The study on cellulose fibers substrate can be extended to explore fibers with scale-down radical size where higher surface area can be applied for energy material deposition, or explore any other water-absorbing material for prospective application as substrate. 1D ordered nanoarrays synthesized with in AAO template, with ion-diffusion beneficial structure, good connection to current collector,

and good packing efficiency can be utilized for all different kinds of energy materials. The determinable effect of charge transfer process on energy and power performance is concluded, not quiet can be well achieve by solely structural modification though. Hybrid material with synergistic properties is proposed to resolve the challenge and is now playing a crucial role in leading to the success in future energy. Feasible fabrication method is required toward this object. The electro co-deposition and redox induced deposition introduced in this thesis demonstrate two approaches among the reported diverse methods, of which work and effort is continuous going to. The fundamental study and understanding on how hybrid materials work during charge/discharge process, if not more, is as important as getting high performance. Our investigation developed in chapter 4 gained insight into how the co-deposited RuO_2 advantages the MnO_2 electrochemical properties, in terms of electrical conductivity and contribution to different capacitance components. This kind of fundamental study is also needed in any of the new developed hybrid energy materials in the future. Hybrid materials with desired properties fabricated in beneficial structure may very well lead to the success for energy storage devices.

Publication

Chapter 3 in this dissertation has been published in

ACS Nano, **2013**, 7, 6037–6046

Appendices

Table A1. Literature Survey of MnO₂ based Supercapacitors Electrode.

Category	composition	structure	synthesis	capacitance
Pure MnO ₂	N/A	Ultrathin film ¹⁹⁷	Sol-gel	700 F/g @ 50 mV/s
		Thin film ⁴²	Sol-gel	100-200 F/g @ 5 mV/s
		Hollow nanosphere ¹⁹⁸	Hydrothermal using SiO ₂ template	299 F/g @ 5 mV/s
		Nanowires arrays ¹³²	Sol-gel using AAO template	165 F/g @ 10 mV/s
MnO ₂ -Polymer	PEDOT ^{102,121}	Coaxial nanowires	Co-electrodeposition	210 F/g @ 5 mA/cm ²
	PPY ¹⁹⁹	Nanorods	Chemical co-precipitation	294 F/g @ 1 A/g
	Polyaniline ²⁰⁰	Porous film	Two-step electrodeposition	715 F/g @ 5 mA/cm ²
MnO ₂ -Carbon	Mesoporous carbon ¹¹⁷	Mesoporous	Redox-reaction	220 F/g @ 5 mV/s
	Graphite ^{136,201}	Nanoplatelet	Chemical co-precipitation	120-160 F/g
	CNTs ²⁰²	Nanoflowers	Electrodeposition	199 F/g @ 1 A/g

Reference

1. J. R. Miller and P. Simon, *Science*, 2008, **321**, 651–652.
2. M. Armand and J.-M. Tarascon, *Nature*, 2008, **451**, 652–657.
3. J. M. Tarascon and M. Armand, *Nature*, 2001, **414**, 359–367.
4. R. F. Service, *Science*, 2006, **313**, 902.
5. B. E. Conway, *Electrochemical supercapacitors: scientific fundamentals and technological applications*, Kluwer Academic/ Plenum Publishers, New York, 1999.
6. P. Simon and Y. Gogotsi, *Nat. Mater.*, 2008, **7**, 845–854.
7. J. R. Miller and A. F. Burke, *Electrochem. Soc. Interface*, 2008, **17**, 53–57.
8. K. Naoi and P. Simon, *Electrochem. Soc. interface*, 2008, **17**, 34–37.
9. J. Long, *Electrochem. Soc. Interface*, 2008, **17**, 33.
10. M. Jayalakshmi and K. Balasubramanian, *Int. J. Electrochem. Sci.*, 2008, **3**, 1196–1217.
11. B. Conway, *J. Electrochem. Soc.*, 1991, **138**, 1539–1548.
12. S. Kurzwei and P. Trasatti, *Platin. Met. Rev.*, 1994, **38**, 46–56.
13. S. Pay and Y. Baghzouz, in *2003 IEEE Bologna Power Tech Conference Proceedings*, IEEE, 2003, vol. 3, pp. 728–733.
14. D. Bouquain, B. Blunier, and A. Miraoui, in *2009 IEEE Vehicle Power and Propulsion Conference*, IEEE, 2009, pp. 584–591.
15. J. M. Miller, U. Deshpande, T. J. Dougherty, and T. Bohn, in *2009 Twenty-Fourth Annual IEEE Applied Power Electronics Conference and Exposition*, IEEE, 2009, pp. 190–198.
16. H. I. Becker, 1957, U.S. Patent 2 800 616.
17. H. V. Helmholtz, *Ann. Phys. (Leipzig)*, 1853, **89**, 21.

18. D. L. Chapman, *Philos. Mag.*, 1913, **6**, 475.
19. G. Gouy, *J. Phys.*, 1910, **9**, 457–468.
20. H. Pan, J. Li, and Y. Feng, *Nanoscale Res. Lett.*, 2010, **5**, 654–668.
21. M. Kaempgen, C. K. Chan, J. Ma, Y. Cui, and G. Gruner, *Nano Lett.*, 2009, **9**, 1872–1876.
22. E. Frackowiak, *Carbon N. Y.*, 2002, **40**, 1775–1787.
23. H. Y. Jung, M. B. Karimi, M. G. Hahm, P. M. Ajayan, and Y. J. Jung, *Sci. Rep.*, 2012, **2**, 773.
24. L. L. Zhang and X. S. Zhao, *Chem. Soc. Rev.*, 2009, **38**, 2520–2531.
25. E. Frackowiak, *Phys. Chem. Chem. Phys.*, 2007, **9**, 1774–1785.
26. P. Simon and A. Burke, *Electrochem. Soc. Interface*, 2008, **17**, 38–43.
27. M. D. Stoller, S. Park, Y. Zhu, J. An, and R. S. Ruoff, *Nano Lett.*, 2008, **8**, 3498–3502.
28. L. L. Zhang, R. Zhou, and X. S. Zhao, *J. Mater. Chem.*, 2010, **20**, 5983–5992.
29. D. S. Su and G. Centi, *J. Energy Chem.*, 2013, **22**, 151–173.
30. T. Bordjiba, M. Mohamedi, and L. H. Dao, *Adv. Mater.*, 2008, **20**, 815–819.
31. S. Trasatti and G. Buzzanca, *J. Electroanal. Chem.*, 1971, **29**, 1.
32. J. P. Zheng, P. J. Cygan, and T. R. Jow, *J. Electrochem. Soc.*, 1995, **142**, 2699–2703.
33. D. A. Mckeown, P. L. Hagans, L. P. L. Carette, A. E. Russell, K. E. Swider, and D. R. Rolison, *J. Phys. Chem. B*, 1999, **103**, 4825–4832.
34. C. Hu, *J. Electrochem. Soc.*, 1999, **146**, 2465–2471.
35. D. Galizzioli, F. Tantardini, and S. Trasatti, *J. Appl. Electrochem.*, 1974, **4**, 57–67.
36. G. Lodi, E. Sivieri, A. Battisti, and S. Trasatti, *J. Appl. Electrochem.*, 1978, **8**, 135–143.

37. P. Soudan, J. Gaudet, D. Guay, D. Bédanger, and R. Schulz, *Chem. Mater.*, 2002, **14**, 1210–1215.
38. J. P. Zheng and Y. Xin, *J. Power Sources*, 2002, **110**, 86–90.
39. C.-C. Hu, W.-C. Chen, and K.-H. Chang, *J. Electrochem. Soc.*, 2004, **151**, A281–A290.
40. C. C. Hu, K. H. Chang, M. C. Lin, and Y. T. Wu, *Nano Lett.*, 2006, **6**, 2690–2695.
41. D. Susanti, D.-S. Tsai, Y.-S. Huang, A. Korotcov, and W.-H. Chung, *J. Phys. Chem. C*, 2007, **111**, 9530–9537.
42. H. Y. Lee and J. B. Goodenough, *J. Solid State Chem.*, 1999, **144**, 220–223.
43. B. B. Owens, S. Passerini, and W. H. Smyrl, *Electrochem. commun.*, 1999, **45**, 215–224.
44. M. Min, K. Machida, J. H. Jang, and K. Naoi, *J. Electrochem. Soc.*, 2006, **153**, A334–A338.
45. H. Xia, M. O. Lai, and L. Lu, *JOM*, 2011, **63**, 54–60.
46. M. Toupin, T. Brousse, D. Be, and D. Bédanger, *Chem. Mater.*, 2004, **16**, 3184–3190.
47. S. W. Zhang and G. Z. Chen, *Energy Mater. Mater. Sci. Eng. Energy Syst.*, 2008, **3**, 186–200.
48. W. Wei, X. Cui, W. Chen, and D. G. Ivey, *Chem. Soc. Rev.*, 2011, **40**, 1697–721.
49. C. Xu, H. Du, B. Li, F. Kang, and Y. Zeng, *J. Electrochem. Soc.*, 2009, **156**, A73.
50. J.-K. Chang and W.-T. Tsai, *J. Electrochem. Soc.*, 2003, **150**, A1333–A1338.
51. Z. Lu, Z. Chang, J. Liu, and X. Sun, *Nano Res.*, 2011, **4**, 658–665.
52. G.-W. Yang, C.-L. Xu, and H.-L. Li, *Chem. Commun. (Camb.)*, 2008, 6537–6539.
53. G. Fu, Z. Hu, L. Xie, X. Jin, Y. Xie, Y. Wang, and Z. Zhang, *Int. J. Electrochem. Sci.*, 2009, **4**, 1052–1062.

54. H. Jiang, T. Zhao, C. Li, and J. Ma, *J. Mater. Chem.*, 2011, **21**, 3818–3823.
55. B. Saravanakumar, K. K. Purushothaman, and G. Muralidharan, *ACS Appl. Mater. Interfaces*, 2012, **4**, 4484–4490.
56. H. Y. Lee and J. B. Goodenough, *J. Solid State Chem.*, 1999, **148**, 81–84.
57. D. B. Dang, L. Brousse, and J. Long, *Electrochem. Soc. Interface*, 2008, **17**, 49–52.
58. A. Rudge, J. Davey, I. Raistrick, S. Gottesfeld, and J. P. Ferraris, *J. Power Sources*, 1994, **47**, 89–107.
59. G. A. Snook, P. Kao, and A. S. Best, *J. Power Sources*, 2011, **196**, 1–12.
60. R. J. Waltman and J. Bargon, *Can. J. Chem.*, 1986, **64**, 76–95.
61. A. Malinauskas, J. Malinauskiene, and A. Ramanavičius, *Nanotechnology*, 2005, **16**, R51–R62.
62. P. J. Nigrey, *J. Electrochem. Soc.*, 1981, **128**, 1651–1654.
63. A. Feldblum, A. J. Heeger, T. -C. Chung, and A. G. MacDiarmid, *J. Chem. Phys.*, 1982, **77**, 5114.
64. R. B. Kaner and A. G. MacDiarmid, *Synth. Met.*, 1986, **14**, 3–12.
65. R. B. Kaner and A. G. MacDiarmid, *J. Chem. Soc. Faraday Trans. 1*, 1984, **80**, 2109.
66. M. Gholamian, J. Sundaram, and A. Q. Contractor, *Langmuir*, 1987, **3**, 741–744.
67. B. K. Kuila, B. Nandan, M. Böhme, A. Janke, and M. Stamm, *Chem. Commun. (Camb.)*, 2009, 5749–5751.
68. R. K. Sharma, a. C. Rastogi, and S. B. Desu, *Electrochem. commun.*, 2008, **10**, 268–272.
69. Q. F. Wu, K. X. He, H. Y. Mi, and X. G. Zhang, *Mater. Chem. Phys.*, 2007, **101**, 367–371.
70. B. Muthulakshmi, D. Kalpana, S. Pitchumani, and N. G. Renganathan, *J. Power Sources*, 2006, **158**, 1533–1537.

71. L.-Z. Fan and J. Maier, *Electrochem. commun.*, 2006, **8**, 937–940.
72. K. A. Noh, D.-W. Kim, C.-S. Jin, K.-H. Shin, J. H. Kim, and J. M. Ko, *J. Power Sources*, 2003, **124**, 593–595.
73. G. Sabouraud, S. Sadki, and N. Brodie, *Chem. Soc. Rev.*, 2000, **29**, 283–293.
74. J. C. Carlberg, 1997, **144**, 8–11.
75. Y. Wang, *J. Phys. Conf. Ser.*, 2009, **152**, 012023.
76. T. F. Otero and M. C. Romero, *J. Phys. Conf. Ser.*, 2008, **127**, 012016.
77. K. Ryu, Y. Lee, Y. Hong, Y. Park, X. Wu, K. Kim, M. Kang, N. Park, and S. Chang, *Electrochim. Acta*, 2004, **50**, 843–847.
78. B. L. Groenendaal, F. Jonas, D. Freitag, H. Pielartzik, and J. R. Reynolds, 2000, 481–494.
79. W. G. Pell and B. E. Conway, *J. Power Sources*, 1996, **63**, 255–266.
80. L. F. Nazar, G. Goward, F. Leroux, M. Duncan, H. Huang, T. Kerr, and J. Gaubicher, *Int. J. Inorg. Mater.*, 2001, **3**, 191–200.
81. Z. Yin and Q. Zheng, *Adv. Energy Mater.*, 2012, **2**, 179–218.
82. A. S. Aricò, P. Bruce, B. Scrosati, J.-M. Tarascon, and W. van Schalkwijk, *Nat. Mater.*, 2005, **4**, 366–77.
83. M. Conte, P. . Prosini, and S. Passerini, *Mater. Sci. Eng. B*, 2004, **108**, 2–8.
84. X. Zhao, B. M. Sánchez, P. J. Dobson, and P. S. Grant, *Nanoscale*, 2011, **3**, 839–855.
85. R. Liu, J. Duay, and S. B. Lee, *Chem. Commun.*, 2011, **47**, 1384–1404.
86. J. N. Broughton and M. J. Brett, *Electrochim. Acta*, 2005, **50**, 4814–4819.
87. J. . Broughton and M. . Brett, *Electrochim. Acta*, 2004, **49**, 4439–4446.
88. X. Lang, A. Hirata, T. Fujita, and M. Chen, *Nat. Nanotechnol.*, 2011, **6**, 232–236.
89. P. Banerjee, I. Perez, L. Henn-lecordier, S. B. Lee, and G. W. Rubloff, *Nat. Nanotechnol.*, 2009, **4**, 292–296.

90. V. L. Pushparaj, P. K. Narwankar, and O. Nalamasu, 2011, US20110045349.
91. Y. Liu, X. H. Liu, B.-M. Nguyen, J. Yoo, J. P. Sullivan, S. T. Picraux, J. Y. Huang, and S. A. Dayeh, *Nano Lett.*, 2013, **13**, 4876–4883.
92. K. Karki, E. Epstein, J.-H. Cho, Z. Jia, T. Li, S. T. Picraux, C. Wang, and J. Cumings, *Nano Lett.*, 2012, **12**, 1392–1397.
93. X. H. Liu, H. Zheng, L. Zhong, S. Huang, K. Karki, L. Q. Zhang, Y. Liu, A. Kushima, W. T. Liang, J. W. Wang, J.-H. Cho, E. Epstein, S. A. Dayeh, S. T. Picraux, T. Zhu, J. Li, J. P. Sullivan, J. Cumings, C. Wang, S. X. Mao, Z. Z. Ye, S. Zhang, and J. Y. Huang, *Nano Lett.*, 2011, **11**, 3312–3318.
94. X. H. Liu, J. W. Wang, S. Huang, F. Fan, X. Huang, Y. Liu, S. Krylyuk, J. Yoo, S. A. Dayeh, A. V Davydov, S. X. Mao, S. T. Picraux, S. Zhang, J. Li, T. Zhu, and J. Y. Huang, *Nat. Nanotechnol.*, 2012, **7**, 749–756.
95. W.-M. Zhang, X.-L. Wu, J.-S. Hu, Y.-G. Guo, and L.-J. Wan, *Adv. Funct. Mater.*, 2008, **18**, 3941–3946.
96. Y. Wang, Y. Wang, E. Hosono, K. Wang, and H. Zhou, *Angew. Chem. Int. Ed. Engl.*, 2008, **47**, 7461–7465.
97. Y. Kwon, H. Kim, S.-G. Doo, and J. Cho, *Chem. Mater.*, 2007, **19**, 982–986.
98. K. Takahashi, Y. Wang, and G. Cao, *J. Phys. Chem. B*, 2005, **109**, 48–51.
99. Y.-S. Hu, X. Liu, J.-O. Müller, R. Schlögl, J. Maier, and D. S. Su, *Angew. Chem. Int. Ed. Engl.*, 2009, **48**, 210–214.
100. A. L. M. Reddy, M. M. Shaijumon, S. R. Gowda, P. M. Ajayan, A. Leela, and M. Reddy, *Nano Lett.*, 2009, **9**, 1002–1006.
101. P. L. Taberna, S. Mitra, P. Poizot, P. Simon, and J.-M. Tarascon, *Nat. Mater.*, 2006, **5**, 567–573.
102. R. Liu and S. B. Lee, *J. Am. Chem. Soc.*, 2008, **130**, 2942–2943.
103. L. L. Zhang, S. Li, J. Zhang, P. Guo, J. Zheng, and X. S. Zhao, *Chem. Mater.*, 2010, **22**, 1195–1202.
104. K. T. Lee, J. C. Lytle, N. S. Ergang, S. M. Oh, and A. Stein, *Adv. Funct. Mater.*, 2005, **15**, 547–556.

105. J. Fan, T. Wang, C. Yu, B. Tu, Z. Jiang, and D. Zhao, *Adv. Mater.*, 2004, **16**, 1432–1436.
106. Y.-G. Wang, H.-Q. Li, and Y.-Y. Xia, *Adv. Mater.*, 2006, **18**, 2619–2623.
107. X. Ji, K. T. Lee, and L. F. Nazar, *Nat. Mater.*, 2009, **8**, 500–506.
108. Y. Xu, J. Wang, W. Sun, and S. Wang, *J. Power Sources*, 2006, **159**, 370–373.
109. R. Liu, S. Il Cho, and S. B. Lee, *Nanotechnology*, 2008, **19**, 1–8.
110. S. Il Cho and S. B. Lee, *Acc. Chem. Res.*, 2008, **41**, 699–707.
111. R. Liu, J. Duay, and S. B. Lee, *ACS Nano*, 2010, **4**, 4299–4307.
112. R. Liu, J. Duay, T. Lane, and S. Bok Lee, *Phys. Chem. Chem. Phys.*, 2010, **12**, 4309–4316.
113. Y.-T. Wu and C.-C. Hu, *J. Electrochem. Soc.*, 2004, **151**, A2060–A2066.
114. C. Y. Lee, H. M. Tsai, H. J. Chuang, S. Y. Li, P. Lin, and T. Y. Tseng, *J. Electrochem. Soc.*, 2005, **152**, A716–A720.
115. E. Raymundo-Piñero, V. Khomenko, E. Frackowiak, and F. Béguin, *J. Electrochem. Soc.*, 2005, **152**, A229–A235.
116. A. E. Fischer, K. A. Pettigrew, D. R. Rolison, R. M. Stroud, and J. W. Long, *Nano Lett.*, 2007, **7**, 281–286.
117. X. Dong, W. Shen, J. Gu, L. Xiong, Y. Zhu, H. Li, and J. Shi, *J. Phys. Chem. B*, 2006, **110**, 6015–6019.
118. G. Yu, L. Hu, N. Liu, H. Wang, M. Vosgueritchian, Y. Yang, Y. Cui, and Z. Bao, *Nano Lett.*, 2011, **11**, 4438–4442.
119. J. Duay, E. Gillette, R. Liu, and S. B. Lee, *Phys. Chem. Chem. Phys.*, 2012, **14**, 3329–3337.
120. A. H. Gemeay, H. Nishiyama, S. Kuwabata, and H. Yoneyama, 1995, **142**, 4190–4195.
121. R. Liu, J. Duay, and S. B. Lee, *ACS Nano*, 2011, **5**, 5608–5619.
122. S. a Sherrill, J. Duay, Z. Gui, P. Banerjee, G. W. Rubloff, and S. B. Lee, *Phys. Chem. Chem. Phys.*, 2011, **13**, 15221–15226.

123. Y. Xia, P. Yang, Y. Sun, Y. Wu, B. Mayers, B. Gates, Y. Yin, F. Kim, and H. Yan, *Adv. Mater.*, 2003, **15**, 353–389.
124. A. M. Md Jani, D. Losic, and N. H. Voelcker, *Prog. Mater. Sci.*, 2013, **58**, 636–704.
125. W. Lee, R. Ji, U. Gösele, and K. Nielsch, *Nat. Mater.*, 2006, **5**, 741–747.
126. K. Pitzschel, J. M. M. Moreno, J. Escrig, O. Albrecht, K. Nielsch, and J. Bachmann, *ACS Nano*, 2009, **3**, 3463–3468.
127. W. Lee, K. Schwirn, M. Steinhart, E. Pippel, R. Scholz, and U. Gösele, *Nat. Nanotechnol.*, 2008, **3**, 234–239.
128. G. D. Sulka and K. Hnida, *Nanotechnology*, 2012, **23**, 075303.
129. B. Chen, Q. Xu, X. Zhao, X. Zhu, M. Kong, and G. Meng, *Adv. Funct. Mater.*, 2010, **20**, 3791–3796.
130. H. Xing, L. Zhiyuan, W. Kai, and L. Yi, *Electrochem. commun.*, 2011, **13**, 1082–1085.
131. C. Shuoshuo, L. Zhiyuan, H. Xing, Y. Hui, and L. Yi, *J. Mater. Chem.*, 2010, **20**, 1794–1798.
132. X. Wang, X. Wang, W. Huang, P. J. Sebastian, and S. Gamboa, *J. Power Sources*, 2005, **140**, 211–215.
133. P. Yu, X. Zhang, Y. Chen, and Y. Ma, *Mater. Lett.*, 2010, **64**, 61–64.
134. V. Subramanian, H. Zhu, R. Vajtai, P. M. Ajayan, and B. Wei, *J. Phys. Chem. B*, 2005, **109**, 20207–20214.
135. E. Beaudrouet, a. Le Gal La Salle, and D. Guyomard, *Electrochim. Acta*, 2009, **54**, 1240–1248.
136. J. Yan, Z. Fan, T. Wei, Z. Qie, S. Wang, and M. Zhang, *Mater. Sci. Eng. B*, 2008, **151**, 174–178.
137. V. Subramanian, H. Zhu, and B. Wei, *Electrochem. commun.*, 2006, **8**, 827–832.
138. Y.-S. Chen and C.-C. Hu, *Electrochem. Solid-State Lett.*, 2003, **6**, A210–A213.

139. T. Brousse and D. Bélanger, *Electrochem. Solid-State Lett.*, 2003, **6**, A244–A248.
140. K. Rajendra Prasad and N. Miura, *Electrochem. commun.*, 2004, **6**, 1004–1008.
141. M. Nakayama, A. Tanaka, Y. Sato, T. Tonosaki, and K. Ogura, *Langmuir*, 2005, **21**, 5907–5913.
142. M. Nakayama, A. Tanaka, S. Konishi, and K. Ogura, *J. Mater. Res.*, 2011, **19**, 1509–1515.
143. M.-T. Lee, J.-K. Chang, W.-T. Tsai, and C.-K. Lin, *J. Power Sources*, 2008, **178**, 476–482.
144. M. Nakayama, M. Nishio, and K. Ogura, *J. Mater. Res.*, 2011, **18**, 2364–2370.
145. T.-S. Hyun, J.-E. Kang, H.-G. Kim, J.-M. Hong, and I.-D. Kim, *Electrochem. Solid-State Lett.*, 2009, **12**, A225–A228.
146. J. J. Xu, J. Yang, and G. Jain, *Electrochem. Solid-State Lett.*, 2002, **5**, A223–A226.
147. M. Sathiya, K. Ramesha, G. Rouse, D. Foix, D. Gonbeau, A. S. Prakash, M. L. Doublet, K. Hemalatha, and J.-M. Tarascon, *Chem. Mater.*, 2013, **25**, 1121–1131.
148. J. Wen, X. Ruan, and Z. Zhou, *J. Phys. Chem. Solids*, 2009, **70**, 816–820.
149. J. M. Fletcher, W. E. Gardner, B. F. Greenfield, M. J. Holdoway, and M. H. Rand, *J. Chem. Soc. A Inorganic, Phys. Theor.*, 1968, 653–657.
150. C. N. Chervin, A. M. Lubers, J. W. Long, and D. R. Rolison, *J. Electroanal. Chem.*, 2010, **644**, 155–163.
151. W.-C. Fang, J.-H. Huang, L.-C. Chen, Y.-L. O. Su, and K.-H. Chen, *J. Power Sources*, 2006, **160**, 1506–1510.
152. C. Julien, M. Massot, R. Baddour-hadjean, S. Franger, S. Bach, and J. P. Pereira-ramos, *Solid State Ionics*, 2003, **159**, 345 – 356.
153. C. Mun, J. J. Ehrhardt, J. Lambert, and C. Madic, *Appl. Surf. Sci.*, 2007, **253**, 7613–7621.
154. A. Foelske, O. Barbieri, M. Hahn, and R. Kötz, *Electrochem. Solid-State Lett.*, 2006, **9**, A268–A272.

155. H. Xia, Y. Shirley Meng, G. Yuan, C. Cui, and L. Lu, *Electrochem. Solid-State Lett.*, 2012, **15**, A60–A63.
156. J. R. M. Evgenij Barsoukov, *Impedance Spectroscopy*, John Wiley & Sons, Inc., Hoboken, NJ, USA, 2005.
157. J. Bisquert, G. Garcia-Belmonte, F. Fabregat-Santiago, N. S. Ferriols, P. Bogdanoff, and E. C. Pereira, *J. Phys. Chem. B*, 2000, **104**, 2287–2298.
158. J. Bisquert, *J. Phys. Chem. B*, 2002, **106**, 325–333.
159. F. Fabregat-Santiago, J. Bisquert, G. Garcia-Belmonte, G. Boschloo, and A. Hagfeldt, *Sol. Energy Mater. Sol. Cells*, 2005, **87**, 117–131.
160. S. Ardizzone, G. Fregonara, and S. Trasatti, *Electrochim. Acta*, 1990, **35**, 263–267.
161. J. Wang, J. Polleux, J. Lim, and B. Dunn, *J. Phys. Chem. C*, 2007, **111**, 14925–14931.
162. W. Yan, T. Ayvazian, J. Kim, Y. Liu, K. C. Donovan, W. Xing, Y. Yang, J. C. Hemminger, and R. M. Penner, *ACS Nano*, 2011, **5**, 8275–8287.
163. J. Duay, S. A. Sherrill, Z. Gui, E. Gillette, and S. B. Lee, *ACS Nano*, 2013, **7**, 1200–1214.
164. P. J. Hall, M. Mirzaeian, S. I. Fletcher, F. B. Sillars, A. J. R. Rennie, G. O. Shitta-Bey, G. Wilson, A. Cruden, and R. Carter, *Energy Environ. Sci.*, 2010, **3**, 1238–1251.
165. N.-R. Chiou, C. Lu, J. Guan, L. J. Lee, and A. J. Epstein, *Nat. Nanotechnol.*, 2007, **2**, 354–357.
166. D. Ge, S. Huang, R. Qi, J. Mu, Y. Shen, and W. Shi, *Chemphyschem*, 2009, **10**, 1916–1921.
167. L. Liu, C. Zhao, Y. Zhao, N. Jia, Q. Zhou, M. Yan, and Z. Jiang, *Eur. Polym. J.*, 2005, **41**, 2117–2121.
168. M. Wan, *Adv. Mater.*, 2008, **20**, 2926–2932.
169. L. Zhang and M. Wan, *Adv. Funct. Mater.*, 2003, **13**, 815–820.
170. M. S. Sander, A. L. Prieto, R. Gronsky, T. Sands, and A. M. Stacy, *Adv. Mater.*, 2002, **14**, 665–667.

171. A. D. Franklin, D. B. Janes, J. C. Claussen, T. S. Fisher, and T. D. Sands, *Appl. Phys. Lett.*, 2008, **92**, 013122.
172. R. Yang, C. Sui, J. Gong, and L. Qu, *Mater. Lett.*, 2007, **61**, 900–903.
173. J. C. Claussen, M. M. Wickner, T. S. Fisher, and D. M. Porterfield, *ACS Appl. Mater. Interfaces*, 2011, **3**, 1765–1770.
174. K. E. Swider, C. I. Merzbacher, P. L. Hagans, and D. R. Rolison, *Chem. Mater.*, 1997, **9**, 1248–1255.
175. A. C. Gallegos and P. Gomez-Romero, *J. New Mater. Electrochem. Syst.*, 2005, **188**, 181–188.
176. I. Rodriguez, B. R. Scharifker, and J. Mostany, *J. Electroanal.*, 2000, **491**, 117–125.
177. Ö. Türkarslan, S. K. Kayahan, and L. Toppare, *J. Solid State Electrochem.*, 2008, **13**, 657–663.
178. A. Kros, S. W. F. M. van Hövell, N. A. J. M. Sommerdijk, and R. J. M. Nolte, *Adv. Mater.*, 2001, **13**, 1555–1557.
179. J. C. Claussen, A. Kumar, D. B. Jaroch, M. H. Khawaja, A. B. Hibbard, D. M. Porterfield, and T. S. Fisher, *Adv. Funct. Mater.*, 2012, **22**, 3399–3405.
180. J. A. Arter, D. K. Taggart, T. M. McIntire, R. M. Penner, and G. A. Weiss, *Nano Lett.*, 2010, **10**, 4858–4862.
181. T. R. L. C. Paix ão and M. Bertotti, *Electroanalysis*, 2008, **20**, 1671–1677.
182. P. Kotzian, P. Brázdilová, K. Kalcher, and K. Vytřas, *Anal. Lett.*, 2005, **38**, 1099–1113.
183. Y. Peng, G. Yi, and Z. Gao, *Chem. Commun. (Camb.)*, 2010, **46**, 9131–9133.
184. Y. Cao and T. E. Mallouk, *Chem. Mater.*, 2008, **20**, 5260–5265.
185. H. Yan, L. Zhang, J. Shen, Z. Chen, G. Shi, and B. Zhang, *Nanotechnology*, 2006, **17**, 3446–3450.
186. R. Temmer, A. Maziz, C. Plesse, A. Aabloo, F. Vidal, and T. Tamm, *Smart Mater. Struct.*, 2013, **22**, 104006.
187. L. Ji, J. Lin, and H. C. Zeng, *Chem. Mater.*, 2001, **13**, 2403–2412.

188. S. Bhaskar, P. S. Dobal, S. B. Majumder, and R. S. Katiyar, *J. Appl. Phys.*, 2001, **89**, 2987–2992.
189. T. P. Luxton, M. J. Eick, and K. G. Scheckel, *J. Colloid Interface Sci.*, 2011, **359**, 30–39.
190. D. Rochefort, P. Dabo, D. Guay, and P. M. A. Sherwood, *Electrochim. Acta*, 2003, **48**, 4245–4252.
191. O. Barbieri, M. Hahn, A. Foelske, and R. Kötz, *J. Electrochem. Soc.*, 2006, **153**, A2049–A2054.
192. S. Ghosh, G. A. Bowmaker, R. P. Cooney, and J. M. Seakins, *Synth. Met.*, 1998, **95**, 63–67.
193. G. I. Mathys and V.-T. Truong, *Synth. Met.*, 1997, **89**, 103–109.
194. P. Novák, B. Rasch, and W. Vielstich, *J. Electrochem. Soc.*, 1991, **138**, 3300–3304.
195. T. W. Lewis, G. G. Wallace, C. Y. Kim, and D. Y. Kim, *Synth. Met.*, 1997, **84**, 403–404.
196. F. Palmisano, C. Malitesta, D. Centonze, and P. G. Zambonin, *Anal. Chem.*, 1995, **67**, 2207–2211.
197. S.-C. Pang, M. A. Anderson, and T. W. Chapman, *J. Electrochem. Soc.*, 2000, **147**, 444–450.
198. X. Tang, Z. Liu, C. Zhang, Z. Yang, and Z. Wang, *J. Power Sources*, 2009, **193**, 939–943.
199. J. Zang and X. Li, *J. Mater. Chem.*, 2011, **21**, 10965–10969.
200. K. R. Prasad and N. Miura, *Electrochem. Solid-State Lett.*, 2004, **7**, A425–A428.
201. C. Wan, K. Azumi, and H. Konno, *Electrochim. Acta*, 2007, **52**, 3061–3066.
202. H. Zhang, G. Cao, Z. Wang, Y. Yang, Z. Shi, and Z. Gu, *Nano Lett.*, 2008, **8**, 2664–2668.